LABORATORY-SCALE PETROPHYSICAL EVALUATION OF LITHOFACIES EFFECT ON RESERVOIR & SOURCE QUALITY AND CORE-CALIBARTED WELL LOG ANALYSIS IN PENNSYLVANIAN-PERMIAN WOLFCAMP-SPRABERRY INTERVALS, MIDLAND BASIN, TEXAS, USA

By:

Samuel John Becker

Presented to the Faculty of the Graduate School of

The University of Texas at Arlington in Partial Fulfillment

Of the Requirements for the Degree of

MASTER OF SCIENCE IN GEOLOGY

THE UNIVERSITY OF TEXAS AT ARLINGTON

December 2019

Acknowledgements

I'd like to thank my advisor, Dr. Max Qinhong Hu, for his guidance and insight throughout my time at UT Arlington. Also, thanks to my committee members, Dave Cannon, Dr. John Wickham, and Dr. Naresh Kumar for their support.

This study would not have been possible without the support of Paul Molnar and Dave Cannon at Diamondback Energy, who supplied the core, data, and initial research direction.

I would also like to acknowledge Andy Faigle of the Bureau of Economic Geology for sample procurement, IHS for PETRA and DrillingInfo Pro version database donated to UT Arlington, Qiming Wang for his guidance in the lab, and Brian Jarvie of GeoMark for his insight.

Finally, a special thanks is owed to my family and friends especially my parents, John and Rea Lynn Becker, for their constant support throughout my life.

Abstract

Laboratory-Scale Petrophysical Evaluation of Lithofacies Effect on Reservoir & Source Quality and Core-Calibrated Well Log Analysis in Pennsylvanian-Permian Wolfcamp-Spraberry Intervals, Midland Basin, Texas, USA

Samuel John Becker, M.S.

The University of Texas at Arlington, 2019

Supervising Professor: Q.H. Hu

The "Wolfberry" play, which is made up of the Spraberry and Wolfcamp formations, is an important resource for the exploitation of hydrocarbons with a need for additional petrophysical understanding. Although the Wolfcamp is categorized as a shale, it is a complex and heterogeneous formation composed of multiple facies. The unique lithological composition of each facies controls formation properties, which further drive reservoir/source quality. With the integrated laboratory- and field-scale analyses, this study uses mostly laboratory petrophysical evaluation to gain insight on the relationship between facies and reservoir/source quality in the Lower Spraberry and Wolfcamp intervals throughout the Midland Basin. To achieve this objective, 48 core plugs taken from three wells evenly spaced in the Basin, that represent different facies end members in several of the Lower Spraberry and Wolfcamp intervals, are evaluated. In order to evaluate the Wolfberry formations, vacuum-assisted fluid immersion porosimetry (FIP), fluid displacement, fluid imbibition, total organic carbon (TOC), pyrolysis, X-ray diffraction (XRD), contact angle, and mercury intrusion porosimetry (MIP) tests were used to investigate petrophysical properties such as porosity, geochemistry, mineral

composition, wettability, permeability, and tortuosity. Facies were divided into three groups of depositional environments for comparison: lowstand channel fan complex and windblown deposited siliceous/clay rich lithotypes, highstand/lowstand reef carbonate gravity flow deposited packstones and grainstones, and highstand deep-water hemipelagic and distal turbidity current deposited carbonate mudstones. From the petrophysical and geochemical results of this study, it was determined that the Lower Spraberry and Wolfcamp intervals are primarily oil-wet to intermediate-wet, and both reservoir quality and source potential increase as the carbonate content decreases, and they are the highest in the siliceous- and clay-rich facies (porosity 2.0-10.2% and TOC 3.0-3.5 wt%). However, the packstone and grainstone facies in the Wolfcamp B stratigraphic unit tends to develop a high secondary porosity (7.8-8.5%) associated with the dissolution vugs, and the carbonate mudstone facies in all units often has a high secondary porosity (2.4-8.1%) from fracturing. Furthermore, the well logs corroborate the heterogeneity of the Wolfcamp intervals. These laboratory-scale test results tied to the well logs and paired with similar studies make an investigation on a broader basin scale possible.

Table of Contents

List of Figures

List of Tables

List of Equations

List of Abbreviations

°C: Degrees Celsius

API: American Petroleum Institute

Avg: Average

bbls: Barrels

BEG: Bureau of Economic Geology

BOPD: Barrels of oil per day

BVH: Bulk volume hydrocarbons

BVW: Bulk volume water

$CaCl_2$: Calcium chloride

CALI: Caliper

Carb: Carbonate

CBW: Clay bound water

CEFMS: Shimadzu Center for Environmental, Forensics and Material Science

cm: Centimeter

CNLS: Compensated neutron limestone porosity

CO_2: Carbon dioxide

CT: Computed tomography

DIW/ DI Water: Deionized Water

DPHI: Density porosity

DT2: N-decane: toluene at 2:1 in volumetric ratio

EIA: U.S. Energy Information Administration

Eq: Equation

Equiv: Equivalent

Fctd: Fractured

FE-SEM: Field emission-scanning electron microscopy

FIB-SEM: Focused ion beam-scanning electron microscopy

FIP: Fluid immersion porosimetry

ft: Feet

g: Grams

GR: Gamma ray

GRI: Gas Research Institute

Hr: Hours

ID: Identification

Inter: Intermediate

IR: Infra-red

JB: James Brown #18-2

k: Permeability

KER: Kerogen

L: Lower

LLD: Laterolog deep

LLS: Laterolog shallow

LS: Limestone

m: Meter

M: Middle

ma: Millions of years

MBOE: Thousand barrel of oil equivalent

Mcf: Thousand cubic feet

MD: Measured depth

mD: milli-darcy

ME: Mary Ellen #1

MICP: Mercury intrusion capillary pressure

Min: Minutes

MIP: Mercury intrusion porosimetry

Miss: Mississippian

ml: Milliliter

mm: Millimeter

MPa: Megapascals

mya: Millions of years ago

N_2: Nitrogen

NaCl: Sodium chloride

nD: Nano-darcy

NGL: Natural Gas Liquids

nm: Nanometer

NMR: Nuclear magnetic resonance

Pa: Pascals

PE: Photoelectric factor

Penn: Pennsylvanian

PHI: Porosity

PI: Production index

Psi: Pounds per square inch

RHOB: Bulk density

Ro: Vitrinite reflectance

S: Source rock

SANS: Small-angle neutron scattering

SAXS: Small-angle X-ray scattering

Sec: Second

SEM: Scanning electron microscopy

SH: Shale

Sph. Spherical

SS: Sandstone

ST: Spanish Trail #41-11

S_w: Saturation of water

THF: Tetrahydrofuran

Tmax: Temperature when the S2 value is the maximum during a pyrolysis analysis

TOC: Total organic carbon

TVD: True vertical depth

TX: Texas

U: Upper

USANS: Ultra small-angle neutron scattering

USGS: United States Geological Survey

UT: University of Texas

V: Volume

Wt: Weight

XRD: X-Ray diffraction

µl: Microliter

µm: Micrometer

Chapter 1: Introduction

1-1 Introduction

An unconventional reservoir is often an oil and/or gas producing formation with low matrix porosity and extremely low permeability. The Wolfcamp Shale is one of the most targeted unconventional plays in the Permian Basin, as a prolific hydrocarbon producing formation. Although the formation has been a known hydrocarbon bearing formation for some time, it was mostly thought of as a source rock due to its low permeability mudrock composition. Rapid advancements in horizontal drilling and hydraulic fracturing made it one of the most targeted formations in the Permian Basin with 1000's of completed wells just in the Midland Basin as of 2017 (Roth, 2018). The Wolfcamp Shale in the Midland Basin should remain a top hydrocarbon target as the USGS estimates that the formation contains 20 billion barrels of oil, 16 trillion cubic feet of associated natural gas, and 1.6 billion barrels of natural gas liquids (Gaswirth et al., 2016).

Though the Wolfcamp is generalized as a shale, it is a very complex and heterogeneous formation composed of several different facies. Each facies' unique composition and characteristics drive the reservoir and source quality that control production performance in different ways. To better understand the relationship between facies and reservoir quality, this study focuses on the petrophysical evaluation of different facies within the Wolfcamp Shale and Spraberry Sandstone in the Midland Basin.

In addition to using standard well log analysis, this study uses laboratory petrophysical evaluation such as MIP and spontaneous fluid imbibition to analyze Wolfcamp rock properties at the nano-scale affecting fluid flow and storage. The property values determined at the nano-scale are then compared to these from well logs to determine how logging tools respond to particular

facies and create corrected log curves based on laboratory results. An attempt to upscale is important to explore the basin on a broader scale, but with precise laboratory-level confidence.

Due to extreme heterogeneity and frequent facies changes, this study uses core samples from various points within the Midland Basin as well as multiple sample depths covering several facies within the Wolfcamp intervals (Figure 1-1). The basin coverage and range of lithology included in the selected samples is necessary to capture the trends of reservoir or source rock properties in the thick, expansive, and heterogeneous Wolfcamp intervals.

Though difficult to examine the entirety of the Wolfcamp with one study, this study provides valuable information supplementing similar studies for a better understanding of the Wolfcamp to aid in developing detailed regional models to benefit exploration and exploitation. Not only will this study improve the understanding of the Wolfcamp formation in the Midland Basin, but also it will provide valuable information regarding the evaluation techniques of unconventional reservoirs. Unconventional reservoirs have not been studied to the degree of conventional reservoirs. Thus, there is no standardization of evaluation techniques for low matrix permeability mudstone reservoirs. Determining the petrophysical properties of these mudstone reservoirs using a variety of laboratory methods is important for developing a standardized set of analyses and it may further progress of evaluation techniques needed to accurately and quickly describe shale rock formations.

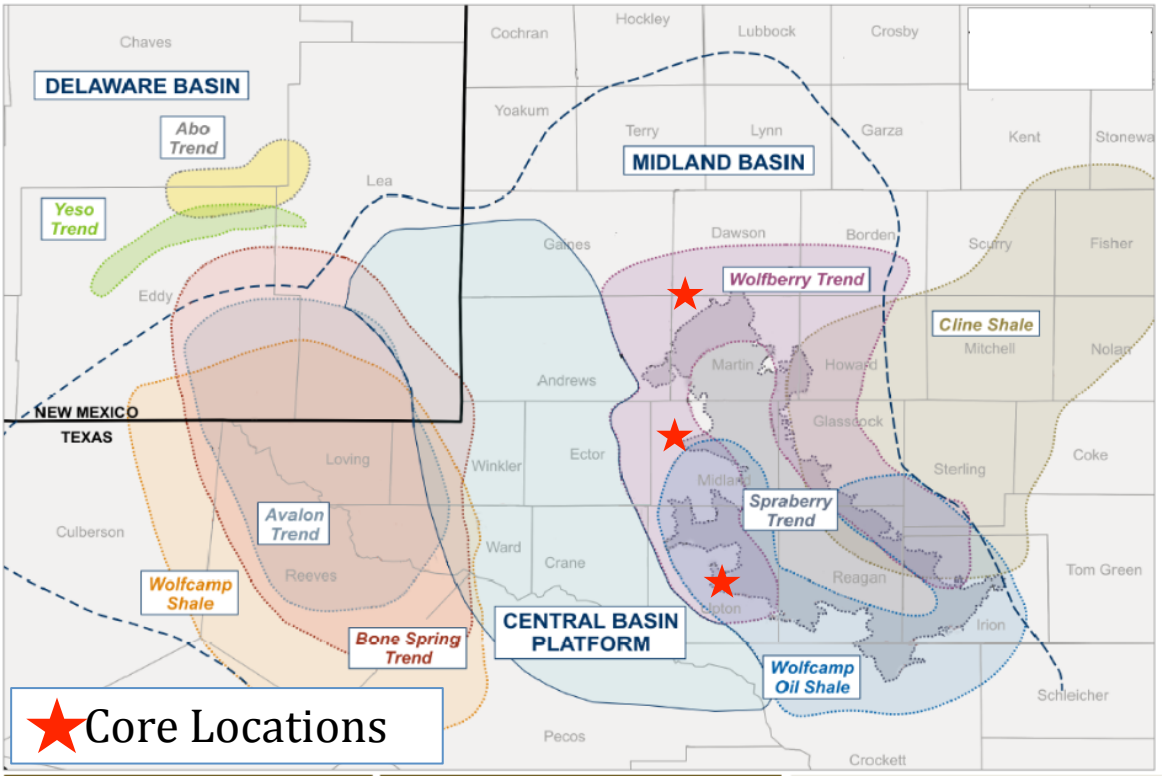

Figure 1-1: Permian Basin hydrocarbon play trend map with core locations highlighted by red stars (modified after 7S Oil and Gas, LLC from Jarvie, 2018).

1-2 Study Location

This study's focus is Wolfcampian and Leonardian stratigraphic units within the Midland Sub-basin of the Greater Permian Basin of West Texas and South Eastern New Mexico. Within these stratigraphic units, samples were taken from the Permian-aged Lower Spraberry and Wolfcamp Shale units A, B, C, and the Pennsylvanian-aged Wolfcamp D. Samples consist of core plugs from three wells that run in a north-south direction down the West Central portion of the Basin (Figures 1-1 and 1-2). These three wells are the James Brown #18-2 (API# 4211533474) in the southwestern corner of Dawson County, Texas, the Spanish Trail #41-11 (API# 4232936005) in North West Midland County, Texas, and the Mary Ellen #1 (API# 4246135783) in South central Upton County, Texas (Figure 1-2).

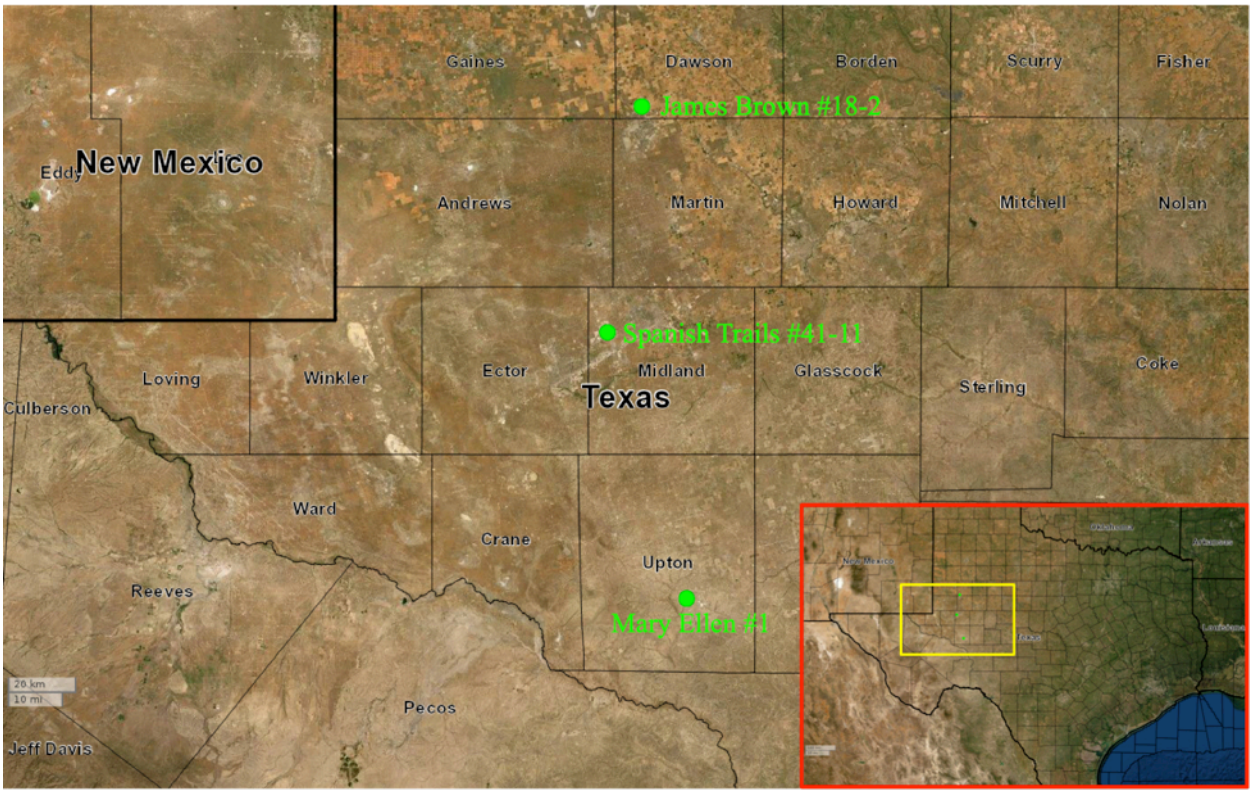

Figure 1-2: Locations and names of three wells that were sampled with satellite imagery base map showing state and county outlines (base map from DrillingInfo, 2019).

1-3 Previous Work

Detailed shale properties are difficult to obtain using conventional techniques. In recent years, high-resolution tools combined with conventional reservoir characterization technologies were adopted for shale research (e.g., Lu et al., 2016; Sondergeld et al., 2010). High-resolution imaging techniques, such as field emission-scanning electron microscopy (FE-SEM), focused ion beam-scanning electron microscopy (FIB-SEM), micro- and nano-CT imaging (computed tomography), are integrated with petrophysical methods like mercury intrusion porosimetry (MIP), N_2 and CO_2 physisorption isotherm, spontaneous imbibition, gas diffusion, nuclear magnetic resonance (NMR), small-angle X-ray scattering (SAXS), small and ultra-small-angle neutron scattering (SANS and USANS) (Wang, 2019). These imaging and petrophysical

methods give researchers more versatile tools to investigate nano-petrophysical parameters that affect fluid storage and flow in shale formations. Key parameters to examine when investigating fluid flow in shale formations are pore structure, permeability, and tortuosity.

Porosity, pore type, and pore size distribution are pore structure parameters important to the evaluation of heterogeneous reservoirs. SEM, CT, gas physisorption, MIP, helium pycnometry, fluid immersion porosimetry (FIP), and NMR are currently among the most common pore structure characterization methods (Rodriguez1 et al., 2014; Li et al., 2019). FE-SEM can be used to image the shale pore space at a spatial resolution of about 5 nm. Porosity can be determined by helium pycnometry, FIP, and MIP. Out of the three listed, MIP is the most functional method to measure porosity as well as determine pore-throat distribution and pore volumes over micrometer to nanometer ranges. Currently, two popular methods for permeability determination of a shale matrix are gas expansion and MIP (Cui et al., 2009). Finally, MIP can assist in characterization of another important petrophysical parameter, tortuosity. Simply put, tortuosity is the fraction of traveled distance over a straight line between two points (Schlumberger Oilfield Glossary, 2019). It can reflect the complexity of pore space and hydrocarbon pathway morphology (Ghanbarian et al., 2013). CT, acoustic absorption, reflection wave, diffusion diaphragm, and MIP are several methods used to determine the tortuosity of a shale matrix (Fellah et al., 2003; Hu et al., 2017).

1-4 Objective of Study

The objective of this study is to use laboratory petrophysical evaluation to gain insight on how the different depositional facies affect reservoir quality in Midland Basin Wolfcamp intervals. With these lab-scale test results tied to well logs, an investigation at a broader basin scale is possible. To characterize different Wolfcamp Shale and Spraberry Sandstone facies,

vacuum-assisted FIP, fluid displacement, fluid imbibition, LECO-TOC, pyrolysis, XRD, contact angle, and MIP tests will be conducted to investigate porosity, organic geochemistry, mineral composition, wettability, permeability, and tortuosity. The choice of fluids used in these tests includes deionized water, DT2, and THF, to examine the wettability effects of shale pore space.

Chapter 2: Geologic Background

2-1 Structural Setting

2-1-1 Permian Basin Architecture

The Permian Basin of West Texas and Southeast New Mexico is a Northwest to Southeast trending asymmetrical sedimentary system widely known for its stratified hydrocarbon targets. The Greater Permian Basin is one of the largest and most structurally complex basins in North America (Sutton, 2014). The Basin covers an area of over 75,000 miles^2 across 52 counties in Texas and New Mexico (Sutton, 2014; EIA, 2018). The Permian Basin is bounded by the Appalachian-Marathon-Ouachita orogenic belt to its south, the Northwest shelf and Matador Arch to its north, the Diablo platform to its west, and the Eastern shelf to its east (Hills, 1985; Gardiner, 1990; Ewing, 1991). The Basin is currently composed of several sub basins and platforms that are divided into three main subdivisions; the Delaware Basin in the west, the Midland Basin in the east, and the Central Basin Platform separating the two (EIA, 2018). The Permian Basin as a whole was originally an open marine area known as the Tobosa Basin in the middle Carboniferous (325-320 Ma, millions of years) (Galley, 1958) (Figure 2-1). The Tobosa Basin was characterized as a broad, shallow, gently dipping depression that developed due to an asymmetric structural flexure in the Precambrian basement caused by sediment loading at the southern margin of the North American plate from the Cambrian to Mississippian periods (541 to 323 mya) (Beamont, 1981; Jordan, 1981; Alnaji, 2002; Sutton, 2014). The Pangea forming

collision of Laurasia and Gondwana from the late Mississippian through the Pennsylvanian (310 to 265 mya) gave rise to the Ouachita-Marathon fold belt, part of the Appalachian-Ouachita-Marathon orogeny, and deformed the ancient Tobosa Basin along high angle basement faults and pre-existing zones of weakness (Horak, 1985) (Figure 2-1). The continued, large, collision linked, thrust faults related to the Ouachita-Marathon orogeny created sizeable amounts of uplift or crustal thickening. This resulted in tectonic loading and lithospheric flexure directly related to the subsidence of the foreland basin, now known as the Permian Basin. The Ancestral Rocky Mountains intracratonic deformation development during the Pennsylvanian-earliest Permian is also a heavy influencer of the Permian Basin development (Soreghan et al., 2012). Although the cause for the Ancestral Rocky Mountains is debated, a common interpretation is association with far-field compression from the Ouachita-Marathon orogeny (Soreghan et al., 2012). During this collision and subsidence the Permian Basin area remain covered by a seaway (Sutton, 2014) (Figure 2-1). In the late Mississippian, vertical movement, associated with the Ouachita-Marathon orogeny along the Proterozoic lines of weakness, deepened the eastern incipient Delaware Basin along the Central Basin Platform, which was undergoing uplift along redeveloped thrust faults caused by a compression associated with the orogeny (Alnaji, 2002) (Figure 2-1). This resulted in the splitting of the Basin into its three sub-divisions; Delaware Basin, Central Basin Platform, and Midland Basin.

2-1-2 Midland Basin Architecture

The Midland Basin is the focus of this thesis with all samples coming from wells in this Basin. The Midland Basin is bounded on its east by the Eastern shelf, to the west by the Central Basin Platform, and to the north by the Northern shelf (Figure 2-5). These boundaries caused a restricted setting with only the Sheffield and San Simon channels connecting it to the Delaware

Basin (Figure 2-5). The tectonic history of the Midland Basin is mostly affected by the uplift of the Central Basin Platform, thrusting of the Marathon-Ouachita orogenic belt, and the Ancestral Rocky Mountains (Soreghan et al., 2012; EIA, 2018). In the early Pennsylvanian, clastic supplies within the Permian Basin were limited, but starting in the Pennsylvanian the Basin underwent rapid subsidence at the western boundary evidenced by sudden changes in thickness and lithology of the Pennsylvanian to Permian strata as well as the Strawn carbonates unconformably overlying the Paleozoic strata in the fault zone around the Central Basin Platform (Alnaji, 2002; EIA, 2018) (Figure 2-1). This stage of tectonic activity lasted until the middle Triassic when the subsidence in the Basin slowed and eventually stopped (EIA, 2018) (Figure 2-1).

During this tectonic activity, the combination of rapid basin subsidence and rapid uplift of its margins provided the accommodation and clastic sources that would feed the Midland Basin (Alnaji, 2002). The equidistant Midland Basin accumulated clastics associated with deep-water environments. In addition, from the middle to late Pennsylvanian, a shallow, broad, carbonate shelf and margin developed, which formed reefs around the seaward edges of the shelves during stages of still-stand or slow subsidence (Alnaji, 2002; Sutton, 2014) (Figure 2-1). Along the western edge, against the Central Basin Platform, coarse sediments associated with the shallow reef environments were deposited (Sutton, 2014). This carbonate Central Basin Platform uplift is the main sediment provenance for the Midland Basin (Quintero, 2016). From the middle to late Permian, the Midland Basin was principally a site of rapid variable sedimentary filling with fluvial-deltaic siliciclastic sediments along with the development of extensive reef fringed carbonate/evaporite platforms and shelves (Alanji, 2002) (Figure 2-1). During the late Permian, the basin ceased to accumulate carbonates and instead became a site of cyclic deposition of sandstone, anhydrite, and halite (Ward et al., 1986). Basin subsidence slowed considerably in the

late Permian and the Permian Basin was tectonically stable, providing stability for sediment compaction (Oriel et al., 1967; Robinson, 1988; Yang and Dorobek, 1995; Alnaji, 2002). Since the late Permian, the Midland Basin has been affected by the Laramide orogeny from the late Cretaceous to early Tertiary and igneous intrusions from the Eocene to Oligocene (Zoeten, 2017) (Figure 2-1).

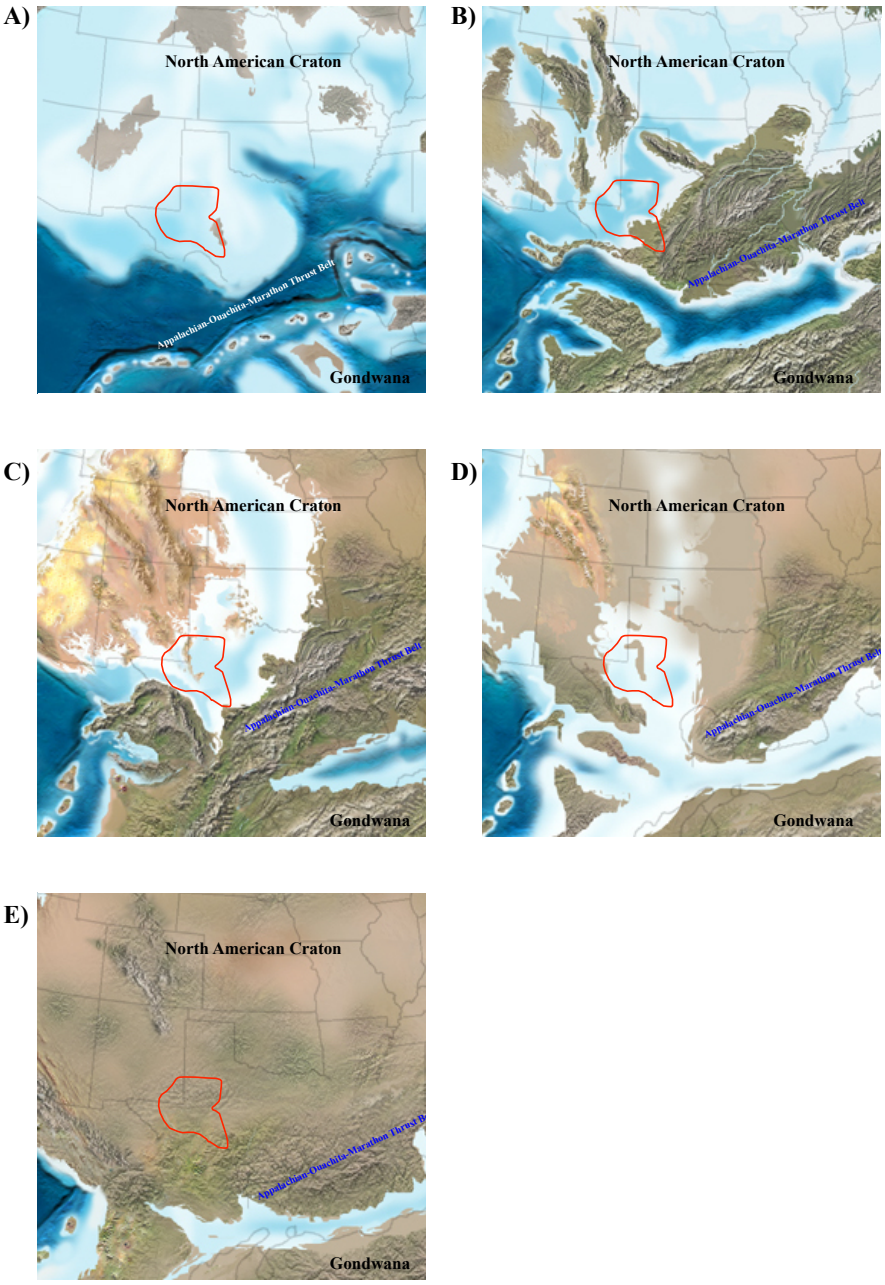

Figure 2-1: Paleogeographic reconstructions exhibiting the southern part of North America with the Permian Basin outlined in red. A) Early Miss. (345 Ma); B) Late Penn. (300 Ma); C) Early Permian (290 Ma); D) Late Permian (260 Ma); E) Middle Triassic (230 Ma) (modified after Blakey, 2011).

2-2 Stratigraphy and Depositional Environment

2-2-1 Introduction

Within the stratigraphic framework of the Midland Basin, the Wolfcampian and Leonardian aged Wolfcamp Shale, Dean Sandstone and Spraberry Formation is the focus of this thesis as all samples come from intervals within these units (Figure 2-2). These formations, sometimes collectively called the Wolfberry, were mostly deposited in toe-of-slope depositional positions throughout the Midland Basin and comprise organic-rich, transgressive basinal mudstones interbedded with siliciclastic and carbonate debrite and turbidite beds (Gardner et al., 2017). The Wolfcamp Shale is dominated by mudstone interbedded with limestone and minor fine-grained sandstones, though vertical and lateral heterogeneities are common. The Wolfcamp can be subdivided into several units that generally have comparable facies (Figure 2-2). Each Wolfcamp and Spraberry unit is unique with respect to reservoir pressure, mineralogy and petrophysical properties (Waite, 2019). The Wolfcampian and Leonardian strata was deposited during periods of long-term lowstands and highstands as a result of multiple forcing factors (Waite, 2019). The difference in depositional stages from highstand carbonates and deep-sea fines to the lowstand channel fan complexes resulted in Spraberry depositional rates being ten times Wolfcamp units (Waite, 2019).

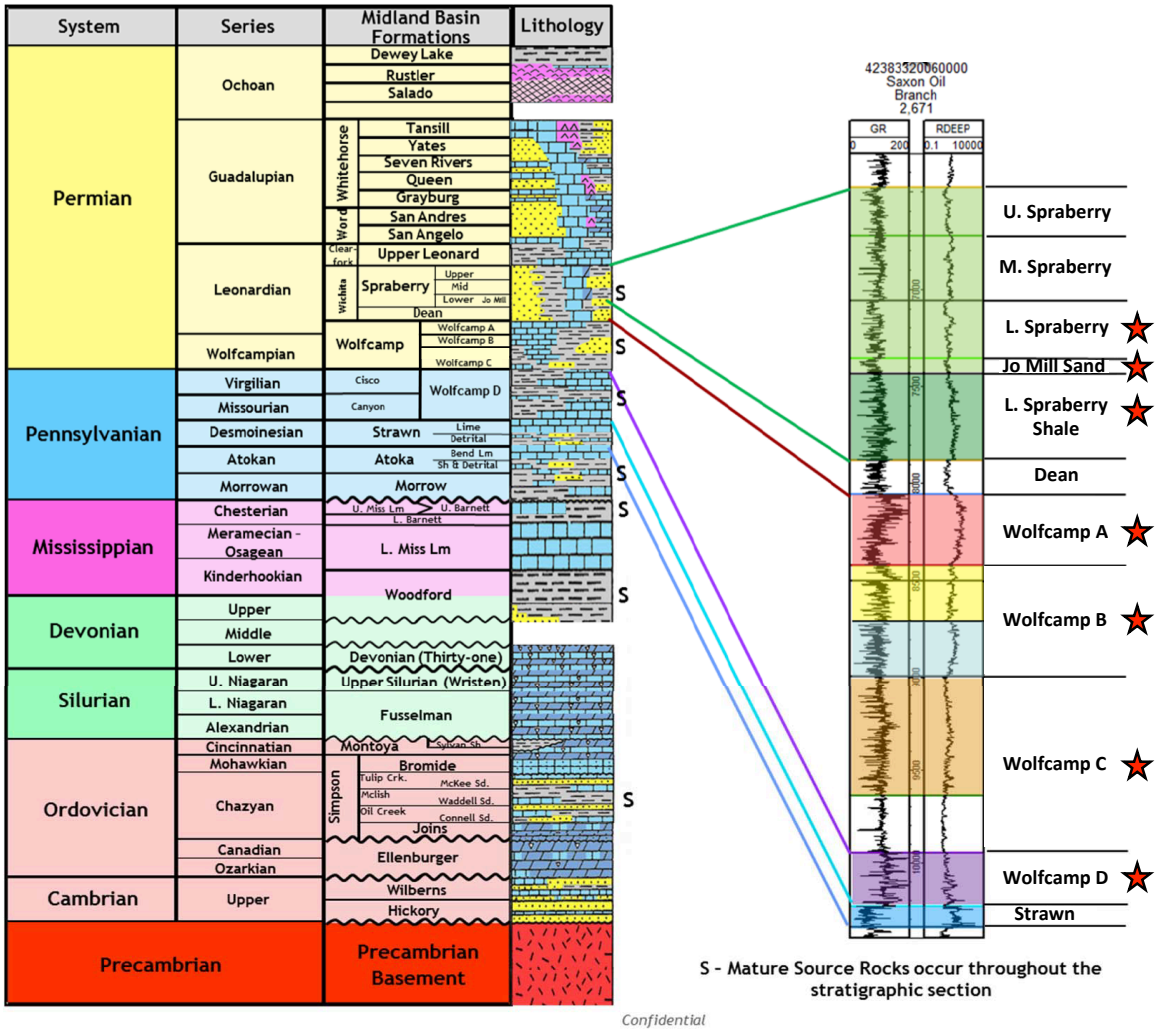

Figure 2-2: Stratigraphic column of the Midland Basin from Precambrian to Permian with type log GR and resistivity over study intervals (modified after Pioneer, 2014). Red stars indicate sampled intervals.

2-2-2 Wolfcamp

Overlying the shallow water carbonates of the Strawn limestone is the Wolfcamp shale, largely a two lithology system dominated by laminated mudstones interbedded with argillaceous carbonate debrites with minor layers of calcareous sandstone (Wilson, 1975; Mazzullo and Reid, 1989; Walker et al., 1991; Hamlin and Baumgardner, 2012; Sutton, 2014; Blomquist, 2016; Gardner et al., 2017). The base is late Pennsylvanian icehouse and the unit lasted thru the Early Permian Wolfcampian greenhouse period (Waite, 2019). This interval can be separated into four

units; the Pennsylvanian Wolfcamp D (Canyon, Cisco), Permian Wolfcamp C, Permian Wolfcamp B, and Permian Wolfcamp A, where strata mainly consists of carbonate facies in the peripheral areas that grades down to a toe of slope fine-grained siliciclastic facies in the deeper equidistant basin with abrupt lateral changes and cyclical variation (Blomquist, 2016; Gardner et al., 2017; EIA, 2018) (Figures 2-2 and 2-5). These facies are described as gravity-flow deposited muddy carbonate-clast conglomerate, gravity-flow deposited skeletal packstone/grainstone, hemipelagic deposited siliceous mudrock, and hemipelagic deposited calcareous mudrock (Hamlin and Baumgardner, 2012) (Figure 2-5).

The Carboniferous to Permian Wolfcamp deposition was a time of continental glaciation that drove high amplitude, high frequency, eustatic, sea-level changes that controlled sediment input (Heckel, 1986; Veevers and Powell, 1987; Fielding et al., 2008). The sediment deposited during regional lowstands are from erosion of exposed, uplifted highlands and reached the deeper basin by gravity flow processes (Ward, 2017) (Figure 2-3). During regional sea-level highstands, the uplifted highlands are flooded and turned into carbonate factories with sediments transporting into the basin being mostly carbonate derived from these platforms (Ward, 2017) (Figure 2-3). Hemipelagic, windblown silt, clay and organics would have been present in the depositional system throughout the sea level cycles and in all intervals (Hamlin and Baumgardner, 2012) (Figure 2-4).

A simultaneous deposition of organic-rich carbonate and clastic sediments in an anaerobic basin results in hydrocarbon-rich, interbedded, conventional and unconventional reservoirs with an average porosity of 7% and permeability as low as 10 nD (Pioneer, 2014; Blomquist, 2016; Gardner et al., 2017). The present-day depth of the Wolfcamp varies with structural position, from the axis of the basin around 11,000 ft deep and shallowing toward the

basin margins from 4,000 ft to 7,000 ft deep (Sutton, 2014; Blomquist, 2016). Thickness varies as well from 185 ft to 4000 ft thick, with an average thickness of ~1500 ft (Blomquist, 2016).

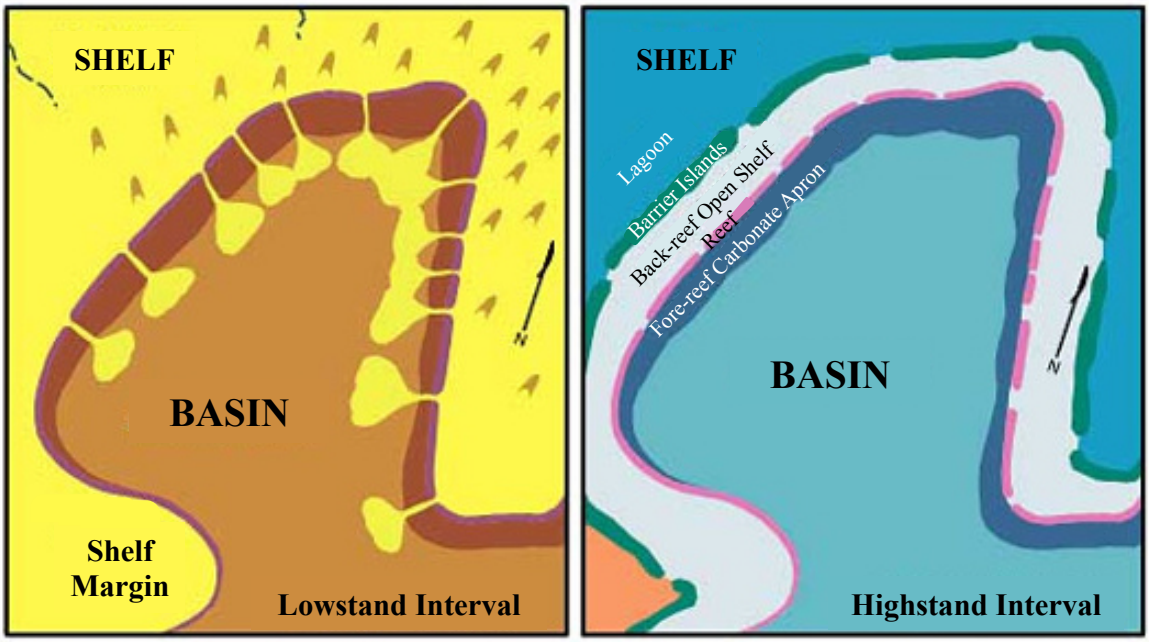

Figure 2-3: Typical basin deposition model showing siliciclastics being deposited in the lowstand intervals and carbonates on the basin shelf during the highstand intervals (modified after Scholle, 2002).

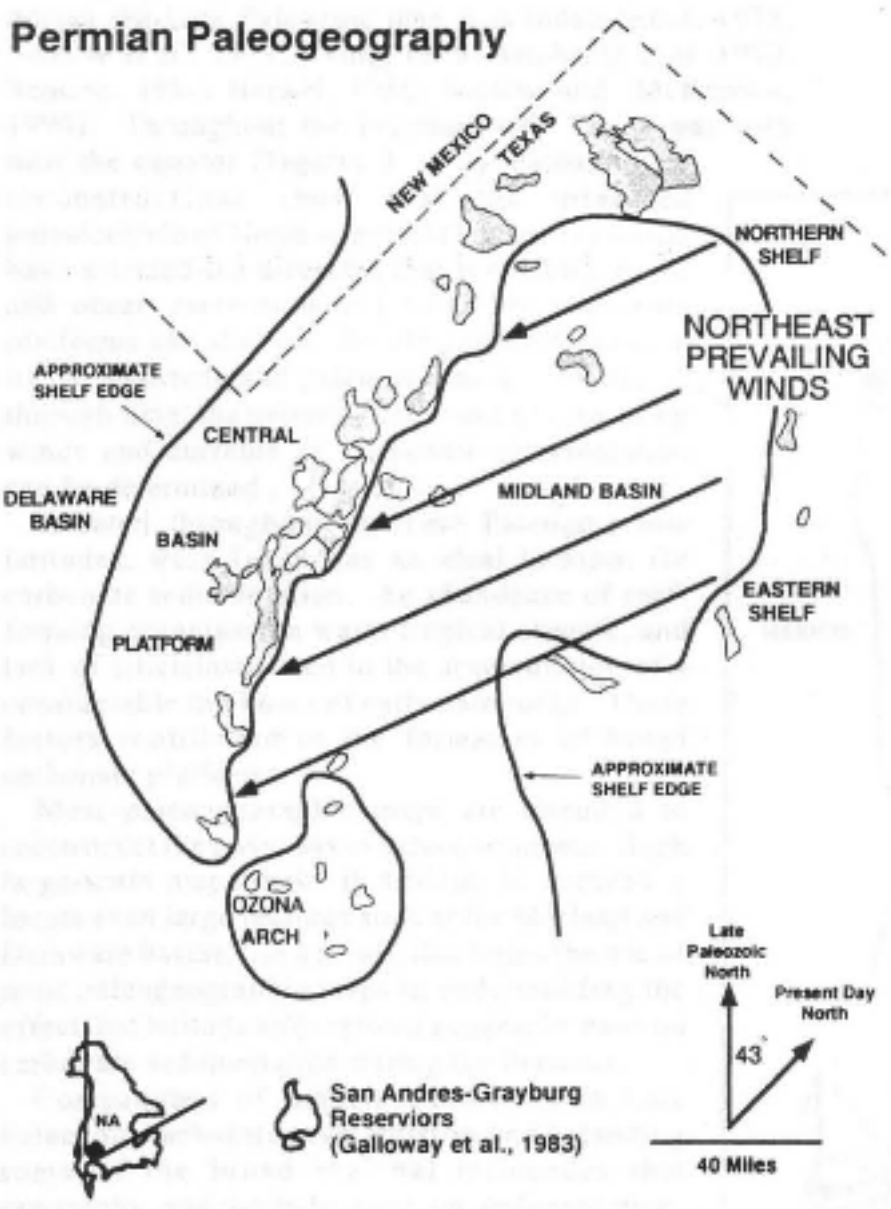

Figure 2-4: Permian paleogeographic map showing the Midland Basin and surrounding structures highlighting the wind direction at this time, depositing wind-blown hemipelagic siliciclastic sediments into the Basin (Galloway et al., 1983).

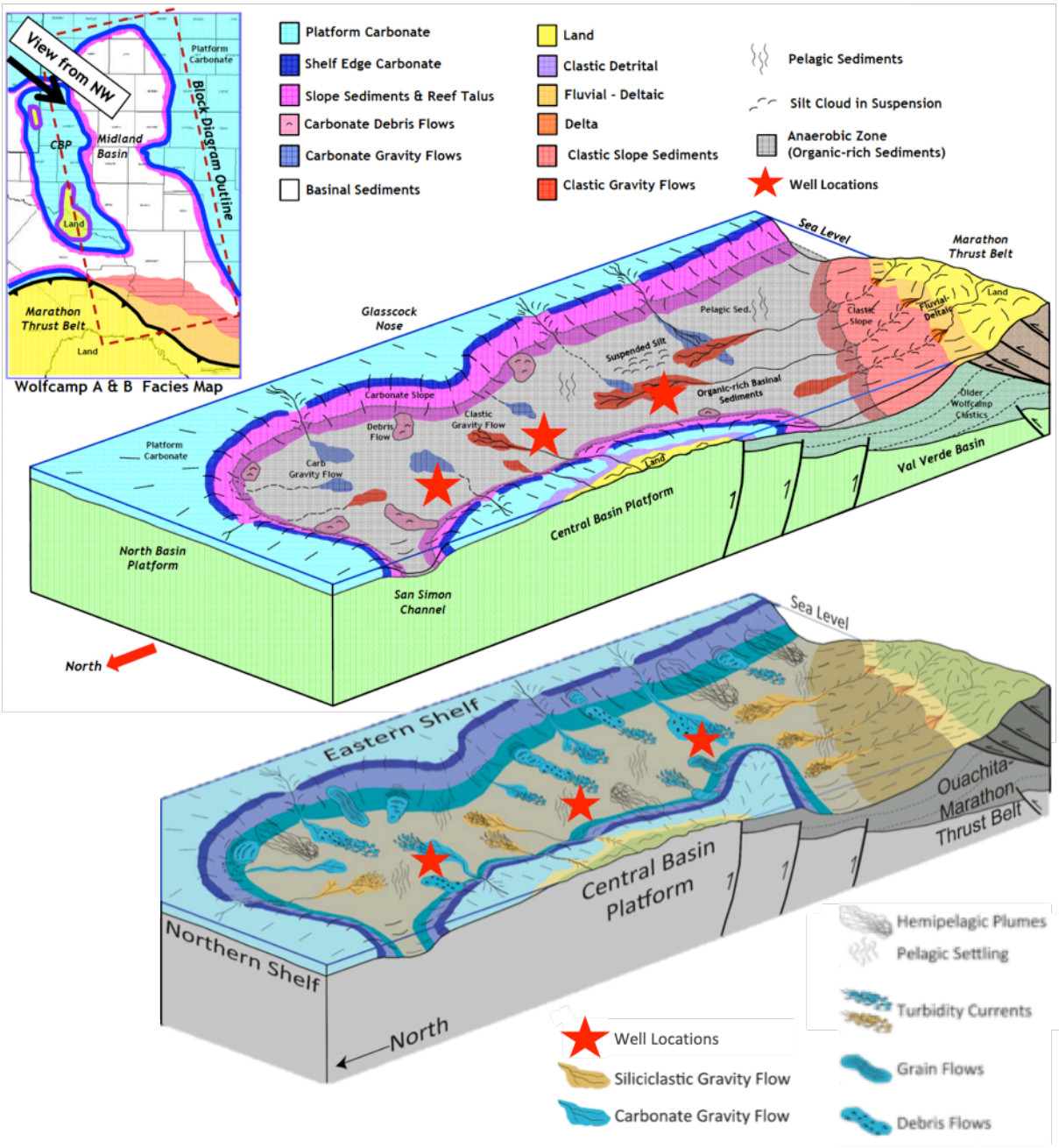

Figure 2-5: Two separate Midland Basin depositional and structural models showing possible depositional processes and relative locations during Wolfcampian-Leonardian time with well locations highlighted by red stars (modified after Hanford, 1981; Ward, 2017; Pioneer, 2014).

2-2-3 Dean and Spraberry

Directly after the Wolfcamp, the Leonardian Dean and Spraberry intervals were deposited, marking a shift in basin evolution from lowstand/highstand carbonate shale deposition

to lowstand clastic deposition via a large influx of sand and silt-rich deepwater fan systems (Waite, 2019). These intervals are broken into six units; The Dean sandstone, Leonard shale (Lower Spraberry shale), Jo Mill sand, Lower Spraberry, Middle Spraberry, and Upper Spraberry with major and minor deepwater channel fan systems throughout (Waite, 2019) (Figure 2-2).

The channel systems and submarine fans that deposited Dean and Spraberry sediment formed during a regional lowstand due to a relative low sea-level period. During this low stand sediments sourced from uplifted highlands on basin margins, in particular the Northern shelf, were heavily deposited near the basin margins as well as the distal basin depocenter via submarine canyon channel fan complexes (Pioneer, 2012) (Figure 2-3). Associated with these channel fan complexes, the Spraberry-Dean combination is largely interbedded, fine-grained, silty sandstone, calcareous mudstone, coarse siltstone, and silty mudstone characterized by low porosity, low matrix permeability, and a natural fracturing tendency (Sutton, 2014).

The present-day depth of the Spraberry formation varies by structural position, but average approximately 7,000 feet across the Midland basin (Sutton, 2014). The Dean is significantly thinner than the Spraberry at about 100-200 feet, and the entire section from the top of the Spraberry to the base of the Dean varies in thickness between 1,200 and 1,900 feet (Sutton, 2014).

2-3 Petroleum Potential of the Wolfcamp Midland Basin

The Wolfcamp Shale is a well-known unconventional reservoir in the Permian Basin, which is deemed unconventional due to the source and reservoir sharing the same system of storage and deliverability. The source rock potential directly impacts the amount of recoverable hydrocarbons within this unconventional reservoir. Evaluating the total organic carbon (TOC), kerogen type, thermal maturity (vitrinite reflectance, Ro), and thickness can lead to a better

determination of the source rock quality and petroleum potential of the unconventional reservoir. Though important, organic quality does not alone define reservoir quality.

When organic material, accumulates in deep, poorly oxygenated areas of a basin, as such in the Permian Midland Basin, they can be converted to hydrocarbons via thermogenic stress. The amount of organic carbon can be measured and reported as TOC wt%. The TOC range in the Wolfcamp intervals is from less than 2.0 wt% to as high as 8.8 wt% (Ward, et al., 1986; Blomquist, 2016; Kvale and Rahman, 2016; Rodriguiez, 2017; EIA, 2018). Organic deposition and preservation is related to flooding surfaces and is facies-dependent, where it is the highest in siliceous mudrocks, reaching 8.0 wt% (Baumgardner et al., 2014; EIA, 2018). The TOC ranges from 0.6 wt% to 6.0 wt% in carbonate turbidites and is usually less than 2.0 wt% in siliciclastics turbidites (EIA, 2018). High quality source rocks typically contain 2.0 wt% TOC or higher, giving the organic-rich Wolfcamp intervals a high petroleum potential (Blomquist, 2016; EIA, 2018).

The kerogen type present in a source formation impacts the type of hydrocarbon generated when the formation is thermally maturing. The Wolfcamp oils were mostly generated from oil prone, marine derived type II kerogens with a smaller contribution from gas prone, terrestrial derived type III kerogens (Kvale and Rahman, 2016; Gupta et al., 2017).

The thermal maturity of a source rock dictates if the source is or was ever mature enough to generate hydrocarbons and can be measured using vitrinite reflectance (%Ro). Vitrinite reflectance is a direct microscopic measure made on the macerals extracted from the kerogen in the source rock and is dependent on the kerogen type (Worley, 2017). Typically, Ro% values < 0.6 are found in immature source rock, Ro% values 0.6 to 1.2 are in the oil window, and Ro%

values > 1.2 are in the gas window (Rowan, 2006). The Wolfcamp Shale has a %Ro from 0.85 to 0.90%, which puts it in the oil window (Rodriguez, 2017).

The thickness of a source rock can dictate how much organic material is available for generating hydrocarbons and, in this case, how thick the reservoir pay intervals are. As discussed in Section 2-2-2, the thickness of the Wolfcamp Shale intervals varies, but on average is about 1500 ft thick, although not all 1500 ft is source rock, this is a large interval for hydrocarbon development (Blomquist, 2016). The thickness is used, in combination with other properties to calculate resource volume, such as oil-in-place and natural gas-in-place estimates. As stated in the introduction, the USGS estimates the Wolfcamp formation in the Midland Basin to be in excess of a technically recoverable 20 billion barrels of oil, 16 trillion cubic feet of natural gas, and 1.6 billion barrels of natural gas liquids (NGL), making it one of the largest hydrocarbon plays in the United States (Gaswirth et al., 2016).

2-4 Oil and Gas Production of the Wolfberry Play

Since reservoir stimulation methods have advanced the Permian Wolfcampian and Late Pennsylvanian Wolfcamp Shales, have been heavily targeted for hydrocarbon production (Figure 2-6). Based on size, source/reservoir quality, and stacked pay zones, the Wolfcamp Play is one of the largest resource plays in the world (Blomquist, 2016). Deposited after Wolfcamp intervals, Permian Leonardian Dean and Spraberry sandstones, known together as the Spraberry Trend, have been producing since the 1940's (BEG, 2019). The Spraberry Trend productive area spans 18 counties in West Texas and contains more than 10 Bbbl of oil (BEG, 2019) (Figure 2-6). When the Wolfcamp and the overlying Spraberry formations are combined it creates an expanded productive interval known informally as the Wolfberry Play (Blomquist, 2016; BEG, 2019).

Most current drilling activities in the Delaware and Midland Basins target the Wolfcamp A and B benches rather than Wolfcamp C and D benches, which are more mature, natural gas prone intervals (Blomquist, 2016; EIA, 2019) (Figure 2-6). Coarser-grained portions of the Wolfcamp make for obvious reservoirs, but the fine-grained carbonate and siliceous mudstone facies are also productive after fracture stimulation (BEG, 2019). Hydraulic fracturing enhances these low-permeability, organic-rich formations to produce econmically (BEG, 2019). Over 5,800 Wolfberry oil wells have been completed since the late 1990s (BEG, 2019). The initial production averages 1000 to 1500 BOPD, and ultimate per-well recovery can be in excess of 750 MBOE.

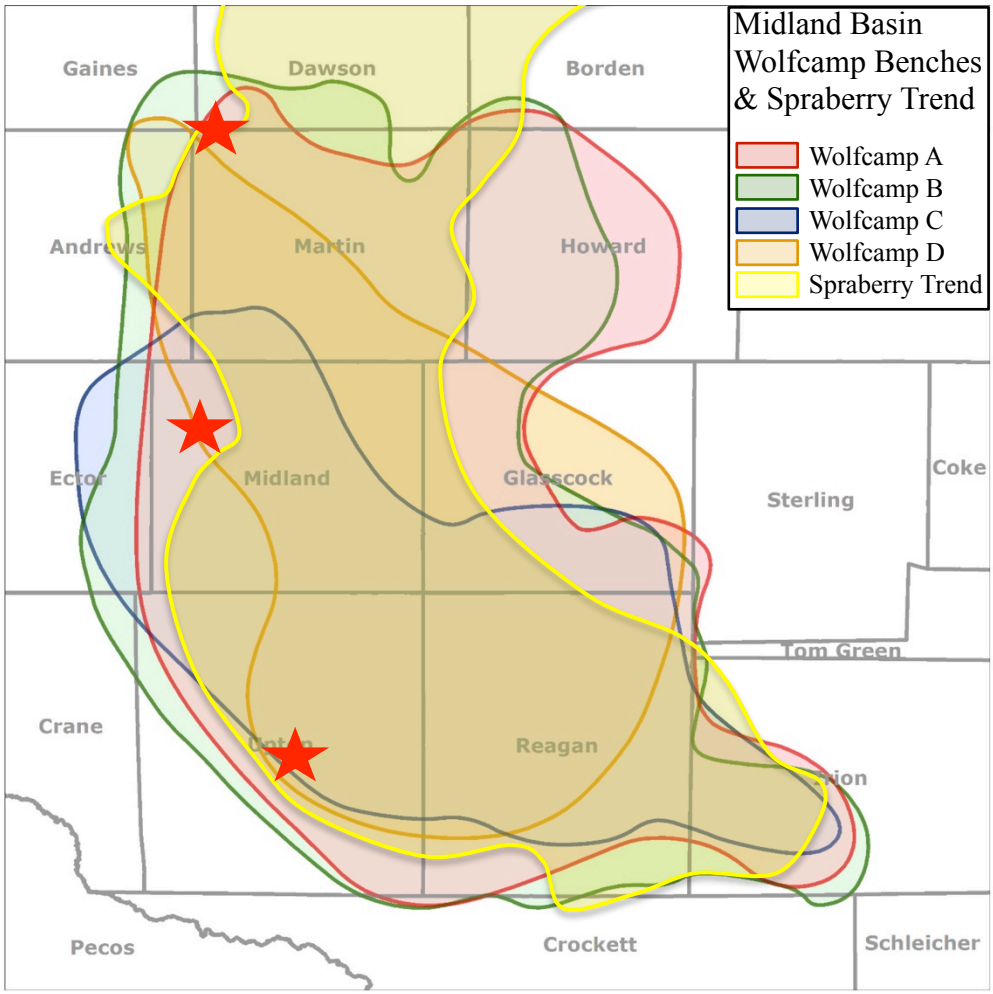

Figure 2-6: Wolfcamp and Spraberry trends in the Midland Basin with core locations highlighted by red stars (modified after Abramov and Mlada, 2017)

Chapter 3: Methods

3-1 Sample Acquisition and Information

Diamondback Energy donated core samples and well logs from three wells in the Midland Basin to investigate the petrophysical properties of the Wolfcamp and Spraberry in this study. Core plugs were taken from core in three wells; Mary Ellen 1 in Upton County, James Brown 18-2 in Dawson County, and Spanish Trail 41-11 in Midland County. These wells were chosen based on location being spread north to south spanning the basin to test multiple areas of the basin and determine if trends exist (Figure 1-1). The core plug points were chosen by myself

with assistance by Dave Cannon (Diamondback VP Geoscience) at Core Lab's facility in Houston, TX. Points were chosen by visually interpreting the different facies distributed in the slab. The intended objective was to choose facies end-members in each formation in each well so a determination of any potential trends based on facies, formation, and/or location could be identified.

The 1-inch core plugs for the Mary Ellen and Spanish Trail wells were cut from the slab butt end by Core Lab. The slab butt end for the James Brown well was donated to BEG and is located at their Midland, TX facility. After meeting with Andy Faigle, the Manager of BEG Midland Core Research Center, the James Brown 1-inch plugs were cut as well. Each core plug was assigned a sample ID based on an abbreviation of the well name followed by the corresponding depth (ft) of the plug (Table 3-1).

Table 3-1: Well names, sample identification and information. For sample ID; ME: Mary Ellen #1, ST: Spanish Trail #41-11, JB: James Brown #1-2, and the number corresponds to depth in ft.

Well Name	API	County	Sample ID	Depth (ft)	Formation	Age	Facies
Mary Ellen #1	4246135783	Upton	ME-8004	8,004.05	Lower Spraberry	Permian	Siliceous
			ME-8027	8,027.17			Siliceous-Rich Carbonate
			ME-8045	8,045			Carbonate Dominated
			ME-8063	8,063.17			Shale
			ME-8435	8,435.75	Wolfcamp A		Detrital Carbonate-Rich Shale
			ME-8444	8,444.84			Shale
			ME-8455	8,455.15			Shale
			ME-8463	8,463			Shale
			ME-8621	8,621			Detrital Carbonate-Rich Shale
			ME-8633	8,633.35			Clay-Rich Siliceous Shale
			ME-8832	8,832.90	Wolfcamp B		Shale
			ME-8852	8,852			Shale
			ME-8866	8,866.75			Detrital Carbonate-Rich Shale
			ME-9031	9,031.10			Carbonate Dominated
			ME-9039	9,039.05			Carbonate Dominated
			ME-9044	9,044.05			Carbonate Dominated
			ME-9052	9,052			Vuggy Carbonate
			ME-9197	9,197.35	Wolfcamp C		Detrital Carbonate-Rich Shale
			ME-9207	9,207			Clay-Rich Carbonate
			ME-9509	9,509	Wolfcamp D Cisco	Pennsylvanian	Shale
			ME-9511	9,511.05			Carbonate Dominated
			ME-9528	9,528.84			Clay-Rich Carbonate
Spanish Trail #41-11	4232936005	Midland	ST-8441	8,441.10	Spraberry	Permian	Carbonate-Rich Siliceous Rock
			ST-8877	8,877	Jo Mill		Carbonate-Rich Siliceous Rock
			ST-9400	9,400.15	Lower Spraberry		Carbonate-Rich Shale
			ST-9605	9,605.60	Wolfcamp A		Shale
			ST-9612	9,612.50			Carbonate Dominated
			ST-9632	9,632.20			Carbonate-Rich Siliceous Shale
			ST-9833	9,833.75	Wolfcamp B		Carbonate-Rich Shale
			ST-9841	9,841			Vuggy Carbonate
			ST-9849	9,849			Clay-Rich Siliceous Rock
			ST-10053	10,053	Wolfcamp C		Shale
			ST-10067	10,067.30			Shale
			ST-10310	10,310.40	Wolfcamp D Cisco	Pennsylvanian	Shale
			ST-10318	10,318			Carbonate-Rich Shale
			ST-10322	10,322.40			Shale
James Brown #18-2	4211533474	Dawson	JB-9187	9,187.60	Lower Spraberry	Permian	Clay-Rich Siliceous Rock
			JB-9209	9,209.30			Carbonate-Rich Shale
			JB-9733	9,733.30	Wolfcamp A		Detrital Carbonate-Rich Shale
			JB-9781	9,781.10	Wolfcamp B		Clay-Rich Siliceous Rock
			JB-9849	9,849.50			Shale
			JB-9867	9,867.30			Detrital Carbonate-Rich Shale
			JB-9871	9,871.80			Carbonate Dominated
			JB-9891	9,891.60			Carbonate-Rich Shale
			JB-9904	9,904			Shale
			JB-10525	10,525.60	Wolfcamp D Cisco	Pennsylvanian	Carbonate-Rich Shale
			JB-10570	10,570.60			Shale
			JB-10595	10,595.60	Wolfcamp Canyon		Carbonate-Rich Shale

3-2 Sample Processing

When all core plug samples were received and assigned a unique sample ID, pictures were taken of the plugs using a digital camera (slab photos were taken at the Core Lab facility

when sample points were being picked) (Figure 3-1 and Appendix D). Core plugs, at 2.54 cm in diameter and 5-10 cm in height, were measured and weighed to determine dimensions and mass before any testing took place. The plugs were dried in a 60°C oven for two days to remove moisture, then non-destructive tests, DI water FIP and DI water displacement, were conducted on all plugs. After the completion of the initial plug tests, the samples were further processed by cutting into smaller sizes using a Hi-Tech Diamond Rock Saw (Figure 3-2). A 3 cm portion of each plug was removed for helium porosity and permeability tests in the future.

Several representative samples from each well totaling 18 samples out of the initial 48 were selected based on facies and formation to undergo further testing. These samples were cut into as many (~6-12) $1cm^3$ cubes as the sample size would allow (Figure 3-3). These cubes were used for FIP, fluid displacement, imbibition, and MIP experiments. One cube from each sample was cut into ~2 mm-thick thin slabs for contact angle and wettability testing. The exposed surfaces of the cubes and thin slabs were polished using sandpaper with a measured surface roughness of 2.29±0.08 μm. The cubes being used for imbibition were then epoxied using Hardman Double/Bubble Transparent Epoxy on 4 continuous faces to allow fluid flow in one desired direction, which is parallel to the bedding plane (Figure 3-3).

The remainder of the sample, as well as the saw cuttings from cubes and thin slabs, were used to acquire six separate crushed sized samples for GRI+ (Gas Research Institute) down to powder size (Table 3-2). To crush the sample, larger pieces were broken down with a hammer and all was eventually ground using a mortar and pestle, although a few samples were ground momentarily using an electric grinder (Figure 3-4). Once crushed, the samples were placed into a stacked sieve system that contained mesh sizes #8, #12, #20, #35, #80, #200, and a pan, and gently flushed with water to produce granular samples at specific size intervals (Figure 3-5).

These sieve mesh sizes separated the crushed sample into sizes GRI+, A, GRI, B, C, and powder (Table 3-2), where GRI sizes were used for N_2 gas physisorption, powder sizes for XRD, TOC, and pyrolysis, and all particle sizes for pycnometry experiments. Samples were weighed and placed into appropriately-sized glass vials based on mass. Table 3-3 displays which experiments are performed on each sample in order to maximize use of all samples.

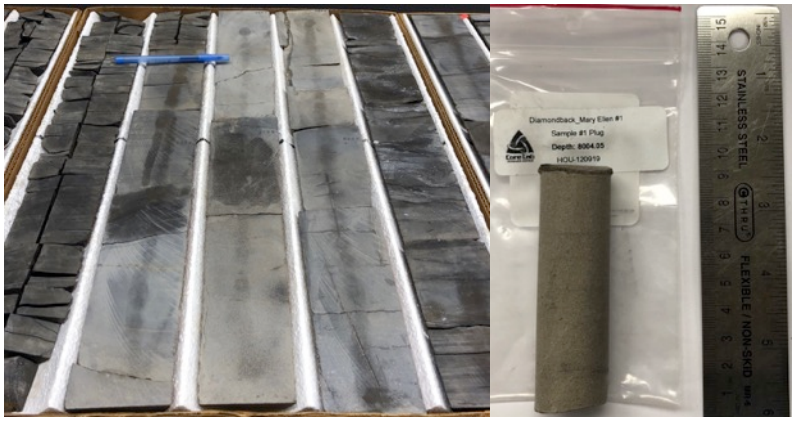

Figure 3-1: ME-8004 sample photo showing core slab interval on left with blue pen for scale as well as pointing to the approximate plug point and core plug photo upon arrival to UTA lab on right. All core slab and plug photos are located in Appendix D.

Figure 3-2: Hi-Tech Diamond saw used to cut samples.

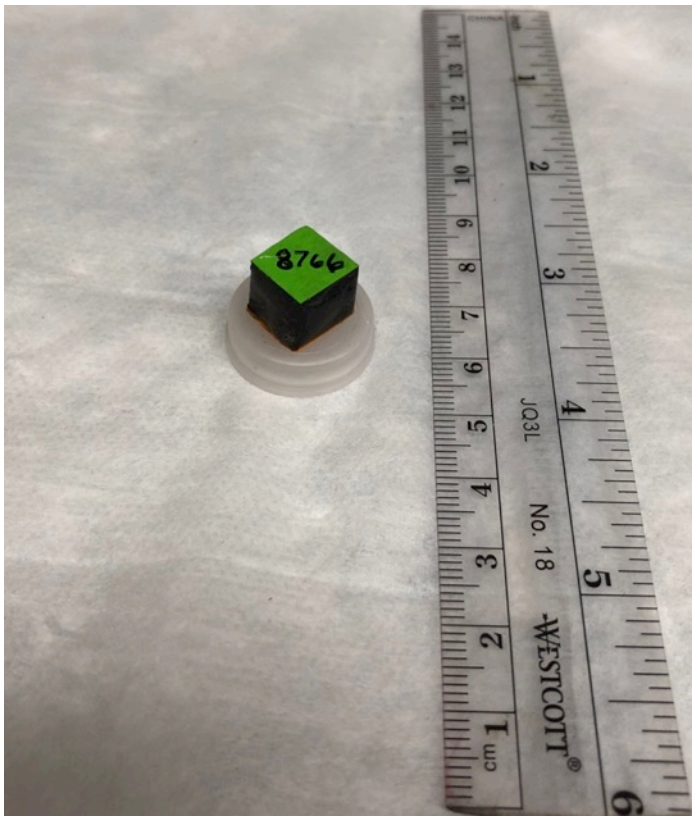

Figure 3-3: Image of cut and epoxied cube (for the imbibition test) with green tape on top and bottom to keep epoxy off of testing edges.

Table 3-2: Sample size designation.

Size designation	Mesh size	Linear size	Equivalent spherical diameter (µm)
Plug		2.54 cm in diameter and ~ 3 cm in height	30735
Cube		1.0 cm	9086
GRI+	#8 to #12	1.70 - 2.36 mm	2030
Size A	#12 to #20	841 – 1700 µm	1271
GRI	#20 to #35	500 – 841 µm	671
Size B	#35 to #80	177 – 500 µm	339
Size C	#80 to #200	75 – 177 µm	126
Powder	<#200	<75 µm	<75

Figure 3-4: Mortar and pestle used to crush samples (left). Electric grinder used to crush samples (right).

Figure 3-5: Sieve stack used to separate sample into discrete granular sizes.

Table 3-3: List of experiments performed on each sample for this study.

Sample ID	FIP & Fluid Displacement	Liquid Pycnometry	Fluid Imbibition	XRD	TOC	Pyrolysis	MIP	Contact Angle
ME-8004	X							
ME-8027	X	X	X	X			X	X
ME-8045	X							
ME-8063	X							
ME-8435	X							
ME-8444	X							
ME-8455	X							
ME-8463	X							
ME-8621	X	X	X	X	X	X	X	X
ME-8633	X	X	X	X	X	X	X	X
ME-8832	X							
ME-8852	X							
ME-8866	X	X	X	X	X	X	X	X
ME-9031	X	X	X	X	X	X	X	X
ME-9039	X							
ME-9044	X							
ME-9052	X	X	X	X	X	X	X	X
ME-9207	X	X	X	X	X	X		X
ME-9197	X	X	X	X	X	X	X	X
ME-9509	X							
ME-9511	X							
ME-9528	X							
ST-8441	X							
ST-8877	X	X	X	X			X	X
ST-9400	X							
ST-9605	X							
ST-9612	X	X	X	X	X	X	X	X
ST-9632	X	X	X	X	X	X	X	X
ST-9833	X							
ST-9841	X	X	X	X	X	X	X	X
ST-9849	X	X	X	X	X	X	X	X
ST-10053	X							
ST-10067	X							
ST-10310	X							
ST-10318	X							
ST-10322	X							
JB-9187	X	X	X	X			X	
JB-9209	X							
JB-9733	X	X	X	X	X	X	X	X
JB-9781	X	X	X	X	X	X	X	X
JB-9849	X							
JB-9867	X							
JB-9871	X	X	X	X	X	X	X	X
JB-9891	X	X	X	X	X	X	X	X
JB-9904	X							
JB-10525	X							
JB-10570	X							
JB-10595	X							

3-3 Vacuum-Assisted Fluid Immersion Porosimetry (FIP) and Fluid Displacement

3-3-1 Introduction to FIP and Fluid Displacement

Fluid immersion porosimetry with assistance of vacuum pulling followed with Archimedes' displacement method, is used to investigate pore structure of a porous medium. With tracers, this method can be utilized to quantify the edge-only accessible porosity distribution of poorly connected and/or low porosity rocks (Hu et al., 2015). The vacuum-assisted FIP apparatus consists of a steel sample chamber connected to a vacuum pump, compressed gas (CO_2) cylinder, and fluid reservoir (Figures 3-6 and 3-7). This customized apparatus can quantify the effective porosity of each sample by evacuating the sample chamber, then filling the sample chamber with fluid to immerse the sample and occupy the evacuated pore space. By reducing the pressure in the sample chamber to 0.05 Torr, which is equivalent to 99.993% vacuum (Kibria et al., 2018), the air in the sample chamber, in addition to edge-accessible pores of the sample placed inside the chamber, is evacuated. These evacuated pores will become accessible for fluid occupation as a result. During fluid immersion, the samples were introduced to pressurized CO_2, further assisting the fluid into the pores of the sample. CO_2 is easier to dissolve in DI water than air, allowing for better saturation and porosity measurements. After FIP, the saturated samples underwent liquid displacement using the Archimedes principle to determine the bulk density for rock cores, large and irregularly-shaped rocks, and gravels (Dane et al., 2002). Combined with Archimedes' principle, the FIP approach can measure porosity, bulk density and grain density of rock samples (American Petroleum Institute, 1998). The vacuum FIP apparatus used in this study was custom designed by Dr. Hu's research group. The data collected from vacuum FIP and liquid displacement are utilized in Eqs. 3-1 to 3-3 to calculate porosity, bulk density, and grain density.

$$\varphi = V_o/V_b = (W_s - W_d)/W_f \quad \text{Eq. 3-1}$$

$$\rho_b = V_o/W_d = (W_s - W_d)/\rho_f \quad \text{Eq. 3-2}$$

$$\rho_g = \rho_b/(1-\varphi) \quad \text{Eq. 3-3}$$

Where,

φ: Porosity (%)

V_o: void volume (cm^3)

V_b: Bulk volume (cm^3)

W_s: Saturated weight of the sample (g)

W_d: Sample oven-dry weight (g)

W_f: Sample weight submerged in fluid (g)

ρ_f: Fluid density (g/cm^3)

ρ_b: Bulk density (g/cm^3)

ρ_g: Grain density (g/cm^3)

3-3-2 Procedure for FIP and Fluid Displacement

The apparatus for vacuum-assisted FIP, as described above, consists of a sample chamber connected to a fluid reservoir, compressed CO_2 gas cylinder, and vacuum pump (Figures 3-6 and 3-7). Sample types for FIP included core plugs and 1 cm^3 cubes to determine variations in properties based on sample size. Prior to the experiments, samples were placed inside a 60°C oven for at least 48 hours to remove moisture in pore space connected to the sample edge and then placed in the desiccator for at least 30 minutes. Before being placed in the sample chamber, the weight of each sample was recorded. After sealing the chamber and shutting the fluid reservoir value, the vacuum pump was turned on to begin the experiment. The first evacuation was complete when the pressure in the chamber was less than 0.1 Torr (the timeframe for this is

a minimum of 8 hours and can be sustained for 12 to 18 hours if needed). After the first evacuation, CO_2 was released into the chamber until the gauge read 50 psi; and remained under pressure for 30 minutes. Afterward, another evacuation cycle was conducted to 0.1 Torr. Once the samples had been sufficiently evacuated, the sample chamber was filled with a saturating fluid. Plugs were saturated in de-aired (from boiling and cooling) DI water (de-ionized water) only and cubes were saturated in DI water, THF (tetrahydrofuran), and DT2 (2:1 ratio in volume of n-decane and toluene) used as a substitution for oil to determine the wettability of the sample surface to oil. Next, another cycle of CO_2 was injected to 50 psi, pressurizing the fluid so that it could further invade into the edge accessible pore system of the sample.

After the completion of FIP, the now saturated samples underwent liquid displacement tests. The saturated samples were removed from the chamber, excess fluid cleaned, and weighed in air. Next, the Archimedes Principle process was started. The Archimedes Principle apparatus consists of an empty sample basket (an aluminum can with holes) that is suspended within a beaker of the saturating fluid (Dane et al., 2002) (Figure 3-8). The beaker of fluid was placed on a top loading balance. The balance was zeroed with the empty basket submerged in the beaker of fluid. The empty sample basket only touches the fluid within the beaker, not the wall or bottom of the beaker. Next, the saturated sample was placed inside the wire basket submerged in the beaker of fluid. The weight that is displaced and shown on the balance was recorded. The whole fluid displacement procedure was then repeated by putting the saturated sample back to the sample chamber. Finally, we used the equations (Eq. 1, Eq. 2, and Eq. 3) to determine the porosity, bulk density, and grain density.

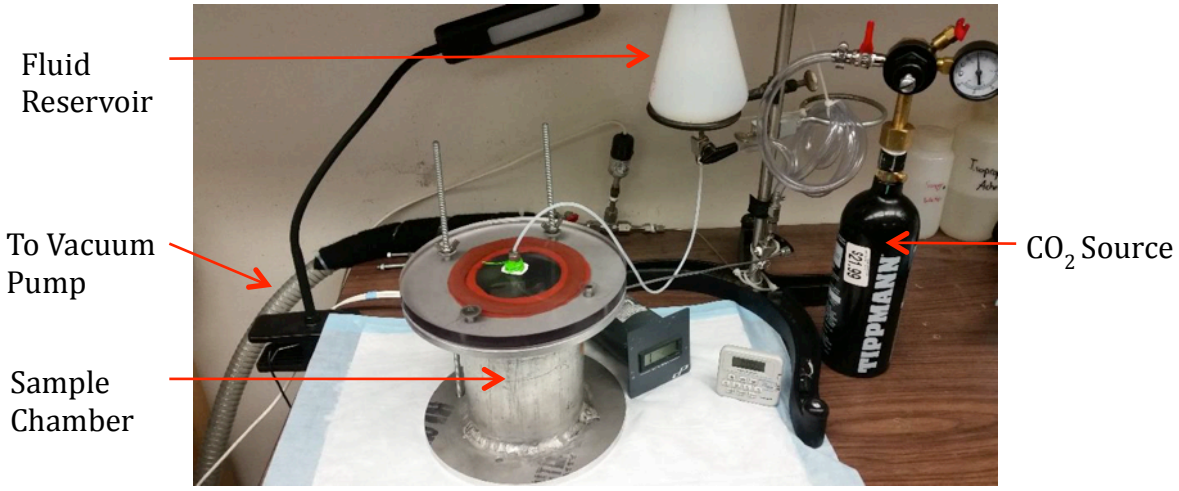

Figure 3-6: Vacuum-assisted FIP experiment set up.

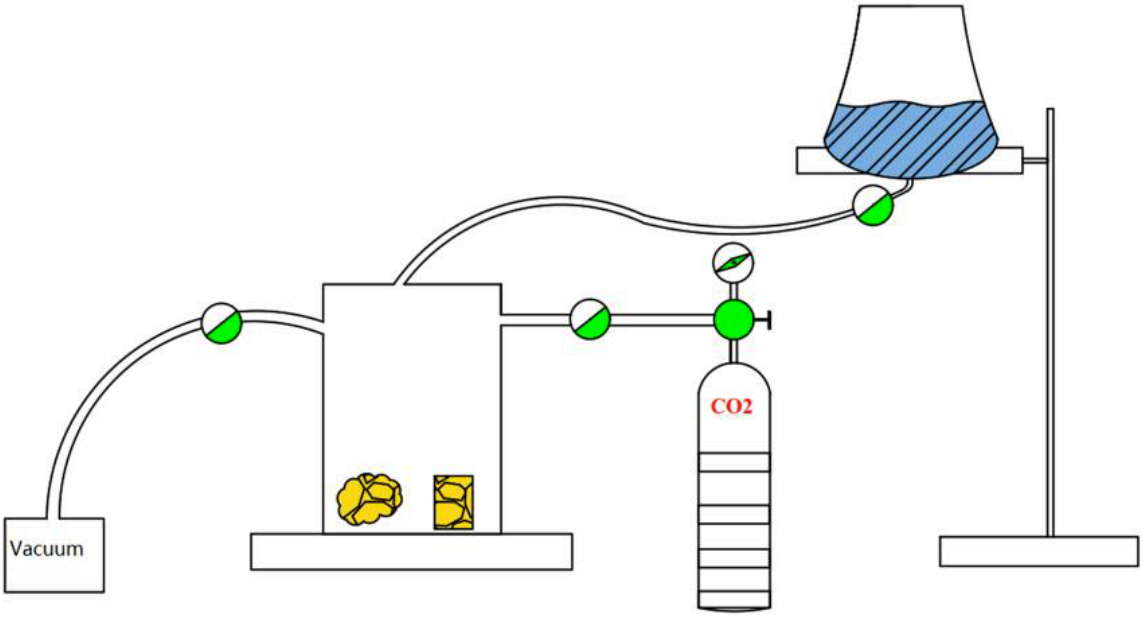

Figure 3-7: Vacuum-assisted FIP schematic (Wang, 2019).

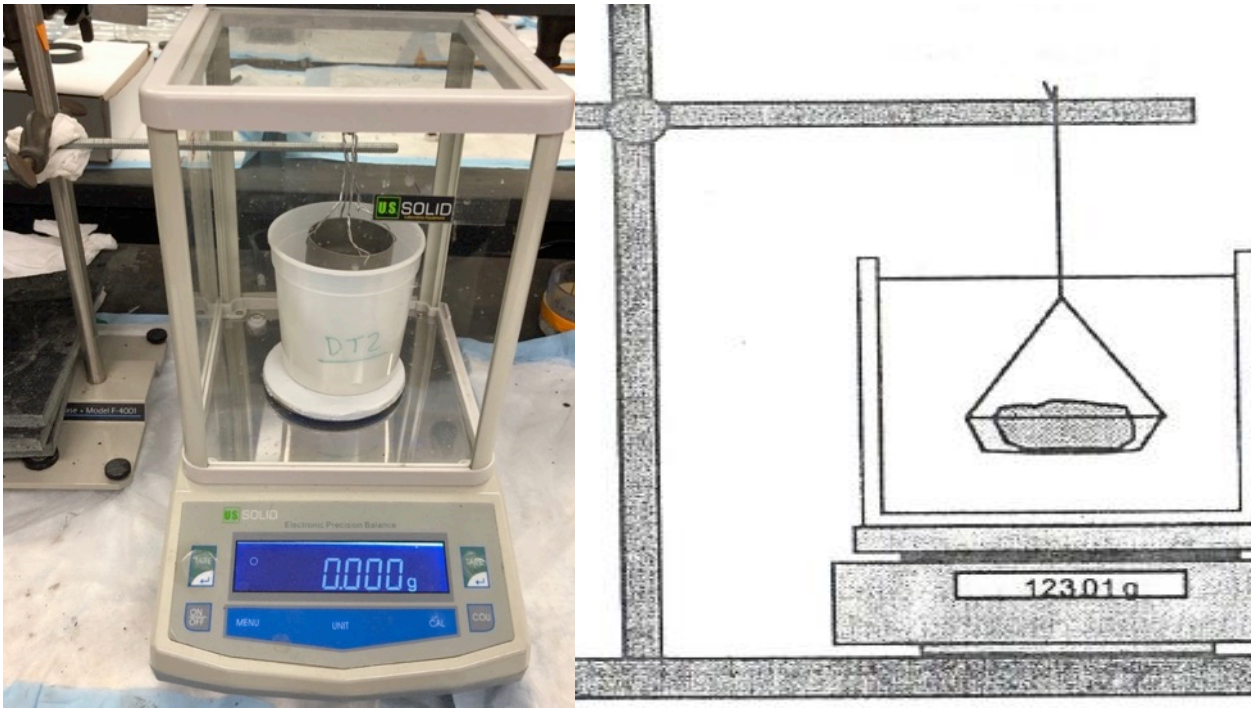

Figure 3-8: Photo of Archimedes' apparatus with the plastics bucket and holed aluminum can used for fluid displacement of large samples (left). Archimedes' principle schematic (Dane et al., 2002).

3-4 X-Ray Diffraction (XRD)

X-Ray Diffraction (XRD), or X-Ray crystallography, is a standardized measurement used to qualitatively and quantitatively investigate and identify the mineral composition and clay content of a rock sample. XRD was performed on select samples from all three wells for a total of 18 samples (Table 3-3). About 1.5 grams of size <75 μm powder for each sample was sent for analysis. The XRD testing was completed at Shimadzu Center for Environmental, Forensics and Material Science (CEFMS) laboratory located at University of Texas at Arlington (UT Arlington), using the MaximaX XRD-7000 X-Ray Diffractometer (Figure 3-9). The powder sample is placed into a steel sample tray, located on the diffractometer axis, and leveled (Figure 3-9). Both the X-ray tube and detector with Soller slit filters are attached to separate arms. These two arms rotate around the sample from 2° to 70° (Figure 3-9). During the rotation, X-rays are

directed at the sample and are diffracted by the mineral crystal edges in the sample (Figure 3-9). The detector records the angles and intensity of the diffracted X-rays and plots them against each other. This plot is known as the diffraction pattern. Through spectrum analysis and whole-pattern fitting using the Minerals relational database, the mineral compositions and weight percentages for the sample are obtained. Detailed methods and procedures for XRD testing using the MaximaX XRD-7000 are attached in Appendix A. The bulk percentages calculated from the data generated in these tests is also used to estimate the lithology of the sample by plotting on the sCore Lithofacies ternary diagram from Schlumberger (2014).

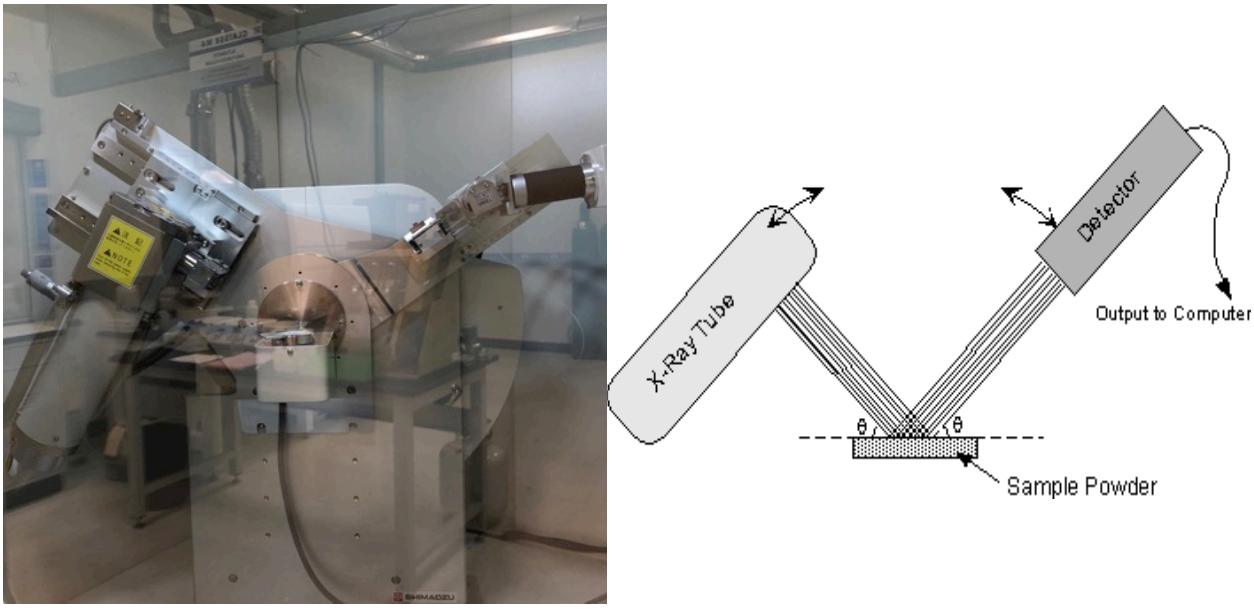

Figure 3-9: Photo of Shimadzu Maxima X XRD-7000 analyzer (left) and XRD schematic (right) (Nelson, 2018)

3-5 LECO Total Organic Carbon (TOC)

Organic richness of rock samples is determined in this study by utilizing the LECO method. TOC was measured by GeoMark Research laboratory using the LECO C230 instrument. The TOC analysis was performed on select samples from all three wells for a total of 15 samples (Table 3-3). Approximately a teaspoon of size <75 μm powder for each sample was sent to

GeoMark for analysis. To avoid inorganic carbon input, each sample is first treated with HCl and weighed before and after thus giving a percent carbonate value. Then, using high temperature combustion (1200 °C) in an oxygen-rich reaction tube, the remaining carbon in the sample will convert to carbon dioxide. This carbon dioxide is detected and measured by an IR (infra-red) sensor, outputting a TOC weight percentage. Detailed methods and procedures for TOC testing using the LECO C230 are attached in Appendix B. The TOC percentages determined from this experiment combined with the results from pyrolysis can be used in a number of equations to determine several geochemical parameters for a sample (Table 3-4).

3-6 Pyrolysis

Pyrolysis is a standardized measurement for geochemical analyses to determine the source rock potential of a sample. The pyrolysis testing was completed at GeoMark Research laboratory using the HAWK Pyrolysis instrument (Figure 3-10). Pyrolysis testing was performed on select samples from all three wells for a total of 15 samples (Table 3-3). Approximately a teaspoon of size <75 μm powder for each sample sent to the laboratory for analyses. Each sample was progressively heated to 600ºC in an inert environment. As the sample begins to increase in temperature, the hydrocarbons currently present in the rock (either free or adsorbed) are volatilized. Then, as the temperature continues to increase, the kerogen present in the sample begins conversion to hydrocarbons and hydrocarbon-like compounds. Also, oxygen-containing volatiles such as carbon dioxide are released. Detailed methods and procedures for pyrolysis tests using the HAWK instrument are attached in Appendix C. From the measured values recorded from pyrolysis testing combined with the TOC values for each sample, there are several useful ratios and calculated values used to determine kerogen type, quality, source potential, and

maturity. These measured values, calculated values, ratios, and descriptions are outlined in Table 3-4.

Table 3-4: Pyrolysis parameters and equations.

Pyrolysis Measured Values	
Value	**Description**
S1	Free oil content (mg HC/g rock)
S2	Remaining generation potential (mg HC/g rock)
S3	Organic carbon dioxide yield (mg CO_2/ g rock)
T_{max}	Temperature at maximum evolution of S2 hydrocarbons (^oC)
Pyrolysis Ratios and Calculated Values	
Value	**Equation**
Hydrogen Index (HI)	S2/TOC × 100 (mg HC/g TOC)
Oxygen Index (OI)	S3/TOC × 100 (mg CO_2/g TOC)
Production Index (PI)	S1/ (S1+S2)
Normalized Oil Content	S1/TOC × 100 (mg HC/g TOC)
S4	10 × TOC –(0.83 (S1+S2)) (mg C/g rock)
Residual Carbon (RC)	S4/10 (%)
Vitrinite Reflectance (Ro)	0.0165 × T_{max} – 6.51 (%) (Jarvie, 2018)

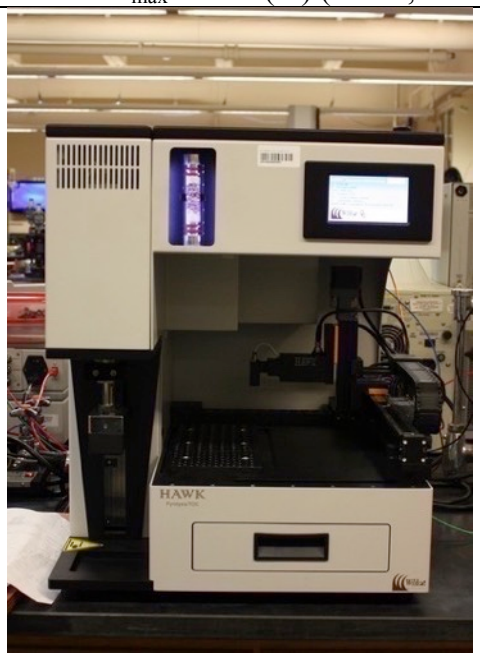

Figure 3-10: Photo of HAWK pyrolysis instrument.

3-7 Liquid Pycnometry

3-7-1 Introduction to Liquid Pycnometry

Liquid pycnometry is used to determine bulk density of small sample size fractions that cannot be tested using FIP, which involves handling of individual monoliths. Although originally designed to measure grain density in solid samples, this method can also test "relative bulk density" of a porous sample towards a fluid, whether wetting or non-wetting, for a wide range of sample sizes. A porous sample will displace less volume, as a portion of fluid will be imbibed into the pore space of a sample, with magnitude depending on fluid wettability and edge-accessible porosity related to sample size. Identifying this change in "relative bulk density" among different fluids and sample sizes is one of the main purposes of liquid pycnometry.

Pycnometry was performed on select samples from all three wells for a total of 18 samples each with 5 different size fractions. Pycnometry testing was conducted at UT Arlington using a high-precision weighing balance and 10 ml and 5 ml pycnometers (Figure 3-11). Bulk density, which has a direct relationship with porosity, can be determined by carefully measuring mass and volume using the pycnometry test and Eq. 3-4.

$$\rho_b = W1/(W3-W2+W1)/\rho_f \qquad \text{Eq. 3-4}$$

Where:

ρ_b: Apparent bulk density (g/cm3)

W1: Weight of the oven dry sample (g)

W2: Weight of the pycnometer + oven dry sample + fluid (g)

W3: Weight of the pycnometer + fluid (g)

ρ_f: Density of fluid (g/cm^3)

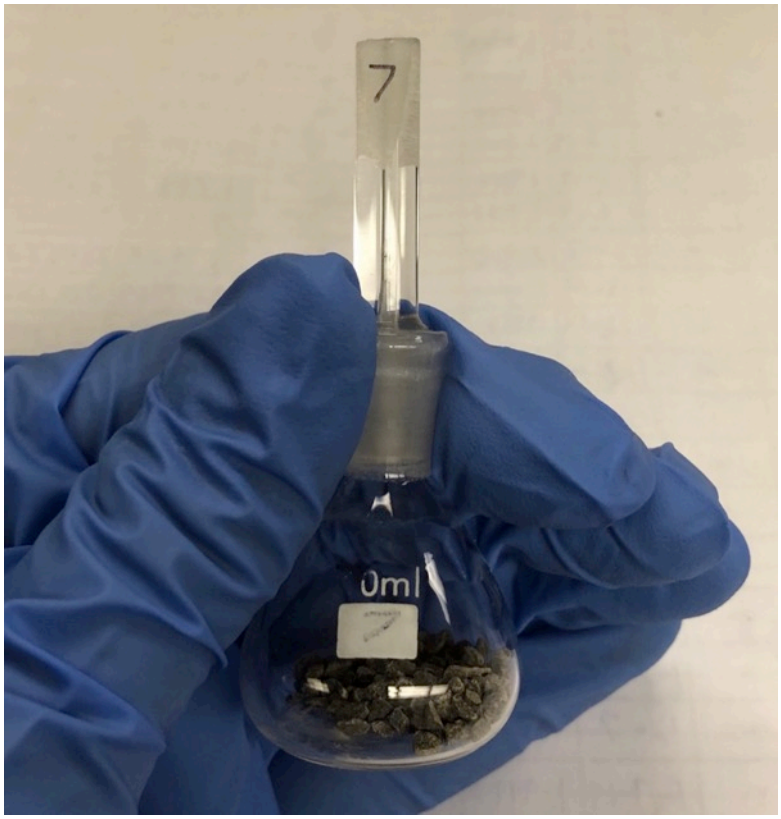

Figure 3-11: Photo of 10 ml pycnometer filled with 2g of dry GRI sample with stopper, but no fluid.

3-7-2 Procedure for Liquid Pycnometry

Five different size fractions, GRI+, A, GRI, B, and C for each sample were used for pycnometry testing (Table 3-3). Samples and pycnometers were first dried in a 60^{o}C oven for a minimum of 48 hours to remove moisture. After drying, approximately 1 or 2 grams of each size was weighed depending on sample mass availability. Then, empty pycnometer and stopper weights were recorded, then again with the sample added. At this point, the desired saturating fluid was added to the pycnometer with a dropper until the pycnometer was filled, then the stopper was inserted to force the excess fluid out of the capillary. A dry cloth was used to wipe away excess fluid on the outside of the pycnometer and the weight was measured. The pycnomter was emptied, cleaned, and dried, before being filled again with only the same

saturating fluid. After the stopper was inserted and outside dried, the fluid filled pycnometer was weighed. At this point all of the weights had been recorded and the equations could be used to calculate for bulk density and compare results by sample size fraction. This process was repeated two to three times (depending on sample availability) for each testing fluid, DI water, DT2, and THF. Finally, average and standard deviation of the repeated results are calculated and plotted for all sizes of each sample.

3-8 Spontaneous Fluid Imbibition

3-8-1 Introduction to Spontaneous Fluid Imbibition

Imbibition tests are used to investigate pore connectivity and wettability by measuring the amount of fluid uptake into a porous rock sample over time. The rate of imbibition is primarily dependent on properties of porous media and fluids, as well as their interactions. These interactions include matrix permeability, relative permeability, boundary conditions, fluid viscosity, interfacial tension and wettability (Zhang et al., 1996). Since the amount of fluid a rock sample imbibes is strongly related to the sample's wettability, different wettability analysis conditions are created (Gao & Hu, 2016a, 2016b; Yang et al., 2017). DI water is used as a hydrophilic fluid, and DT2 is used as a hydrophobic fluid. The results of each imbibition test will provide a better understanding of pore connectivity, wettability, and interactions of different fluids on each sample.

Spontaneous imbibition is the process of fluid penetrating a porous media due to capillary forces and/or gravity (Lopez and Soria, 2007). Spontaneous imbibition of a wetting liquid into porous media is regarded as a crucially important driving mechanism for enhancing oil recovery from naturally fractured reservoir rock, especially rocks with a low permeability (Cai et al., 2012). In this study, spontaneous imbibition was performed on select samples from all three

wells for a total of 18 epoxied 1 cm^3 (cube) size samples using DI water and DT2 as imbibing fluids (Table 3-3). The imbibition testing was conducted at UT Arlington using a RADWAG AS 60/220.R2 high-precision weighing balance (with bottom weighing ability), a sample chamber, and a computer running the balance's auto-recording software for recording weight change over time (Figures 3-12 and 3-13).

To determine several useful parameters related to pore connectivity from spontaneous imbibition, a series of equations related to cumulative imbibition are needed. For a well-connected porous sample towards a wetting fluid, cumulative imbibition is expressed over time as in Eq. 3-5.

$$I=St^{0.5} \quad \text{Eq. 3-5}$$

where,

I: Cumulative imbibition (mm)

S: Sorptivity ($mm/s^{0.5}$)

t: Imbibition time (s)

Presented as a variable in Eq. 3-5, sorptivity, is another useful parameter to quantify imbibition behavior. Sorptivity is jointly controlled by capillary pressure and permeability (Philip, 1957; Kao and Hunt, 1996). When gravitational force is negligible, cumulative imbibition is related to the square-root-of-time (Philip, 1957; Kao and Hunt, 1996; Hu et al., 2001; Tokunaga and Wan, 2001). Furthermore, the effective wetted distance (L_d) equals cumulative imbibition (I) divided by the step change in volumetric fluid content ($\Delta\theta$), which is often less than or equal to the porosity of porous media (Eq. 3-6):

$$L_d=I/\Delta\theta \quad \text{Eq. 3-6}$$

Combining the cumulative imbibition equation (3-5) and effective wetted distance equation (3-

6), the effective wetting front distance can be expressed as Eq. 3-7 (Tokonaga and Wan, 2001):

$$L_d = \frac{S}{\Delta\theta}\sqrt{t} \quad \text{Eq. 3-7}$$

When a porous medium has a contact angle of zero, indicating perfect wettability towards a fluid, a ¼ power relationship exists between permeability and effective wetted distance (Kao and Hunt, 1996; Tokunaga and Wan, 2001). So, assuming a well-connected porous medium and an imbibition behavior in one dimension, Eq. 3-8 can be used:

$$L_d = B\sqrt{\frac{\sigma}{\mu}}k_{imb}{}^{1/4}\sqrt{t} \quad \text{Eq. 3-8}$$

Where,

B: Geometry of porous medium

σ: Liquid-gas surface tension (mN/m)

μ: Fluid viscosity (mPa·s)

k_{imb}: Permeability of porous media from an imbibition test (m^2)

t: Time (s)

Combining Equations 3-7 and 3-8 results in a relationship between fourth-power of sorptivity and permeability (k_{imb}) that can be obtained from imbibition tests. This relationship is expressed in Eq. 3-9 (Kao and Hunt, 1996; Tokonaga and Wan, 2001):

$$k_{imb} \sim \left(\frac{\mu}{\sigma}\right)^2\left(\frac{S}{B\Delta\theta}\right)^4 \quad \text{Eq. 3-9}$$

However, mudrocks have a mixed wettability and sparsely connected pore space, so we do not presume the square root of time relationship. Instead, pore connectivity is assessed using the slope of log imbibed liquid mass on the y-axis versus log time on the x-axis (Hu et al., 2012; Chukwama, 2015). The slopes derived from spontaneous imbibition tests give valuable insight into pore space connectivity. Higher slopes, upwards of ½, are generally recorded at the

beginning of tests (Stage I), as edge accessible porosity is a factor when a sample first comes in contact with fluid. The slope could decrease as the test continues (Stage II) due to the fluid only moving through interior connected pore space. When the fluid reaches the top of the sample (Stage III) the slope will become almost horizontal. However, slopes vary sample to sample based on the pore connectivity and wettability, where in Stage II a slope near ½ indicates a well-connected pore system and a slope closer to ¼ indicates a poorly connected pore system (Hu et al., 2015).

3-8-2 Procedure for Spontaneous Fluid Imbibition

An epoxied sample was sanded down on its two open faces using 220-grit sandpaper to flatten to a uniform level and ensure no epoxy or other contaminants were blocking accessibility. The sample was dried in a 60°C oven for 48 hours. Once dry, the sample was weighed before being placed in a holder of known weight and being weighed again. A petri dish of desired fluid was prepared, weighed, and placed into the sample chamber (along with two open jars of the same desired fluid, for DI water runs) to keep humidity level high (~98%) and constant. The sample holder was hung within the sample chamber from the balance's suspension-weight hook. The petri dish was raised within the sample chamber using a jack until the fluid is touching the bottom open face of the epoxied cube. Simultaneously, recording was started so weight change was measured over time. After 24 hours for a test using DI water or 12 hours for test using DT2, the recording was stopped and the sample chamber lowered away from the suspended sample. The sample and holder are weighed together and separated after the sample was wiped to remove excess fluid on the sample edge. The petri dish of remaining fluid and wipe are both weighed post experiment. Fluid unaccounted for in weight changes pre to post experiment was treated as evaporative loss and an estimated evaporative loss was achieved through blank experiment

without a sample (Hu, et al., 2001). Lastly, weight changes can be plotted against time and used in equations mentioned above to investigate the pore connectivity, wettability, and interactions of various fluids on each sample.

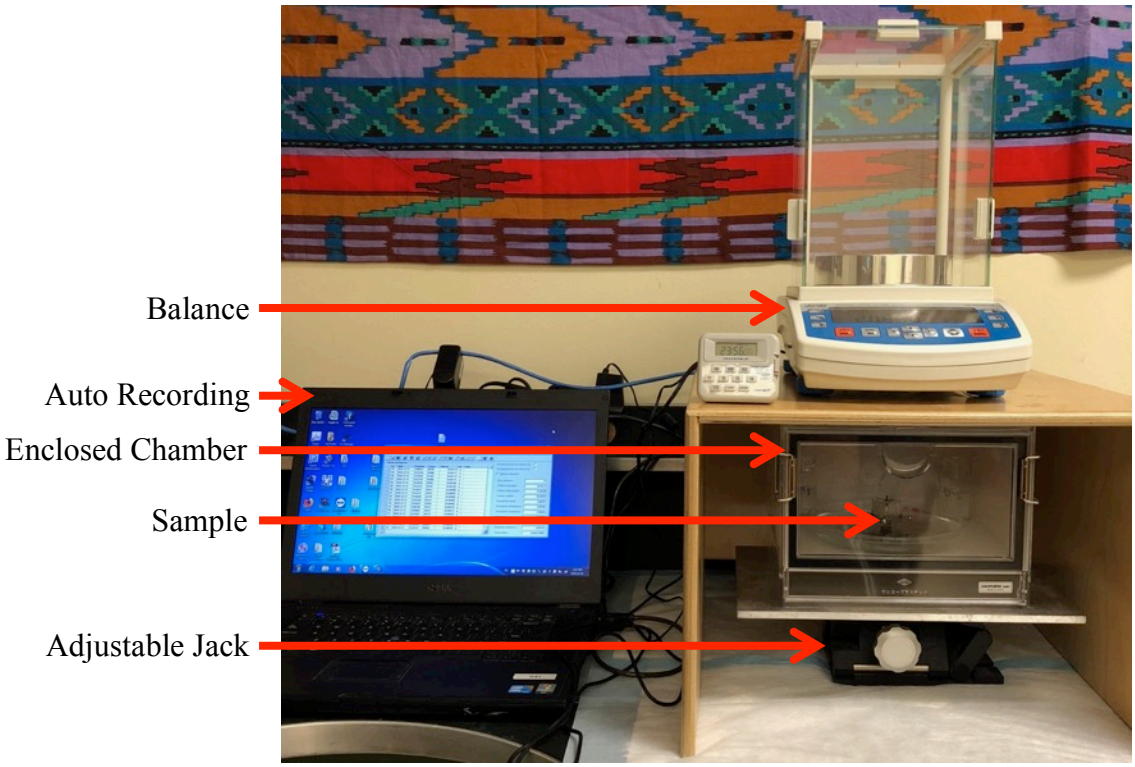

Figure 3-12: Spontaneous fluid imbibition set up.

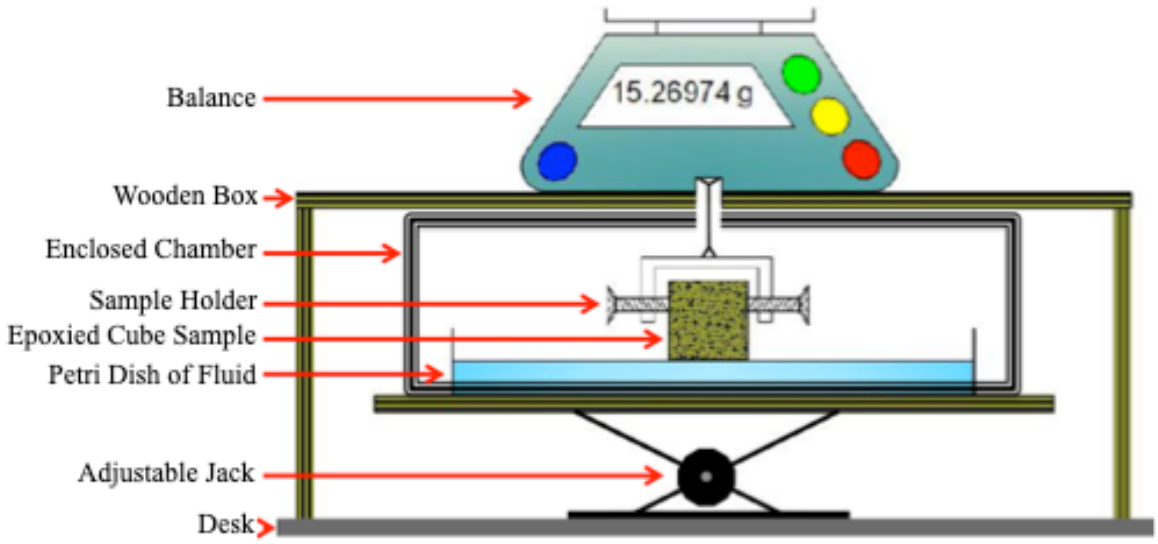

Figure 3-13: Spontaneous fluid imbibition schematic (modified from Wang, 2019).

3-9 Mercury Intrusion Porosimetry (MIP)

3-9-1 Introduction to MIP

MIP, also known as MICP (mercury intrusion capillary pressure), is a standardized measurement used to directly analyze pore structure parameters of porosity, particle density, bulk density, pore throat size distribution, and mean/median pore throat diameters (Hu and Ewing, 2014). This method can also indirectly determine broader pore characteristics, such as total pore surface area, permeability, and tortuosity (Micromeritics, 2001; Hu and Ewing, 2014). The MIP testing was completed using the Micrometrics Autopore IV 9510 (Figure 3-14), performed on select samples from all three wells for a total of 17 samples (Table 3-3). A $1cm^3$ cube sized sample for each depth was tested. Mercury, a non-wetting fluid to most porous media, will not invade pores unless an external pressure is applied. In order to invade the pore throat, a large enough force must be applied to exceed the capillary pressure. The MIP apparatus forces the non-wetting mercury into pore throats at incremental pressures from 0.2 psi to 60,000 psi (414 MPa). The diameter of pore-throats invaded by mercury is inversely proportional to the applied pressure; the higher the applied pressure, the smaller are the pores invaded by mercury (Hu and

Ewing, 2014). Based on the pressure range of the MIP apparatus, detectable pore-throat diameters ranged from 1,110,000 nm to 2.8 nm. The Washburn equation describes the relationship between pressure and radius of the capillary pore, assuming that all pores are cylindrical (Washburn, 1921) (Eq. 3-10).

$$\Delta P = -\frac{2\gamma cos\theta}{r} \quad \text{Eq. 3-10}$$

Where,

ΔP: External pressure (psia)

γ: Surface tension for mercury (dynes/cm)

θ: Contact angle between porous media and mercury (degrees)

r: Pore throat radius (μm)

The original Washburn equation (Eq. 3-10) in 1921 assumes a constant contact angle and surface tension. However, pore throat diameters < 10 nm the contact angle increases significantly as pore diameter decreases thereby exposing a limitation of the original equation. This limitation can result in an error as high as 44% in small pore size distributions (Wang et al., 2016). The Washburn equation has been revised and modified to account for variations in contact angle and surface tension by Wang et al. (2016) (Eq. 3-11).

$$\Delta P = -\left(\frac{2\gamma Hg(r) cos\theta Hg(r)}{r}\right) \quad \text{Eq. 3-11}$$

where,

γHg and θHg are functions of r instead of being constant

By using the modified Washburn equation (Eq. 3-11) and measuring the quantity of mercury that intrudes at each pressure step, a pore-size distribution can be made and porosity can be parametered. A limitation of the modified Washburn equation (Eq. 3-11) is its assumption of all

shale pores being cylindrical, an unrealistic assumption for geological samples but provides close approximation of pore throats. (Hu et al, 2015).

Permeability can be indirectly estimated from MIP results by determining pore throats at which hydraulic conductance is at maximum (Katz and Thompson, 1987; Gao and Hu, 2013) (Eq. 3-12). This point is determined by locating an inflection in the cumulative intrusion of mercury into the sample by pressure. Each pore diameter has a specific capillary pressure that must be exceeded before mercury is intruded. Each inflection point represents an intruded pore-throat diameter corresponding to a threshold pressure for a connected pore network. These inflection points can be used to determine permeability (Katz and Thompson, 1986;1987) (Eq. 3-12).

$$k = (\frac{1}{89})(\frac{(L_{max})^3}{L_c})\emptyset S_{(L_{max})} \quad \text{Eq. 3-12}$$

Where:

k: Permeability (μm^2)

L_{max}: Pore-throat diameter when hydraulic conductance is at a maximum (μm)

L_c: Pore throat diameter corresponding to the threshold pressure (μm)

ϕ: Porosity (fractional)

$S_{(Lmax)}$: Mercury saturation at L_{max} (fractional)

Another important characteristic that affects pore connectivity and aids in understanding of fluid migration through pore matrices is tortuosity, which can be empirically derived using direct measurements from MIP (Hager, 1998; Webb, 2001; Hu et al., 2015) (Eq. 3-13).

$$\tau = \sqrt{\frac{p}{24k(1+pV_{tot})} \int_{n=r_c,min}^{n=r_c,max} n^2 f_y(r_c) dr_c} \quad \text{Eq. 3-13}$$

Where,

τ: Tortuosity

p: Density of mercury(g/cm^3)

V_{tot}: Total pore volume (ml/g)

r_c: Capillary radius (µm)

$f_y(r_c)dr_c$: Volume probability density function (volume of pores with a radius in the range of rc to rc + drc per kg of dry material) (cm^3/g)

r_c, min: Minimum detectable capillary radius by MIP (µm)

r_c, max: Maximum detectable capillary radius by MIP (µm)

$\int_{n=r_c,min}^{n=r_c,max} n^2 f_y(r_c) dr_c$: Pore-throat volume distribution by pore-throat size

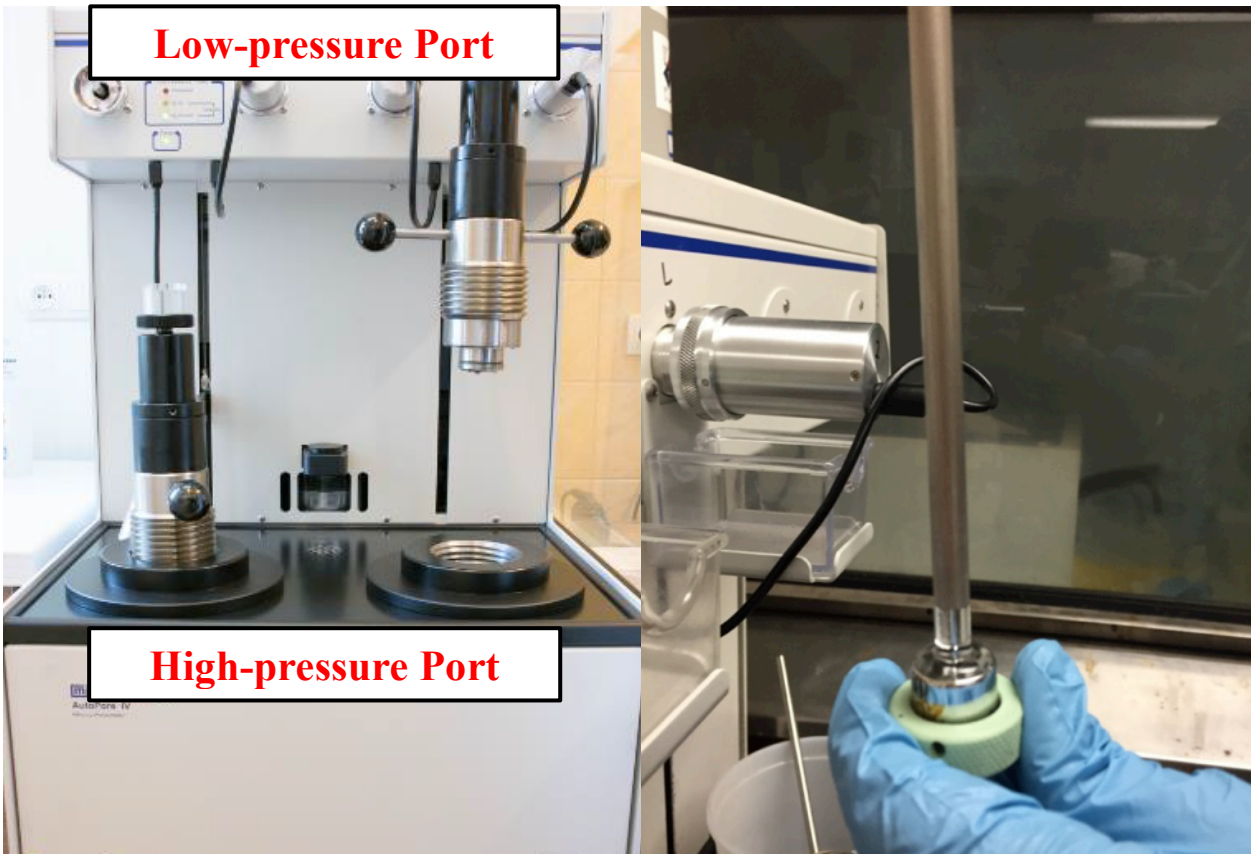

Figure 3-14: Photo of the Micrometrics AutoPore 9520 used for MIP (left) and a penetrometer (right) (modified from Mann, 2017).

3-9-2 Procedure for MIP

In order to remove any moisture before testing, the 1cm^3 sample was placed in a 60°C oven for at least 48 hours. The dry sample weight was taken and an appropriate penetrometer was picked based on the sample's reported porosity from FIP. The penetrometer is the sample chamber connected to a metal clad, precision bore, and glass capillary system used to inject mercury into the sample (Figure 3-14). The size of the bore in the penetrometer was picked based on the samples porosity and dictates the starting (filling) pressure for mercury to fill the sample chamber via the stem of a penetrometer. A large bore size has a lower starting pressure of 0.2 psi and was used for samples > 2% porosity. A smaller bore size has a higher starting pressure of 5.0 psi and was used for samples < 2% porosity. The appropriate penetrometer was weighed before being assembled with the sample in the chamber and weighed again. The penetrometer assembly was covered in vacuum grease and inserted into the low-pressure port on the MIP instrument and evacuated to 0.05 torr (.000972 psi, 6.7 pa, or 99.993% vacuum), which aids in clearing the sample pore network of air and moisture. Low-pressure intrusion was started by filling the penetrometer with mercury and applying pressure up to 30 psi (Figure 3-15). As pressure increased, mercury invaded the sample and the mercury level in the penetrometer bore decreased (Figure 3-15). When low-pressure analysis was complete, the outside surface of the penetrometer was wiped clean and apparatus weighed. The penetrometer was placed into the high-pressure port on the MIP instrument and pressure reapplied up to 60,000 psi. As pressure increased, mercury intrusion was recorded at a detection limit of <0.1 μL (Quintero, 2016). After completion of high-pressure analysis, mercury extrusion was recorded as pressure dropped. Values acquired in this process were used to determine the sample characteristics mentioned previously. During analyses, when a specified pressure point was reached, the system held

pressure for a designated 30-second and 60-sec equilibrium time for low- and high-pressure analyses, to stabilize the mercury volume reading before proceeding to the next pressure point.

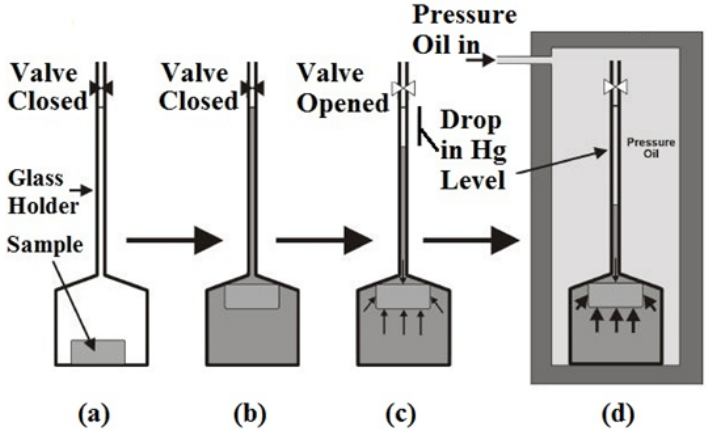

Figure 3-15: MIP schematic (Kantzas, 2019).

3-10 Contact Angle

Wettability quantifies the preferential tendency of a fluid to wet a rock surface in the presence of another fluid (Agbalaka et al., 2008). A porous medium's organic composition and mineralogy alter its wettability state and can vary depending on pore size distribution. Quantifying wetting preferences of a formation is critical in selecting completion fluids and optimizing recovery rates in low permeability formations (Ma, 1994). Contact angle tests are used to investigate a rock sample's wettability. Contact angle testing was completed using the SL200KB Optical Dynamic/ Static Interfacial Tensiometer & Contact Angle Meter (Figure 3-16). Contact angle testing was performed on select samples from all three wells for a total of 18 samples (Table 3-3). Several 2 mm×10 mm×10 mm thin slabs for each sample were tested. DI water, API (American Petroleum Institute) brine, DT2, 20% THF or 20% isopropyl alcohol (IPA) were used to determine the contact angles of different fluids on each sample. Both DI water and API brine represent hydrophilic (water wetting) fluids, where API brine is composed

of 8% NaCl and 2% CaCl2 by weight. The high salinity characteristics in API brine represent reservoir formation fluid (Crowe, 1969). DT2 represents a hydrophobic (oil wetting) fluid, while THF and IPA represent an amphiphilic (both hydrophilic and hydrophobic) fluid; 20% THF or IPA was used with a lower surface tension than 100% IPA. Thin slabs were sanded or polished using 220-grit or 2000-grit sandpapers to reduce the roughness of the surface. Then, for each test, one thin slab was placed horizontally on an adjustable platform. A droplet of a fluid was pipetted onto the surface of a horizontal thin slab. The instrument recorded and measured droplet behavior and contact angle data with respect to time. Each thin slab could be used for two tests by flipping the thin slab over. These experiments investigate a rock surface's tendency to be water- or oil-wet on a millimeter scale. When fluid spreads on a sample surface, the surface is considered to be wetting towards this fluid and will subsequently have a small contact angle (Figure 3-17). In shale studies, a combination of contact angle and spontaneous imbibition tests are used to characterize wettability related connectivity of a sample.

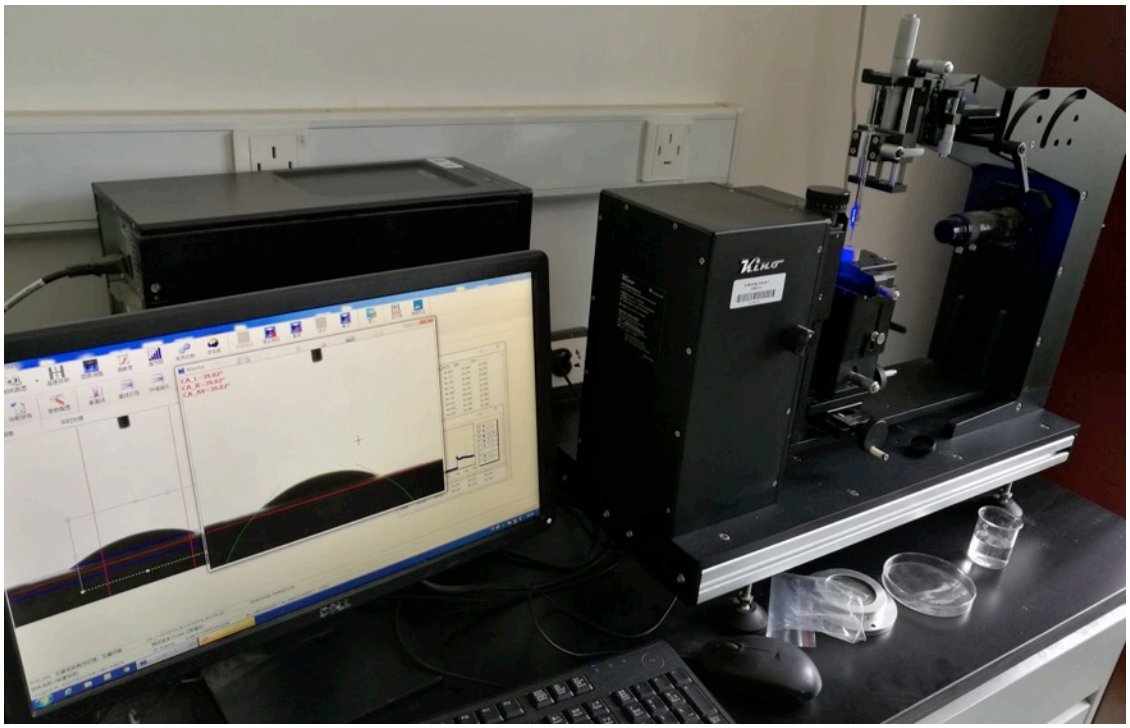

Figure 3-16: Photo of the SL200KB Optical Dynamic/ Static Interfacial Tensiometer and Contact Angle Meter used for contact angle measurement.

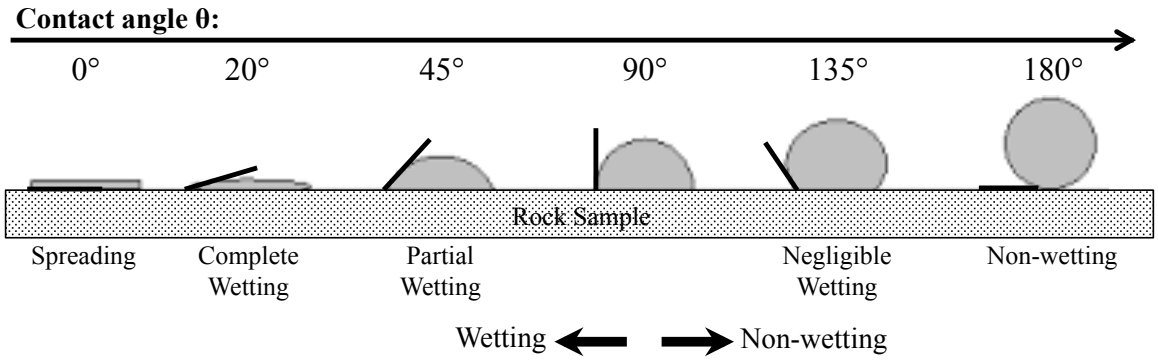

Figure 3-17: Contact angle schematic (modified after Majeed, 2014).

3-11 Well Log Analysis

3-11-1 Introduction to Well Log Analysis

Well logs provide direct and quantitative measurements of the rock properties surrounding a borehole, with an observational volume equating a radius of several feet. These

measurements can be plotted and viewed against other well logs for regional correlation of formations, structure mapping, and a variety of other useful tools that aid in subsurface interpretation, prediction, and exploration. Diamondback Energy provided the digital logs for the three wells. Further interpretation and calculation were performed using the IHS geologic interpretation software PETRA provided to UT Arlington. The calculations made on the initial log measurements can give additional information about the formation surrounding the borehole.

3-11-2 Procedure for Well Log Analysis

3-11-2-1 Shale Volume

The shale volume was derived from the gamma ray log. First the linear gamma ray index (I_{GR}) was determined using Eq. 3-14 and a histogram to determine max and min gamma ray values, which represent shale and carbonate/siliciclastics, respectively. Then the nonlinear Steiber model was used to determine the shale volume (Steiber, 1970) (Eq. 3-15).

$$I_{GR} = \frac{GR_{log} - GR_{min}}{GR_{max} - GR_{min}} \quad \text{Eq. 3-14}$$

$$V_{sh} = \frac{I_{GR}}{3 - 2 * I_{GR}} \quad \text{Eq. 3-15}$$

Where,

I_{GR}: Gamma ray index

GR_{log}: Measured gamma ray log (API)

GR_{min}: Gamma ray carbonate/siliciclastic value (API)

GR_{max}: Gamma ray shale value (API)

V_{Sh}: Shale volume

3-11-2-2 Total Porosity

The neutron and density porosity logs were averaged in order to determine the total porosity.

$$\Phi_t = \frac{DPHI+NPHI}{2} \quad \text{Eq. 3-16}$$

Where,

Φt: Total porosity (%)

DPHI: Density porosity (%)

NPHI: Measured neutron porosity (%)

3-11-2-3 Corrected Porosity

The corrected porosity log was created by trial and error using core and log data. The total porosity, density porosity, and neutron porosity curves were compared in order to determine which most closely fit the core data porosity points. The porosity curve that fit most closely was then shifted and scaled to determine a porosity curve that best imitated the core porosity data. Equation 3-17 below is an example of an equation used to shift and scale total porosity to a corrected porosity.

$$\Phi_C = (\Phi_t - 5) * .8 \quad \text{Eq. 3-17}$$

Where,

Φ_C: Corrected porosity (%)

3-11-2-4 Archie Water Saturation

The water saturation of a formation was determined using the Archie equation (Archie, 1942). Several constants as well as the deep resistivity log and water resistivity were used in the Archie equation. The resulting water saturation log can help determine if a formation interval is highly saturated with water leaving little room for hydrocarbons or vice versa. An average value of 0.035 ohmm was used for R_w (resistivity of water). This value was calculated for each well at a depth in the interval of interest using Equation 3-18. The cementation exponent and saturation

exponent were determined from literature on the Midland Basin, Wolfcamp oil reservoir (Holmes, 2017).

$$R_w = \frac{R_t * \Phi^m}{a} \quad \text{Eq. 3-18}$$

$$S_w = \left(\frac{a * R_w}{R_t * \Phi^m}\right)^{\frac{1}{n}} \quad \text{Eq. 3-19}$$

Where,

R_w: Water resistivity (ohmm)

R_t: Formation resistivity (ohmm)

Φ: Porosity (%)

m: Cementation exponent

S_w: Water saturation (%)

a: Tortuosity constant

n: Saturation exponent

3-11-2-5 Permeability

Permeability is an important property to evaluate when investigating a potential hydrocarbon bearing formation. Eq. 3-20 is from Timur (1986) and can only be used when the formation is at irreducible water saturation.

$$k = \left(\frac{93 * {\Phi_c}^{2.2}}{S_w}\right)^2 \quad \text{Eq. 3-20}$$

Where,

k: Permeability (mD)

3-11-2-6 Bulk Volume Water

Bulk volume water represents the volume of water held within the available pore space in a formation. When the bulk volume water is constant it typically indicates the formation is at

irreducible water saturation. However, irreducible water saturation can change by facies and constant BVW may not necessarily denote irreducible water saturation in complex reservoirs. Irreducible water saturation occurs within a formation when water no longer migrates due to capillary pressure (Morris and Biggs, 1967).

$$BVW = \Phi_c * S_w \quad \text{Eq. 3-21}$$

Where,

BVW: Bulk volume water

3-11-2-7 Clay Bound Water

Clay bound water represents the volume of water trapped in, held on to, and bonded to molecules within a shale (Crain, 1978).

$$CBW = BVW * V_{sh} \quad \text{Eq. 3-22}$$

Where,

CBW: Clay bound water

3-11-2-8 Bulk Volume Hydrocarbon

The bulk volume hydrocarbon is the calculated volume of hydrocarbon fluid that could be occupying available pore space.

$$BVH = \Phi_C - BVW - CBW \quad \text{Eq. 3-23}$$

Where,

BVH: Bulk volume hydrocarbon

3-11-2-9 Rock Mineral Properties

The rock mineral properties, TOC, kerogen, quartz, clay, and carbonate were calculated using a variety of equations listed below modified after Asquith (2010) with adjustments for Wolfcamp geologic conditions. In order for the rock mineral properties curves to function a

separate equation for total porosity had to be used (Asquith, 2010) (Eq.3-26). The resulting log curves were used to compare against core measurements to determine if this model is accurate for investigating intervals that were not sampled as well as other well logs throughout the basin.

3-11-2-9-1 TOC

The Schmoker and Hester (1983) equation was utilized to calculate the TOC log.

$$TOC_{LOG} = (\frac{156.956}{\rho_B}) - 58.271 \quad \text{Eq. 3-24}$$

Where,

TOC_{LOG}: TOC obtained from logging (wt%)

ρ_B: Measured bulk density (g/cm^3)

3-11-2-9-2 Kerogen Volume

$$V_{Ker} = \frac{(TOC * K_{VR} * \rho_B)}{\rho_{Ker}} \quad \text{Eq. 3-25}$$

Where,

V_{Ker}: Kerogen volume

K_{VR}: Kerogen maturity Index (1.2)

ρ_{Ker}: Kerogen density (g/cm^3)

3-11-2-9-3 Total Porosity for Mineralogy Curves

$$\Phi_{tm} = \frac{(NPHI - 0.35) + \left(-\frac{0.40}{0.06}\right) * \left((\rho_B - 2.71) + V_{Ker} * 0.06\right) + V_{Ker} * (-0.05)}{0.17 - \left(2.71 - \rho_f\right) * \left(-\frac{0.40}{0.06}\right)} \quad \text{Eq. 3-26}$$

$$\rho_f = (S_w * \rho_w) + ((1 - S_w) * \rho_h) \quad \text{Eq. 3-27}$$

Where,

Φ_{tm}: Total porosity used for mineralogy curves (%)

ρ_f: Fluid density (g/cm^3)

ρ_w: Water density (g/cm^3)

ρ_h: Hydrocarbon density (g/cm^3)

3-11-2-9-4 Quartz Volume

$$V_{qtz} = \frac{((\rho_B - \rho_{Cl}) + (V_{Ker} * (\rho_{Cl} - \rho_{qtz})) + (\Phi_{tm} * (\rho_{Cl} - \rho_f))}{(\rho_{qtz} - \rho_{cl})} \quad \text{Eq. 3-28}$$

Where,

V_{qtz}: Quartz volume (cm^3)

ρ_{Cl}: Calcite density (g/cm^3)

ρ_{qtz}: Quartz density (g/cm^3)

3-11-2-9-5 Clay Volume

An assumption was made that most shales are composed of 50-70% clay, so a cut-off of 60% was used (Bhuyan and Passey, 1994).

$$V_{cly} = V_{Sh} * 0.60 \quad \text{Eq. 3-29}$$

Where,

V_{cly}: Clay volume (cm^3)

3-11-2-9-6 Carbonate Volume

$$V_{Cl} = 1 - (V_{cly} + V_{qtz} + V_{Ker} + \Phi_{tm}) \quad \text{Eq. 3-30}$$

Where,

V_{Cl}: Carbonate Volume (cm^3)

3-12 Production Data

Production data, history, and general information for the three wells analyzed in this study was gathered from DrillingInfo Pro database and well log headers. Dr. Qinhong Hu's research group at the UT Arlington has access to a complimentary DrillingInfo subscription. DrillingInfo gathers production, completion, well log, and other useful data for wells all around the United States from an assortment of different sources and offers data analytics to observe

trends in production. This allowed production data to be viewed quickly and accurately, and linked to petrophysical and geochemical studies.

Chapter 4: Results

4-1 Vacuum-Assisted Fluid Immersion Porosimetry

Table 4-1 presents vacuum-assisted FIP results for Spraberry and Wolfcamp samples. Plugs were tested in DI water only to preserve sample for future experimentation. Three cubes were tested in DI water and results averaged, where two of these cubes were subsequently tested in either DT2 or THF. These different fluids can impact results based on wettability of as-received samples. Resulting properties from experimentation are edge-accessible porosity, bulk density, and grain density of samples displayed in Table 4-1, with respect to fluids and sample sizes. For most samples, porosity is relatively similar or increases as sample size decreases between plug and cube sizes. However, among cube samples, DT2 tests, as well as most THF tests, all consistently show larger porosity than DIW tests. It should be noted that high evaporation rates of THF could affect measurements, with reported values as low bounds. The porosity results for each testing method are compared for each well by depth in figure 4-1.

Table 4-1: Vacuum-assisted FIP results for plug and cube size samples in DIW, DT2, and THF (Fctd: fractured).

Sample ID	DIW						DT2			THF		
	Plug Size (~4.0cm equiv. sph dia.)			Cube Size (~0.9 cm equiv. sph dia.)								
	Porosity (%)	Bulk Density (g/cm^3)	Grain Density (g/cm^3)	Porosity (%)	Bulk Density (g/cm^3)	Grain Density (g/cm^3)	Porosity (%)	Bulk Density (g/cm^3)	Grain Density (g/cm^3)	Porosity (%)	Bulk Density (g/cm^3)	Grain Density (g/cm^3)
ME-8004	3.025	2.562	2.642									
ME-8027	0.083	2.682	2.684	0.079 ± 0.035	2.687 ± 0.004	2.689 ± 0.005	0.220	2.757	2.763	0.102	2.749	2.752
ME-8045	0.420	2.668	2.679									
ME-8063	2.440 (Fctd)	2.520	2.580									
ME-8435	0.291	2.621	2.629									
ME-8444	0.760	2.490	2.510									
ME-8455	0.842	2.598	2.620									
ME-8463	1.607	2.542	2.584									
ME-8621	0.594	2.613	2.628	0.437 ± 0.087	2.633 ± 0.013	2.645 ± 0.013	0.715	2.710	2.729	0.593	2.672	2.688
ME-8633	0.376	2.613	2.623	0.34 ± 0.242	2.651 ± 0.027	2.660 ± 0.021	0.971	2.710	2.737	1.214	2.673	2.705
ME-8832	1.330	2.430	2.460									
ME-8852	0.820	2.431	2.451									
ME-8866	0.208	2.644	2.650	0.135 ± 0.041	2.647 ± 0.007	2.644 ± 0.006	0.648	2.705	2.723	0.271	2.679	2.687
ME-9031	1.507	2.649	2.689	1.112 ± 0.315	2.653 ± 0.012	2.682 ± 0.005	1.476	2.729	2.770	2.280	2.683	2.745
ME-9039	1.020	2.700	2.730									
ME-9044												
ME-9052	6.601	2.497	2.673	6.238 ± 0.592	2.524 ± 0.016	2.692 ± 0.000	7.309	2.558	2.759	5.663	2.582	2.737
ME-9197	0.672	2.497	2.514	2.345 ± 0.158	2.479 ± 0.012	2.539 ± 0.016	3.310	2.511	2.597	2.379	2.495	2.556
ME-9207	0.291	2.628	2.635	0.457 ± 0.132	2.646 ± 0.015	2.658 ± 0.012	1.623	2.691	2.736	0.957	2.689	2.715
ME-9509	8.129 (Fctd)	2.413	2.626									
ME-9511	0.810	2.690	2.710									
ME-9528	0.110	2.670	2.670									
ST-8441	2.352	2.504	2.564									
ST-8877	2.694	2.601	2.673	3.191 ± 0.052	2.611 ± 0.008	2.697 ± 0.009	3.502	2.665	2.762	3.612	2.651	2.751
ST-9400	1.002	2.589	2.615									
ST-9605	1.775	2.537	2.583									
ST-9612	0.295	2.640	2.648	0.370 ± 0.136	2.632 ± 0.013	2.641 ± 0.009	1.051	2.693	2.721	1.290	2.673	2.707
ST-9632	0.420	2.610	2.630	0.210 ± 0.240	2.663 ± 0.037	2.669 ± 0.044	0.657	2.701	2.719	0.297	2.690	2.698
ST-9833	0.130	2.690	2.690									
ST-9841	4.261	2.504	2.616	6.114 ± 0.355	2.513 ± 0.013	2.677 ± 0.012	7.431	2.553	2.758	6.556	2.555	2.734
ST-9849	1.110	2.480	2.500	2.178 ± 0.244	2.485 ± 0.014	2.540 ± 0.010	3.043	2.553	2.633	3.033	2.499	2.577
ST-10053	5.423 (Fctd)	2.511	2.655									
ST-10067	0.568	2.647	2.662									
ST-10310	5.500 (Fctd)	2.486	2.630									
ST-10318	0.673	2.670	2.688									
ST-10322	2.339	2.537	2.598									
JB-9187	2.443	2.522	2.585	4.214 ± 0.136	2.534 ± 0.019	2.646 ± 0.018	5.907	2.595	2.758	6.025	2.571	2.736
JB-9209	1.185	2.541	2.571									
JB-9733	0.255	2.601	2.607	0.158 ± 0.020	2.602 ± 0.002	2.606 ± 0.002	1.034	2.670	2.698	0.625	2.659	2.675
JB-9781	0.293	2.472	2.479	1.196 ± 0.094	2.520 ± 0.024	2.550 ± 0.025	2.521	2.519	2.584	1.592	2.496	2.537
JB-9849	0.182	2.667	2.672									
JB-9867	0.580	2.548	2.562									
JB-9871	0.362	2.691	2.701	0.170 ± 0.081	2.704 ± 0.014	2.709 ± 0.016	0.453	2.736	2.749	0.176	2.741	2.746
JB-9891	0.257	2.706	2.713	0.526 ± 0.032	2.695 ± 0.005	2.710 ± 0.004	0.861	2.752	2.776	0.336	2.747	2.756
JB-9904	0.303	2.612	2.620									
JB-10525	1.860	2.550	2.600									
JB-10570	1.884	2.581	2.631									
JB-10595	0.070	2.750	2.760									

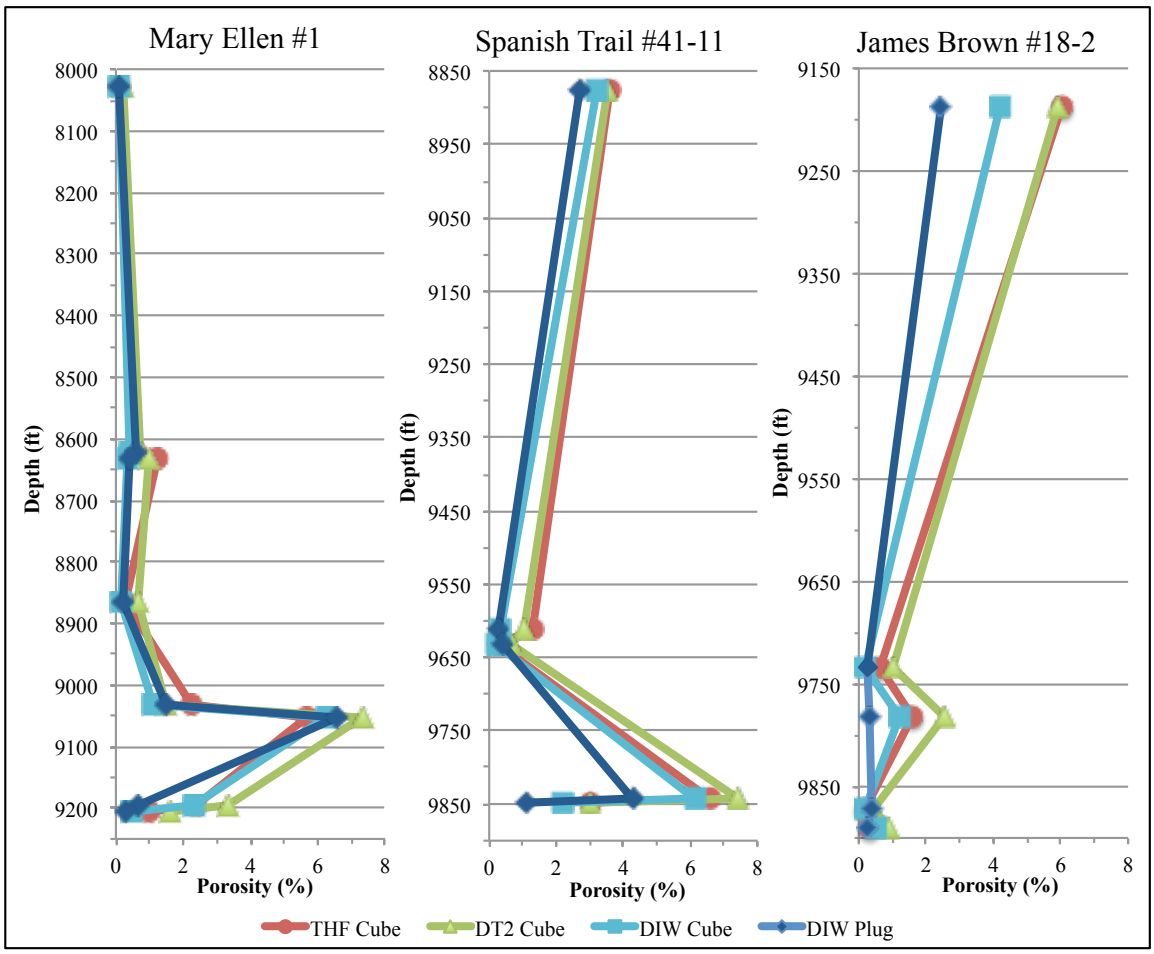

Figure 4-1: Porosity methods comparison by depth for each well.

4-2 X-Ray Diffraction (XRD)

Mineralogy data from XRD analyses are displayed in Table 4-2. XRD results illustrate a total of 10 minerals identified in Spraberry and Wolfcamp samples. Five of 18 samples tested illustrate a quartz/feldspar-dominated composition, where the other 13 display a carbonate-dominated composition. Samples generally displayed clay composition less than 23%, with 10 of 18 samples illustrating 0% clay content (Table 4-2). Pyrite was detected in 14 of 18 samples, however only two samples (ST-9849 and JB-9187) show appreciable percentages (Table 4-2). Pyrite typically forms in organic matter rich, anaerobic environments and can indicate a deep-

water marine depositional environment. The mineral compositions for each sample are visually displayed in Figure 4-2.

The minerals present (sans pyrite) were upscaled into three groups, quartz+feldspar, carbonates, and clays, to plot samples on a ternary diagram used to classify rock type (Schlumberger, 2014) (Figure 4-3). The samples plotted illustrate five different lithofacies present with a majority being carbonate dominated lithotypes (Figure 4-3).

Table 4-2: XRD results showing the mineral composition of each sample in weight percent.

	Composition (wt.%)									
Sample ID	**Quartz** Silica	**Albite** Feldspar	**Anorthite** Feldspar	**Calcite** Carbonate	**Dolomite** Carbonate	**Kutnohorite** Carbonate	**Illite** Clay-Mica	**Montmollorite** Clay-Smectite	**Clinochlore** Clay-Chlorite	**Pyrite** Sulfide
ME-8027	7.8			92.2						
ME-8621	13.8	0.7		83.3	1.2					0.9
ME-8633	11.5			87.3	0.6					0.6
ME-8866	6.7			93.2						0.1
ME-9031	4.4			93.1	2.4					
ME-9052	19			78	3					
ME-9197	56.6	3.6	3.4	8.1	1.9		20.1	0.7	0.7	5
ME-9207	17.8	0.9		73.3	6			0.7		1.2
ST-8877	54.9	8.7	2.4	9.5	17.9		4.9		0.5	1.2
ST-9612	9.1	0.8		86.6	3					0.4
ST-9632	9.7	0.3		88.1	1.4					0.5
ST-9841	1.2	0.4		89.3	9.2					
ST-9849	61.8	5.4	3.9	1.3			22.4		0.6	4.6
JB-9187	59.7	6.1	3.5	2.1		7.8	16.8	0.3	1	2.7
JB-9733	11.9	1.3		80.4	4.7		1.1			0.6
JB-9781	48.7	6.7		14.1		10.4	16.7		0.4	3
JB-9871	4.6	0.5		92.2		2	0.2			0.5
JB-9891	5	1.5		64.5	28.3					0.8

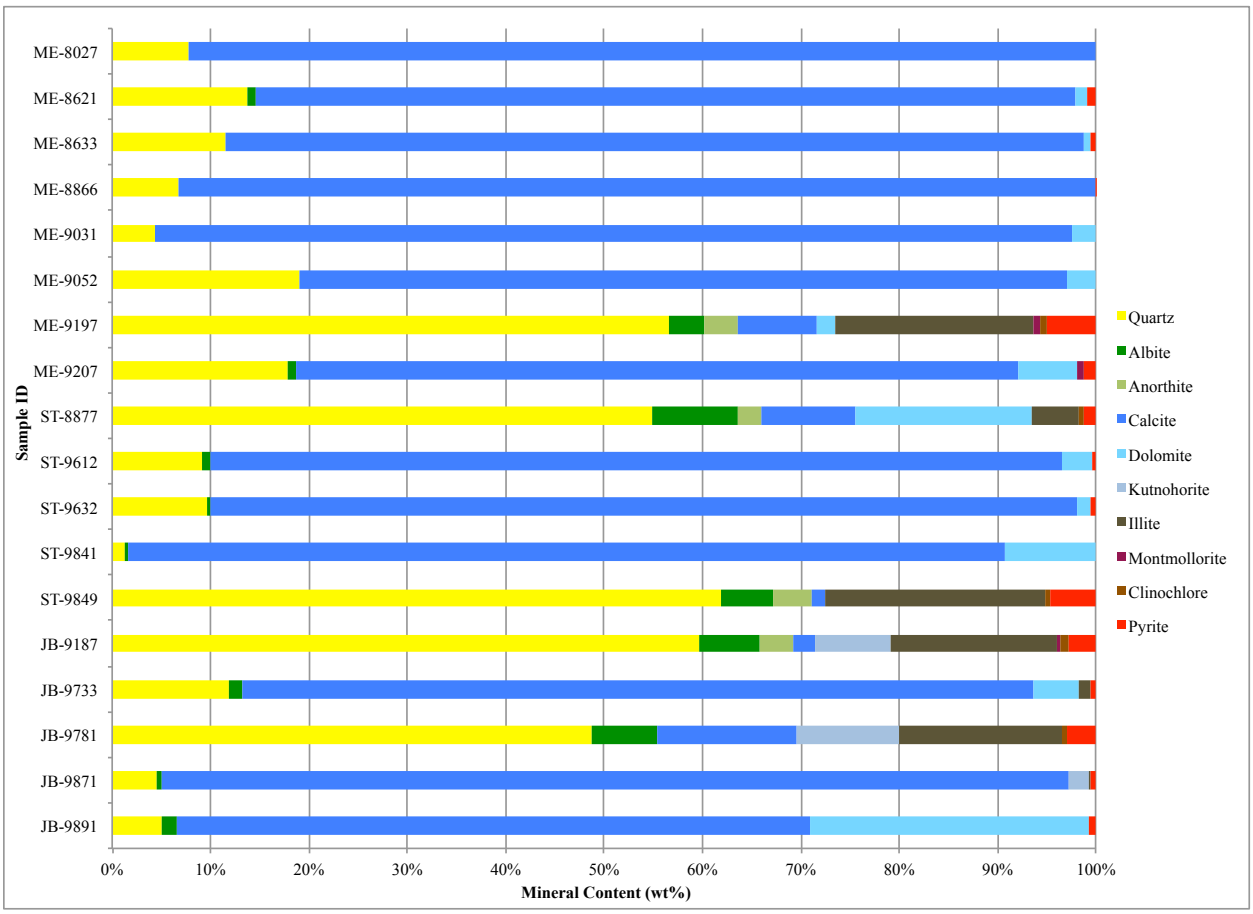

Figure 4-2: Stacked bar chart showing the mineral composition of samples.

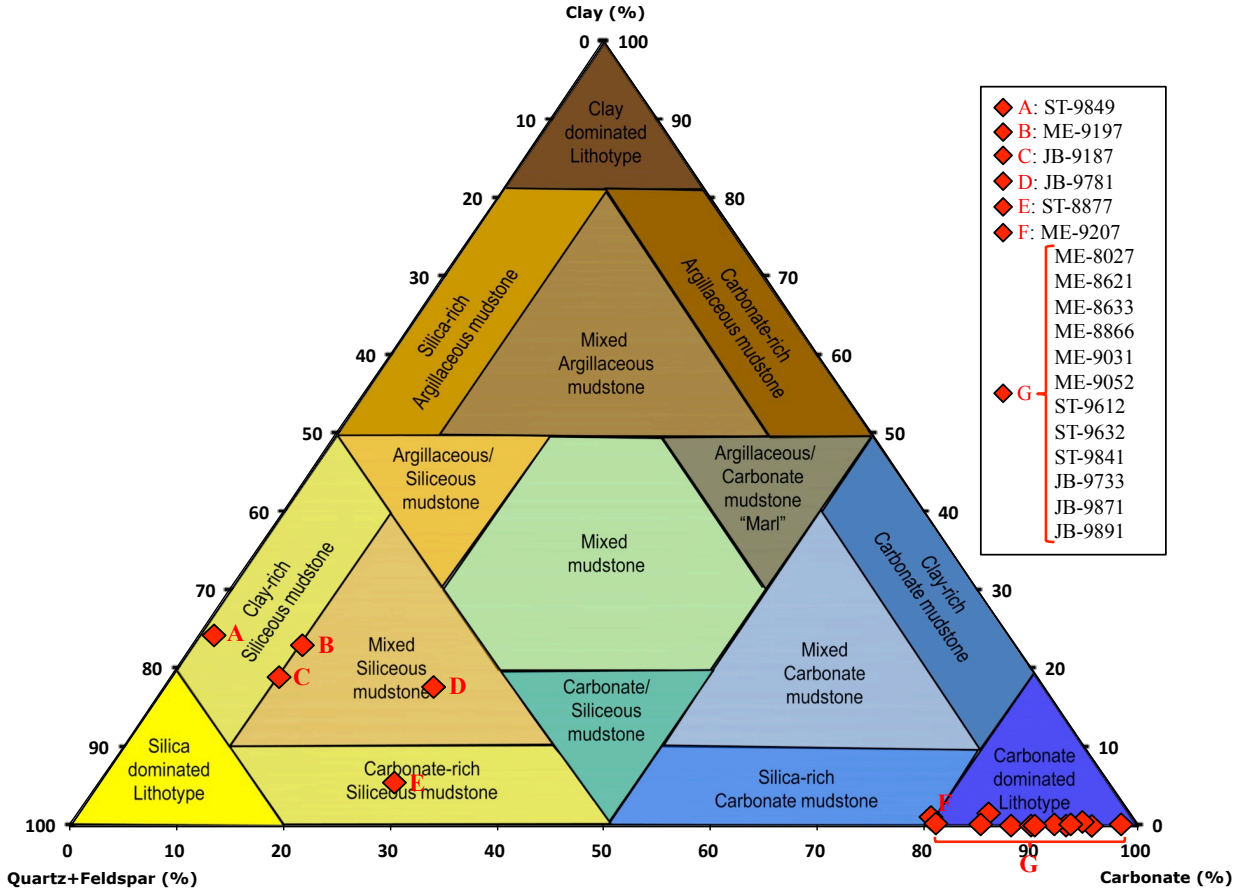

Figure 4-3: Mudrock lithofacies ternary diagram with plotted samples as red diamonds. (modified from Schlumberger, 2014)

4-3 Geochemistry - Total Organic Carbon (TOC) and Pyrolysis

Geochemistry data measured directly, or calculated, from LECO TOC and pyrolysis analyses on powder-sized samples are shown in Table 4-3. Measured and calculated values are described in Table 3-4. As illustrated in Table 4-3, TOC values vary, but the three highest values coincide with the highest clay compositions from XRD data in samples ME-9197, ST-9849, and JB-9781. Calculated vitrinite reflectance values, based on T_{max} results from pyrolysis and the equation in Jarvie (2018) from similar shale plays, placed 13 of 15 samples in the oil generation window, with ST-9841 and JB-9871 interpreted as immature (Figure 4-9).

Kerogen type was estimated with the Pseudo Van Krevelen plot of oxygen index vs. hydrogen index (Figure 4-7), kerogen quality plot of TOC vs. S2 (Figure 4-8), and kerogen type plot of T_{max} vs. hydrogen index (Figure 4-9). All three methods of determining kerogen type put the samples within the type II and III kerogen range. The S1, free oil, value is used with TOC to determine the normalized oil content, where a normalized oil content value from 0-25 indicates low maturity, 25-50 indicates early mature, 50-100 indicates mature, and >100 indicates oil/gas production. Most (14 of the 15) samples tested have a normalized oil content in the range of early mature to production, where only JB-9891 is out of the early mature window at a normalized oil content of 23 (Figures 4-4, 4-5, and 4-6). However, normalized oil content must be normalized to rock type and is most appropriate in organic-rich mudstones, where organic-poor carbonates with high S1 values likely indicate migrated oil that was not generated at that location.

The S2 value is used with TOC to determine the hydrogen index of each sample, where the S3 value is used with TOC to determine the oxygen index. The hydrogen index and oxygen index are plotted against each other in the Van Krevelen plot to determine kerogen type (Figure 4-7). The hydrogen index is related to T_{max} for a secondary kerogen type interpretation as well as maturity indicator (Figure 4-9). The S2 value is related to TOC to determine kerogen quality (Figure 4-8). The production index (PI) is determined using S1 and S2 values, where a PI <0.10 correlates with non-productive zones, 0.10-0.30 correlates with the oil generation zones, and >0.30 correlates with the gas generation/oil cracking zones (Figures 4-4, 4-5, and 4-6). The production index values are related to T_{max} for a secondary assessment of kerogen quality that illustrates almost all samples are in the oil zone (Figure 4-10). The S4 value represents residual carbon left in the sample. Lastly, the percent carbonate of each sample is found from treating

each sample with acid before testing and comparing weights, where percent carbonate values are only slightly lower than carbonate weight percentages determined from XRD (Tables 4-2 and 4-3).

Table 4-3: TOC and pyrolysis results.

Sample ID	**TOC** (wt%)	**Vitrinte Refelectance** (%Ro) Calculated	**Kerogen Type Estimated**	**S1**	**S2**	**S3**	**S4**	**Tmax** (°C)	**Hydrogen Index**	**Oxygen Index**	**Production Index**	**Normalized Oil Content** S1/TOC	**Carbonate** (wt%)
ME-8027													
ME-8621	1.40	0.75	II	0.72	2.35	0.41	11.5	440	168	29	0.23	51	75.0
ME-8633	1.23	0.75	II	0.73	2.14	0.32	9.92	440	174	26	0.25	59	81.1
ME-8866	0.74	0.70	III	0.43	0.97	0.31	6.24	437	132	42	0.31	58	86.4
ME-9031	0.32	0.72	III	0.18	0.36	0.31	2.75	438	114	98	0.33	57	92.9
ME-9052	0.29	0.68	III	0.35	0.53	0.33	2.17	436	186	116	0.40	123	77.0
ME-9197	2.99	0.70	I-II	1.49	4.41	0.38	25.0	437	147	13	0.25	50	13.6
ME-9207	1.16	0.70	III	0.82	1.53	0.37	9.65	437	132	32	0.35	71	69.1
ST-8877													
ST-9612	1.02	0.62	III	0.86	1.90	0.40	7.91	432	186	39	0.31	84	82.0
ST-9632	1.47	0.80	II	1.34	2.75	0.29	11.3	443	187	20	0.33	91	80.9
ST-9841	0.54	0.54	II-III	1.08	1.46	0.24	3.29	427	270	44	0.43	200	96.0
ST-9849	2.97	0.70	II	2.21	5.84	0.38	23.0	437	197	13	0.27	74	10.3
JB-9187													
JB-9733	1.58	0.68	II	0.97	5.45	0.35	10.5	436	345	22	0.15	61	76.9
JB-9781	3.50	0.68	I-II	1.65	13.5	0.32	22.5	436	384	9	0.11	47	21.4
JB-9871	0.38	0.57	III	0.22	0.93	0.31	2.85	429	242	81	0.19	57	90.9
JB-9891	0.69	0.67	III	0.16	1.32	0.46	5.67	435	192	67	0.11	23	83.9

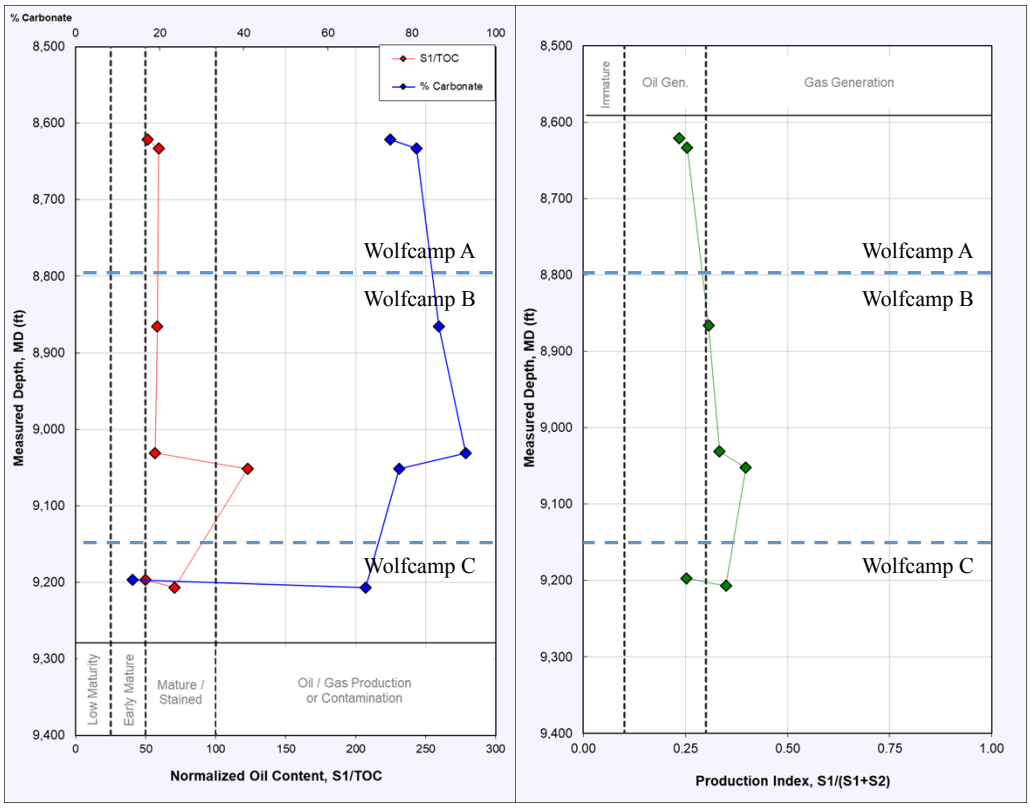

Figure 4-4: Mary Ellen #1 samples normalized oil content (left) and production index (right) by depth.

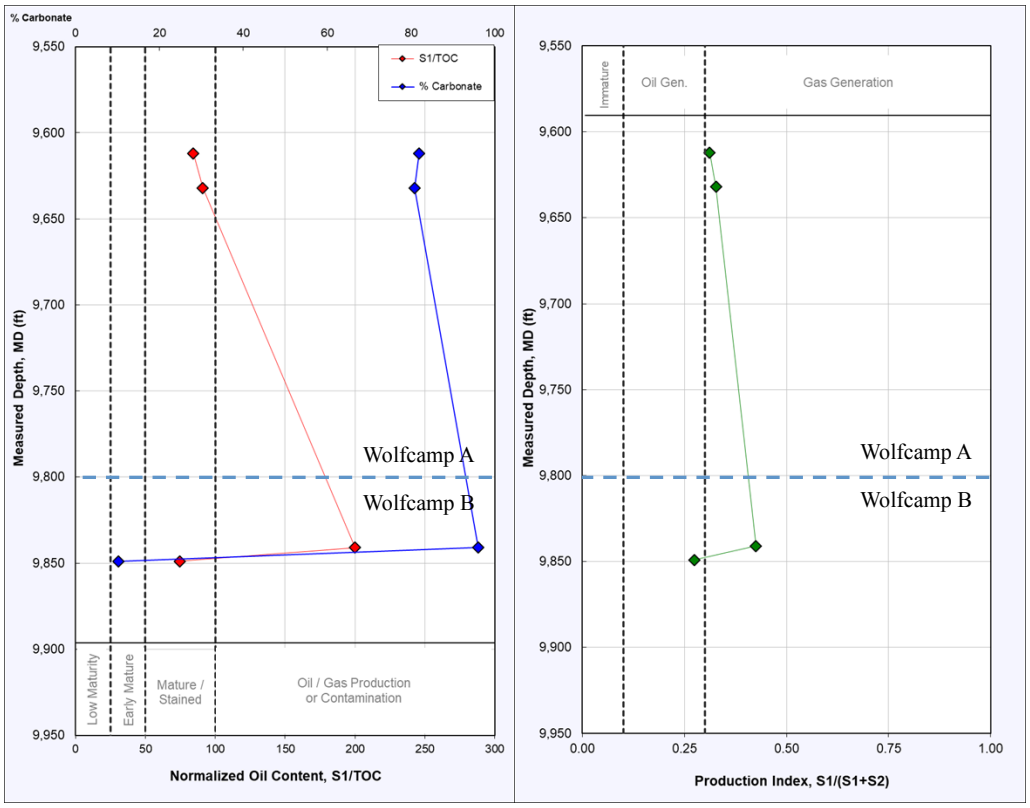

Figure 4-5: Spanish Trail #41-11 samples normalized oil content (left) and production index (right) by depth.

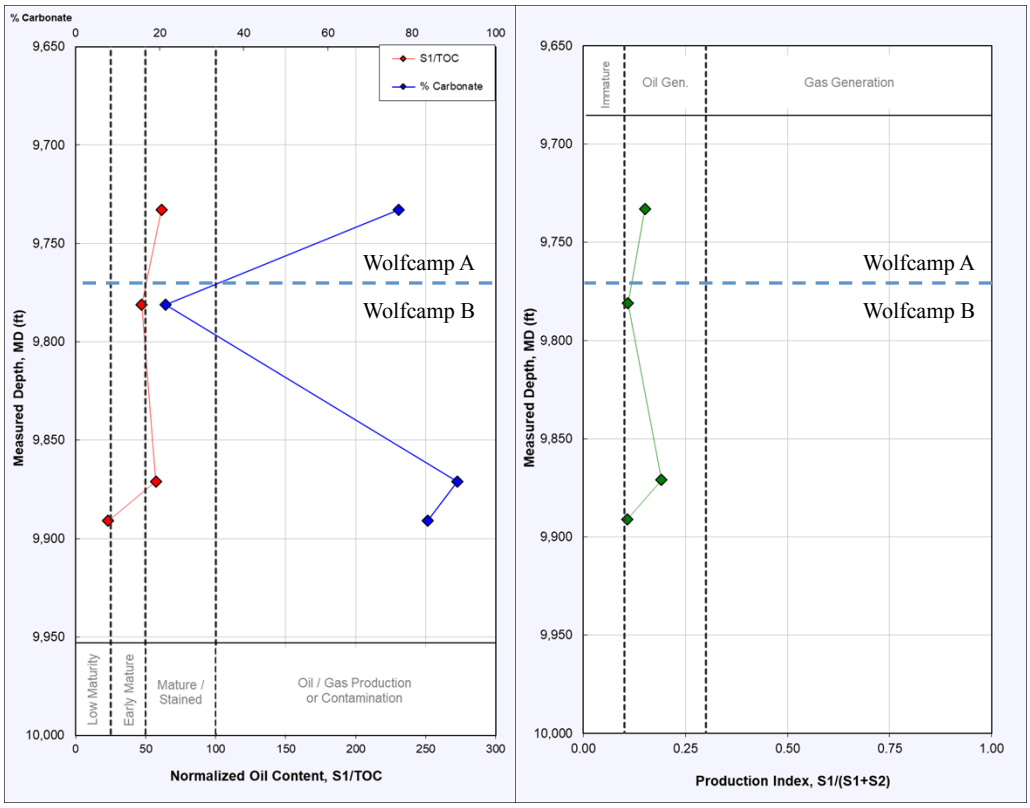

Figure 4-6: James Brown #18-2 samples normalized oil content (left) and production index (right) by depth.

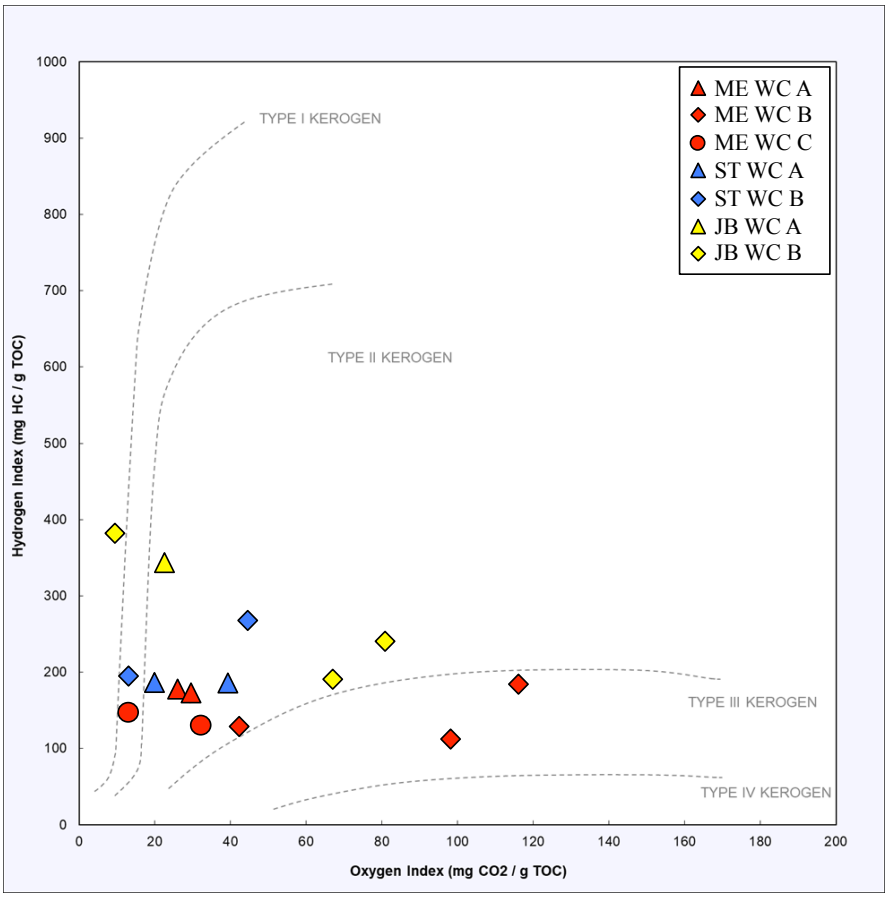

Figure 4-7: Pseudo Van Krevelen plot for 15 samples showing possible kerogen types.

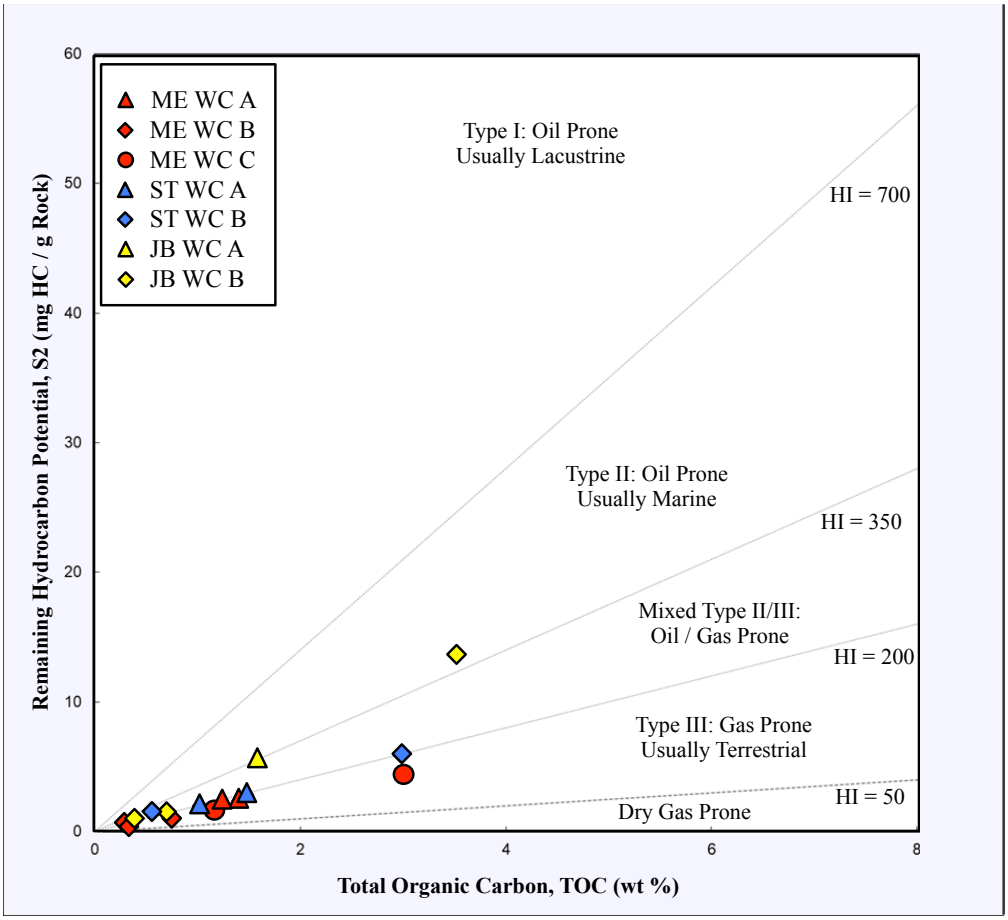

Figure 4-8: Kerogen quality plot for 15 samples.

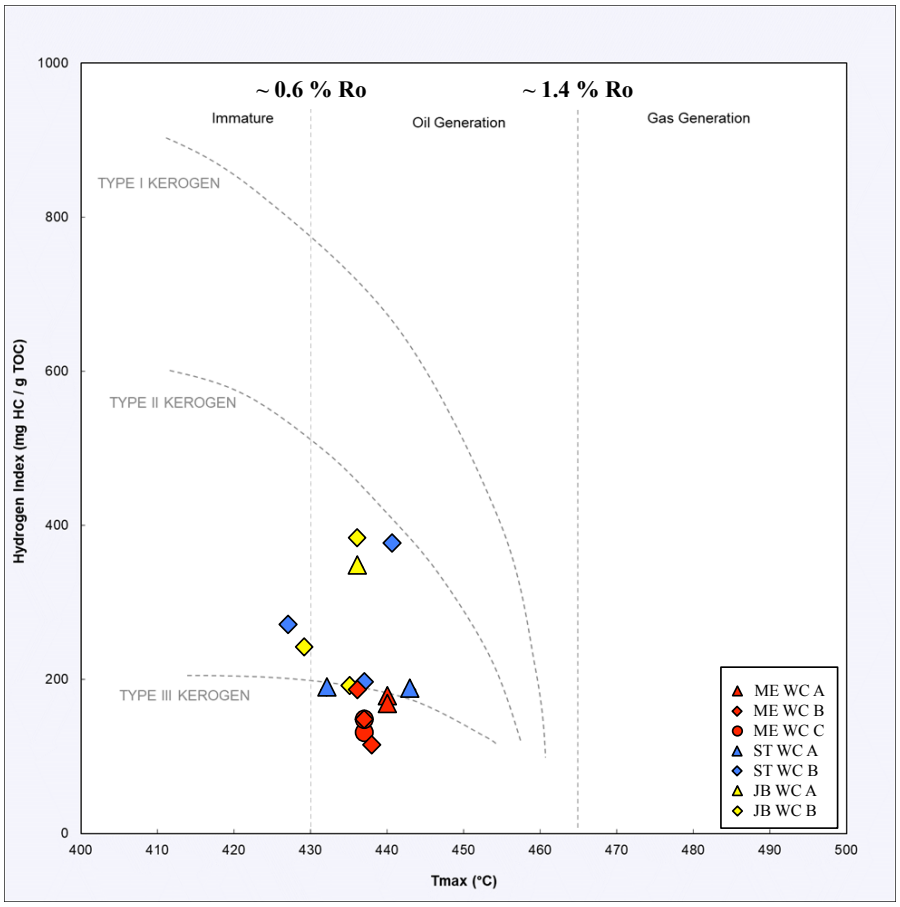

Figure 4-9: Kerogen type and maturity based on calculated vitrinite reflectance (Ro).

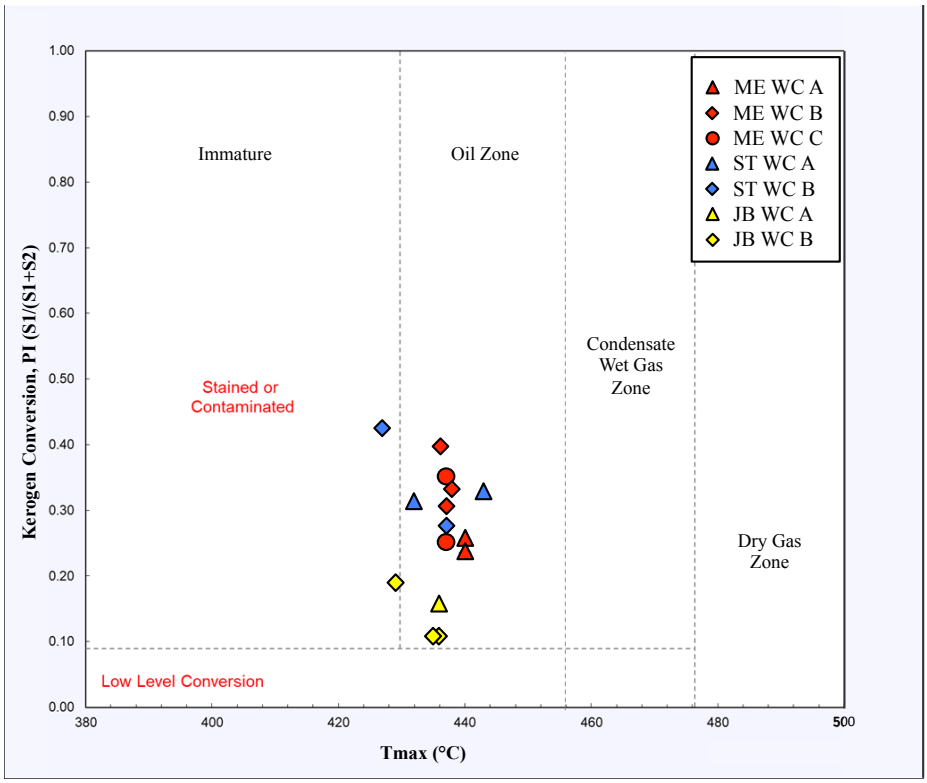

Figure 4-10: Kerogen quality plot showing potential hydrocarbon zones.

4-4 Liquid Pycnometry

The results from liquid pycnometry data for both DI water and DT2 are displayed in Table 4-4. For better comparison, each sample size fraction was converted into equivalent spherical diameter. A common trend observed is a general decrease in apparent bulk density as sample size decreases.

Table 4-4: Apparent bulk density results calculated from the liquid pycnometry test data.

Sample ID	**Size Designation**	**Size**	**Equivalent Spherical Diameter** (cm)	**Apparent Bulk Density** (g/cm^3)	
				DI Water	**DT2**
ME-8027	GRI+	1.70 - 2.36 mm	0.2030		
	A	841 - 1700 µm	0.1271		
	GRI	500 - 841 µm	0.0671		
	B	177 - 500 µm	0.0339	2.783 ± 0.119	2.710 ± 0.011
	C	75 - 177 µm	0.0126	2.744 ± 0.150	2.649 ± 0.053
ME-8621	GRI+	1.70 - 2.36 mm	0.2030	2.776 ± 0.041	2.639 ± 0.045
	A	841 - 1700 µm	0.1271	2.399 ± 0.397	2.621 ± 0.037
	GRI	500 - 841 µm	0.0671	2.188 ± 0.744	
	B	177 - 500 µm	0.0339	1.374 ± 0.017	2.611 ± 0.005

	C	75 - 177 µm	0.0126	1.811 ± 0.669	2.629 ± 0.036
ME-8633	GRI+	1.70 - 2.36 mm	0.2030	2.341 ± 0.009	2.693 ± 0.019
	A	841 - 1700 µm	0.1271	1.863 ± 0.019	2.701 ± 0.020
	GRI	500 - 841 µm	0.0671	1.514 ± 0.097	
	B	177 - 500 µm	0.0339	1.646 ± 0.366	2.629 ± 0.039
	C	75 - 177 µm	0.0126	1.234 ± 0.039	2.565 ± 0.001
ME-8866	GRI+	1.70 - 2.36 mm	0.2030	2.652 ± 0.318	2.696 ± 0.026
	A	841 - 1700 µm	0.1271	2.514 ± 0.361	2.686 ± 0.009
	GRI	500 - 841 µm	0.0671	2.307 ± 0.658	
	B	177 - 500 µm	0.0339	1.764 ± 0.169	2.677 ± 0.042
	C	75 - 177 µm	0.0126	2.020 ± 1.147	2.601 ± 0.001
ME-9031	GRI+	1.70 - 2.36 mm	0.2030	2.739 ± 0.163	2.694 ± 0.003
	A	841 - 1700 µm	0.1271	2.763 ± 0.176	2.709 ± 0.046
	GRI	500 - 841 µm	0.0671	2.773 ± 0.068	
	B	177 - 500 µm	0.0339	2.706 ± 0.119	2.703 ± 0.023
	C	75 - 177 µm	0.0126	2.956 ± 0.272	2.629 ± 0.046
ME-9052	GRI+	1.70 - 2.36 mm	0.2030		
	A	841 - 1700 µm	0.1271		
	GRI	500 - 841 µm	0.0671		
	B	177 - 500 µm	0.0339	1.684 ± 0.386	2.693 ± 0.006
	C	75 - 177 µm	0.0126	1.962 ± 0.853	2.639 ± 0.027
ME-9197	GRI+	1.70 - 2.36 mm	0.2030	2.408 ± 0.196	2.531 ± 0.030
	A	841 - 1700 µm	0.1271	2.327 ± 0.068	2.531 ± 0.043
	GRI	500 - 841 µm	0.0671	2.338 ± 0.229	
	B	177 - 500 µm	0.0339	1.780 ± 0.139	2.503 ± 0.053
	C	75 - 177 µm	0.0126	0.804 ± 0.052	2.389 ± 0.097
ME-9207	GRI+	1.70 - 2.36 mm	0.2030	2.637 ± 0.069	2.643 ± 0.001
	A	841 - 1700 µm	0.1271	2.629 ± 0.201	2.648 ± 0.013
	GRI	500 - 841 µm	0.0671	2.450 ± 0.330	
	B	177 - 500 µm	0.0339	1.896 ± 0.232	2.616 ± 0.023
	C	75 - 177 µm	0.0126	2.120 ± 0.000	2.530 ± 0.019
ST-8877	GRI+	1.70 - 2.36 mm	0.2030	2.697 ± 0.129	2.498 ± 0.211
	A	841 - 1700 µm	0.1271	2.691 ± 0.095	2.683 ± 0.059
	GRI	500 - 841 µm	0.0671	2.700 ± 0.198	
	B	177 - 500 µm	0.0339	2.693 ± 0.059	2.664 ± 0.087
	C	75 - 177 µm	0.0126	2.690 ± 0.072	2.525 ± 0.018
ST-9612	GRI+	1.70 - 2.36 mm	0.2030	2.617 ± 0.058	2.621 ± 0.025
	A	841 - 1700 µm	0.1271	2.228 ± 0.525	2.644 ± 0.033
	GRI	500 - 841 µm	0.0671	2.148 ± 0.309	
	B	177 - 500 µm	0.0339	1.539 ± 0.263	2.629 ± 0.029
	C	75 - 177 µm	0.0126	2.358 ± 0.908	2.621 ± 0.085
ST-9632	GRI+	1.70 - 2.36 mm	0.2030	2.488 ± 0.301	2.661 ± 0.117
	A	841 - 1700 µm	0.1271	2.179 ± 0.209	2.580 ± 0.078
	GRI	500 - 841 µm	0.0671	1.789 ± 0.036	
	B	177 - 500 µm	0.0339	1.253 ± 0.033	1.865 ± 1.133
	C	75 - 177 µm	0.0126	1.134 ± 0.017	2.513 ± 0.057
ST-9841	GRI+	1.70 - 2.36 mm	0.2030	2.355 ± 0.034	1.919 ± 1.106

	A	841 - 1700 µm	0.1271	2.201 ± 0.202	2.557 ± 0.079
	GRI	500 - 841 µm	0.0671	1.580 ± 0.465	
	B	177 - 500 µm	0.0339	1.768 ± 0.589	2.617 ± 0.049
	C	75 - 177 µm	0.0126	1.291 ± 0.082	2.609 ± 0.123
ST-9849	GRI+	1.70 - 2.36 mm	0.2030	2.453 ± 0.041	2.363 ± 0.151
	A	841 - 1700 µm	0.1271	2.272 ± 0.240	2.365 ± 0.140
	GRI	500 - 841 µm	0.0671	1.551 ± 0.167	
	B	177 - 500 µm	0.0339	2.108 ± 0.513	2.375 ± 0.140
	C	75 - 177 µm	0.0126	2.206 ± 0.908	2.314 ± 0.125
JB-9187	GRI+	1.70 - 2.36 mm	0.2030		
	A	841 - 1700 µm	0.1271		
	GRI	500 - 841 µm	0.0671		
	B	177 - 500 µm	0.0339	2.636 ± 0.134	2.526 ± 0.088
	C	75 - 177 µm	0.0126	2.596 ± 0.129	2.482 ± 0.061
JB-9733	GRI+	1.70 - 2.36 mm	0.2030	2.191 ± 0.467	2.639 ± 0.055
	A	841 - 1700 µm	0.1271	2.039 ± 0.783	1.526 ± 1.361
	GRI	500 - 841 µm	0.0671	1.874 ± 0.223	
	B	177 - 500 µm	0.0339	1.649 ± 0.532	2.444 ± 0.141
	C	75 - 177 µm	0.0126	1.209 ± 0.114	2.503 ± 0.094
JB-9781	GRI+	1.70 - 2.36 mm	0.2030	2.421 ± 0.148	2.509 ± 0.017
	A	841 - 1700 µm	0.1271	2.211 ± 0.310	2.424 ± 0.103
	GRI	500 - 841 µm	0.0671	1.980 ± 0.232	
	B	177 - 500 µm	0.0339	1.183 ± 0.021	2.389 ± 0.050
	C	75 - 177 µm	0.0126	1.091 ± 0.038	2.371 ± 0.103
JB-9871	GRI+	1.70 - 2.36 mm	0.2030	2.673 ± 0.256	2.694 ± 0.044
	A	841 - 1700 µm	0.1271	2.637 ± 0.250	2.656 ± 0.088
	GRI	500 - 841 µm	0.0671	2.558 ± 0.216	
	B	177 - 500 µm	0.0339	2.497 ± 0.173	2.613 ± 0.084
	C	75 - 177 µm	0.0126	2.819 ± 0.290	1.925 ± 1.046
JB-9891	GRI+	1.70 - 2.36 mm	0.2030	2.846 ± 0.136	1.672 ± 1.442
	A	841 - 1700 µm	0.1271	2.793 ± 0.124	1.659 ± 1.464
	GRI	500 - 841 µm	0.0671	2.93 ± 0.067	
	B	177 - 500 µm	0.0339	2.725 ± 0.001	2.604 ± 0.054
	C	75 - 177 µm	0.0126	2.993 ± 0.426	2.507 ± 0.040

4-5 Spontaneous Fluid Imbibition

Spontaneous imbibition tests were run on cube sized samples using DI water and DT2 to relate pore connectivity to a fluid. Data acquired was plotted on a graph of cumulative imbibition (mm; logarithmic) vs. time (sec; logarithmic) to determine trends in imbibition rate by identifying characteristic slopes in the data (Figures 4-11 to 16). Based on imbibition plots, imbibition behavior can be divided into four stages, each with its own representative slope. Stage

I lasts a few seconds and has the highest rate of change of all four stages, but can have fluctuations resulting from movement related to the sample first contacting fluid. Once the sample has settled, Stage II occurs when the sample first imbibes fluid. Stage II has the 2nd highest rate of change of all four stages due to edge accessible pores and microfractures being invaded first. Stage III occurs when fluid fills the edge accessible pore network and begins to enter the inner pore network. Stage III is used to qualitatively represent connectivity of a pore network and exhibits a nearly linear and constant slope that is lower than its predecessor due to differences in edge accessible and matrix pore networks. If present, Stage IV is the last stage of the test and occurs when fluid reaches the top of the sample or imbibition stops.

Rate of change for each stage of imbibition were identified for DI water and DT2 tests on all samples (Figures 4-11 to 16). Complexity of a wettable pore network coupled with duration, causes a sample to not display all four stages. The slopes for wall and edge stage (II) and interior stage (III) for DI water and DT2 are displayed in Table 4-5. Connectivity shown represents connection of inner matrix pore network from slope values in stage III. During stage III, values >0.47 have high connectivity, values from 0.30 to 0.47 have intermediate connectivity, and values <0.30 have low connectivity (Hu et al., 2012). From Table 4-5, a trend emerges for samples having low connectivity to DI water and high connectivity to DT2 with few exceptions.

Table 4-5: Imbibition results for DI water and DT2 fluids.

Sample ID	DI Water			DT2		
	Wall and Edge Slope	Interior Stage Slope	Connectivity	Wall and Edge Slope	Interior Stage Slope	Connectivity
ME-8027	0.667	0.244	Low		0.508	High
ME-8621	0.474	0.266	Low	0.837	0.290	Low
ME-8633	0.838	0.281	Low	0.667	0.082	Low
ME-8866	0.468	0.241	Low	1.247	0.667	High
ME-9031	0.446	0.142	Low		0.329	Intermediate
ME-9052	0.248	0.137	Low	0.706	0.365	Intermediate
ME-9197	0.728	0.274	Low	1.486	0.873	High
ME-9207	0.728	0.252	Low	0.520	0.186	Low
ST-8877	0.304	0.14	Low	0.621	0.317	Intermediate
ST-9612	1.325	0.667	High	1.063	0.576	High
ST-9632	1.133	0.161	Low	1.259	0.546	High
ST-9841	1.065	0.347	Intermediate	0.082	0.553	High
ST-9849	0.552	0.17	Low		0.592	High
JB-9187	0.287	0.228	Low	1.159	0.558	High
JB-9733	0.248	0.124	Low	0.818	0.630	High
JB-9781	0.813	0.475	High	1.506	0.096	Low
JB-9871	0.283	0.181	Low	0.895		
JB-9891	0.719	0.241	Low		0.793	High

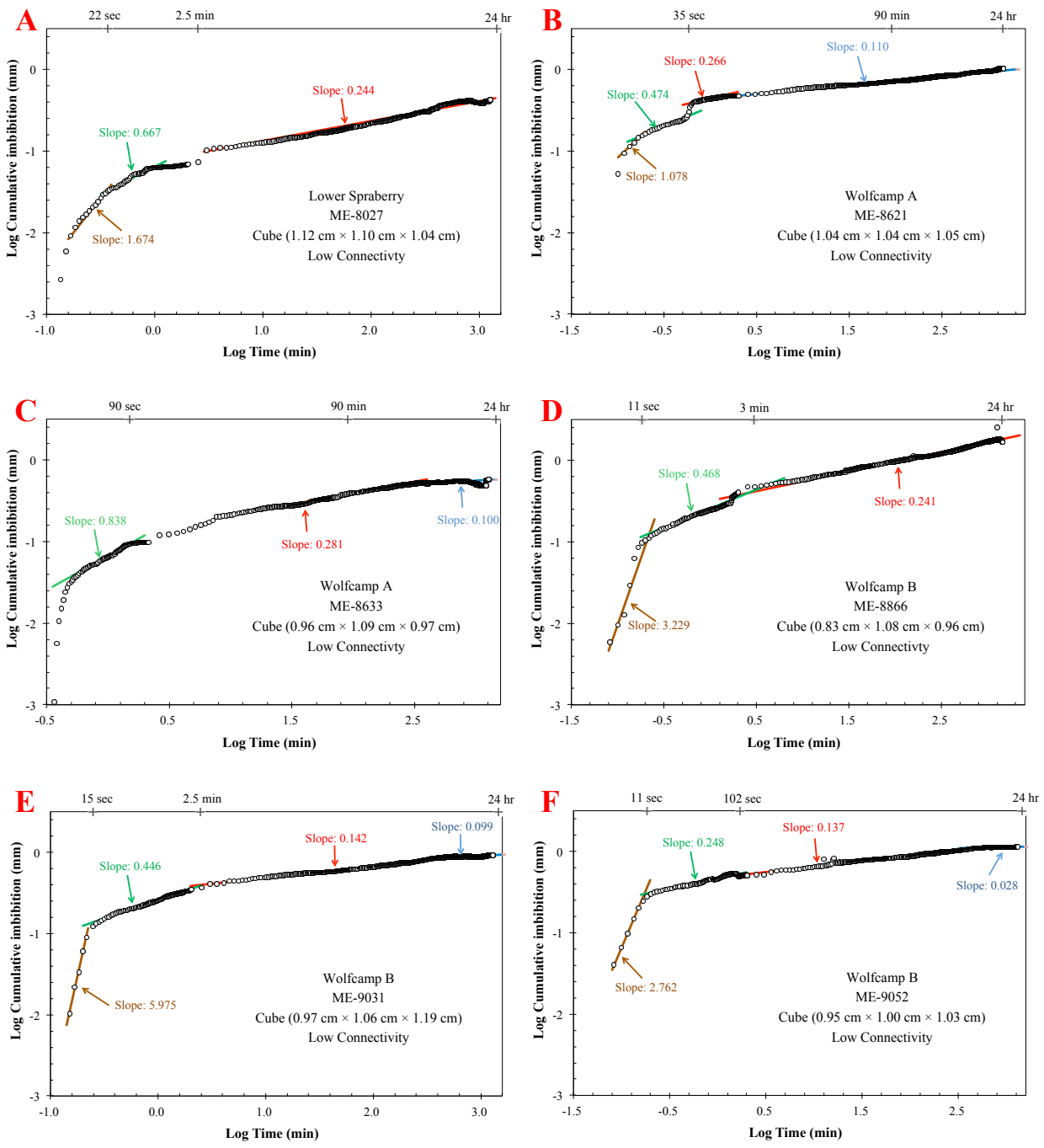

Figure 4-11: DI Water imbibition slopes for ME-8027 (A), ME-8621 (B), ME-8633 (C), ME-8866 (D), ME-9031 (E), and ME-9052 (F).

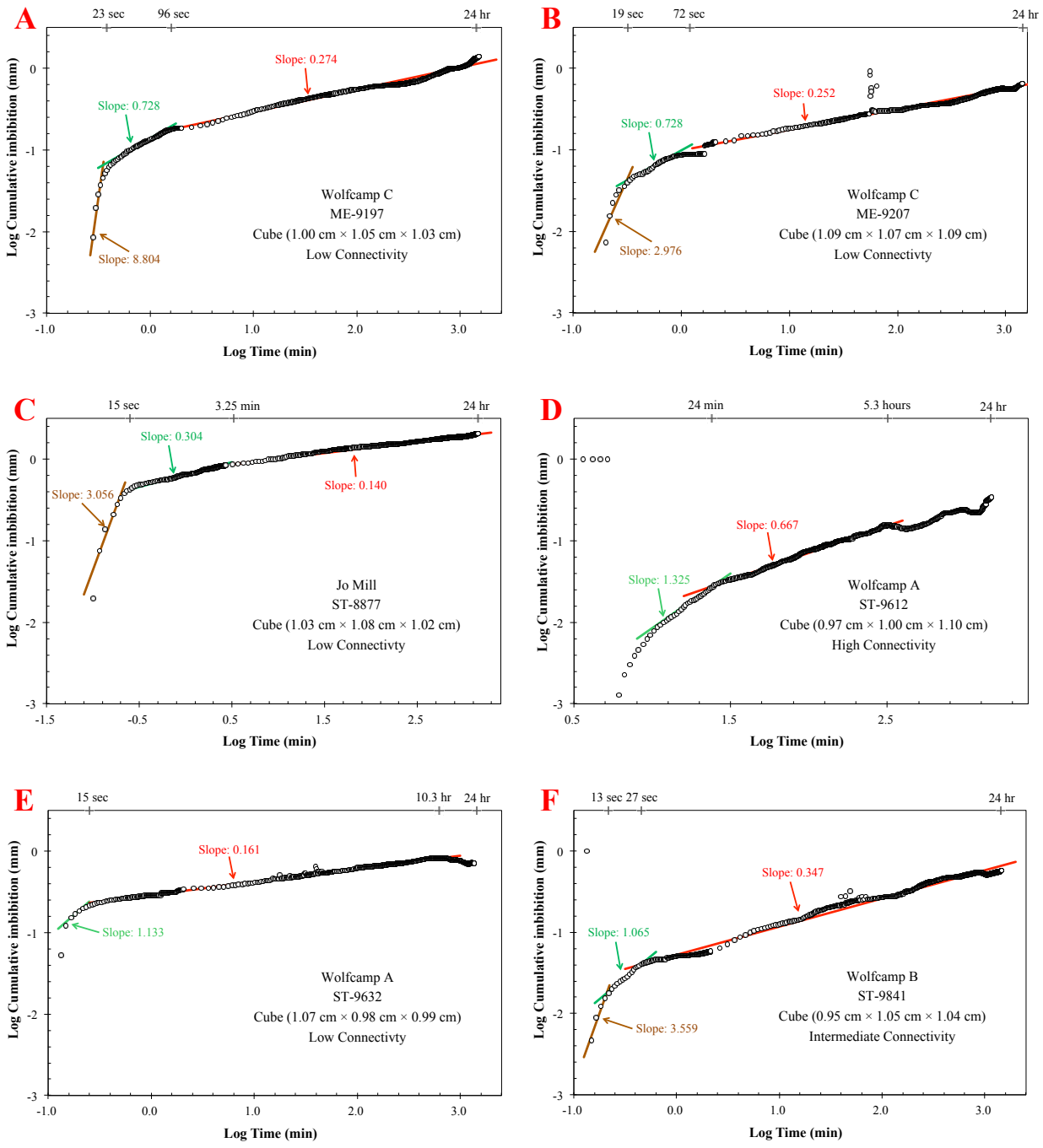

Figure 4-12: DI Water imbibition slopes for ME-9197 (A), ME-9207 (B), ST-8877 (C), ST-9612 (D), ST-9632 (E), and ST-9841 (F).

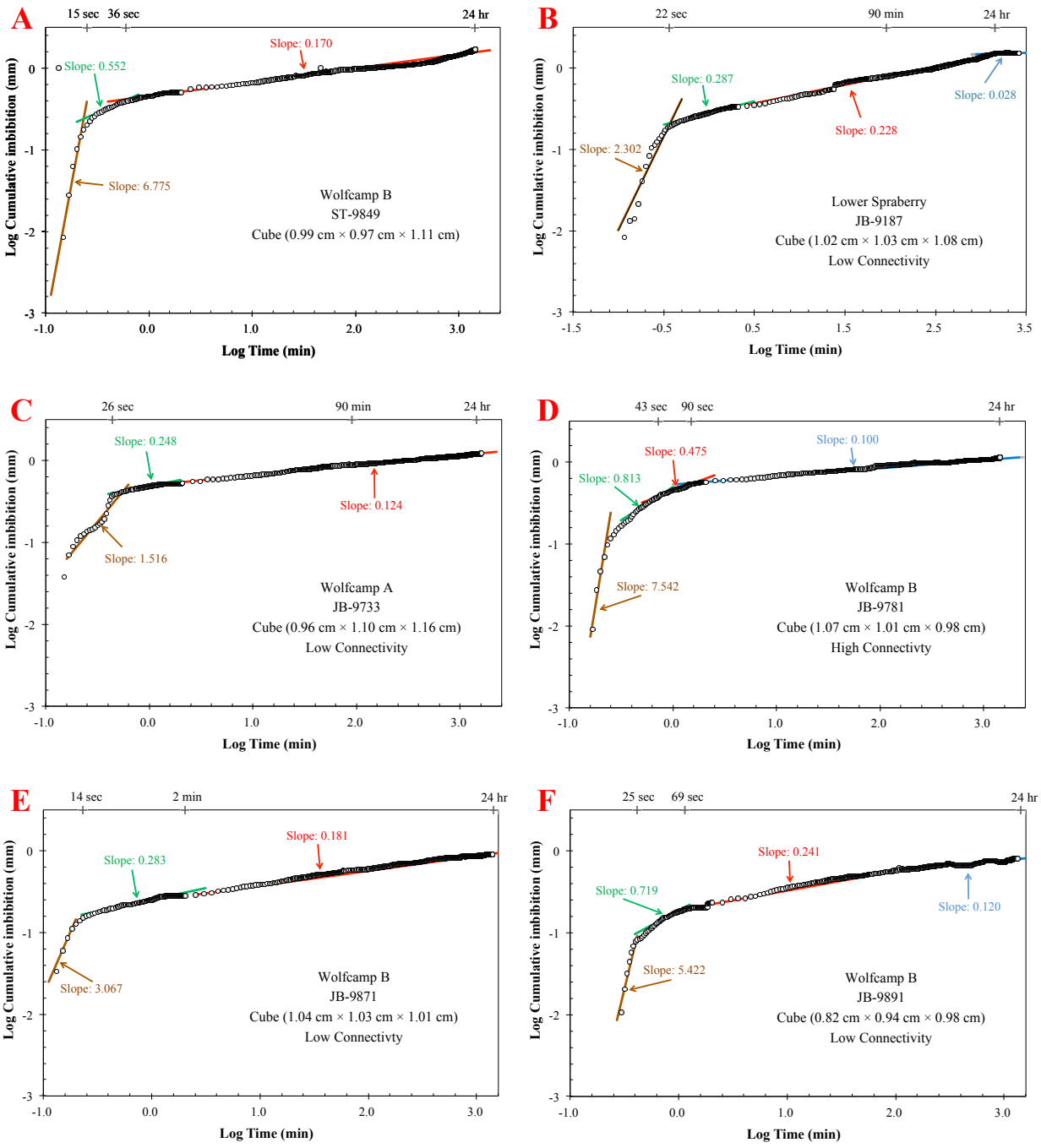

Figure 4-13: DI Water imbibition slopes for ST-9849 (A), JB-9187 (B), JB-9733 (C), JB-9781 (D), JB-9871 (E), and JB-9891 (F).

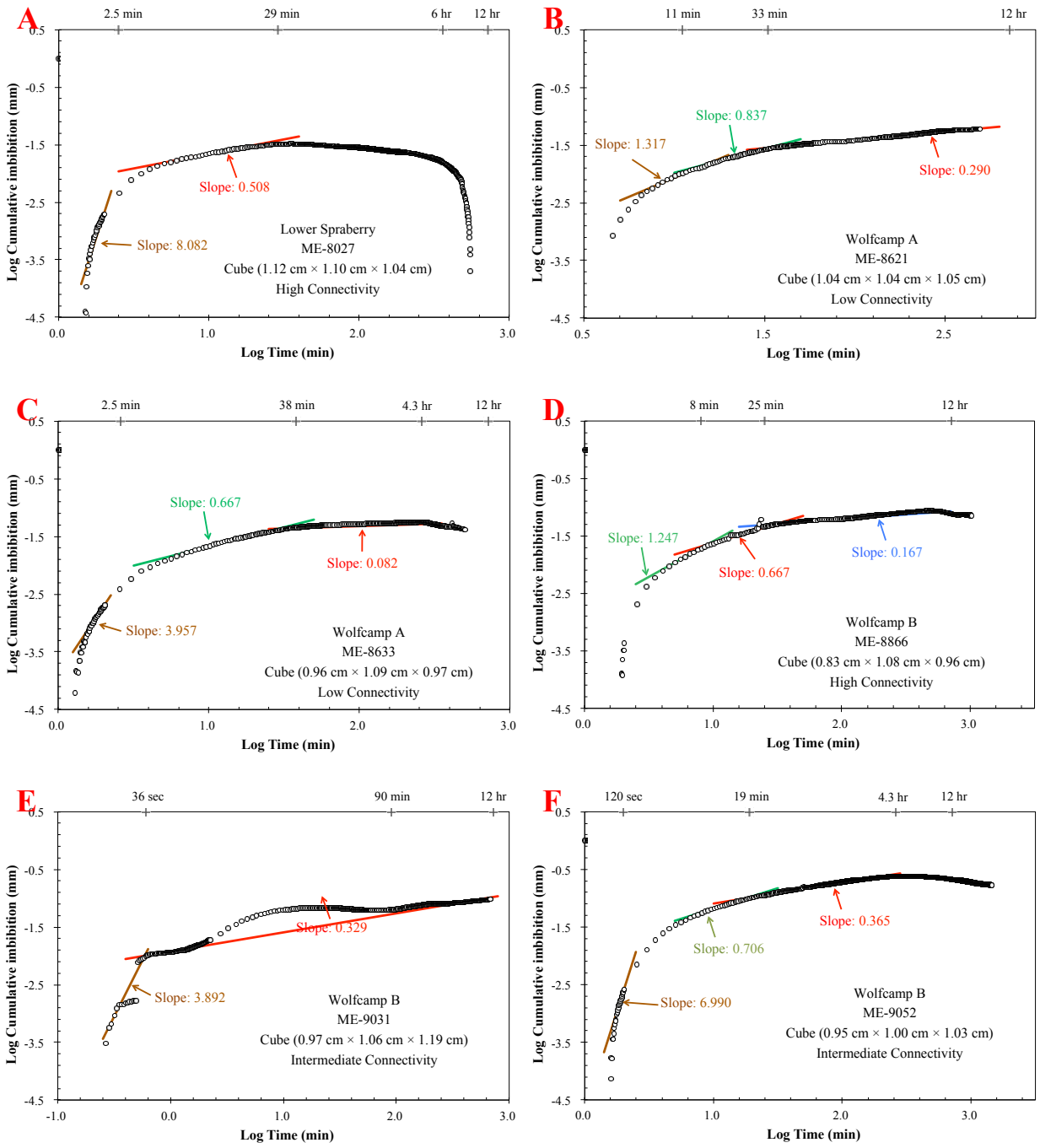

Figure 4-14: DT2 imbibition slopes for ME-8027 (A), ME-8621 (B), ME-8633 (C), ME-8866 (D), ME-9031 (E), and ME-9052 (F).

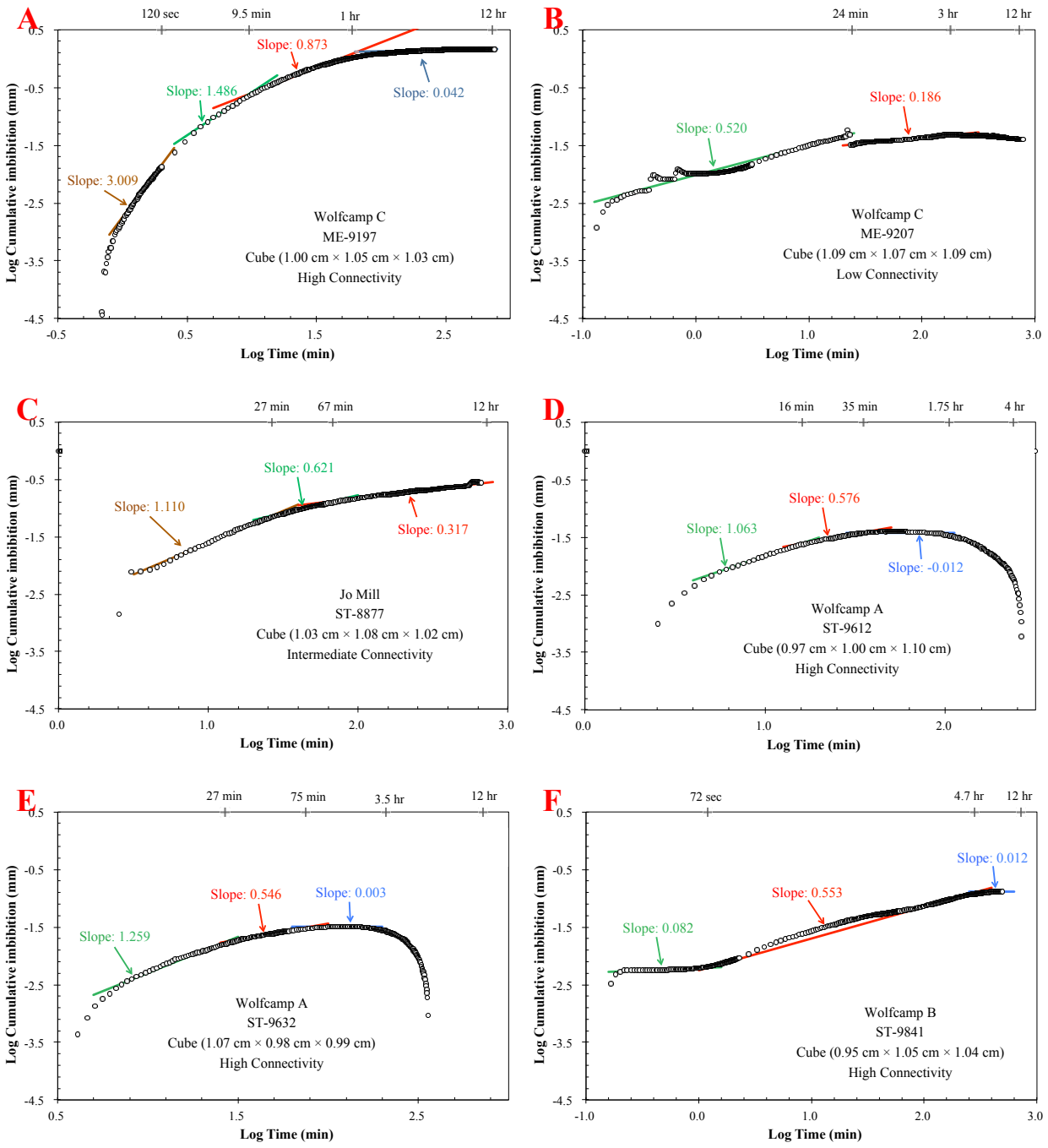

Figure 4-15: DT2 imbibition slopes for ME-9197 (A), ME-9207 (B), ST-8877 (C), ST-9612 (D), ST-9632 (E), and ST-9841 (F).

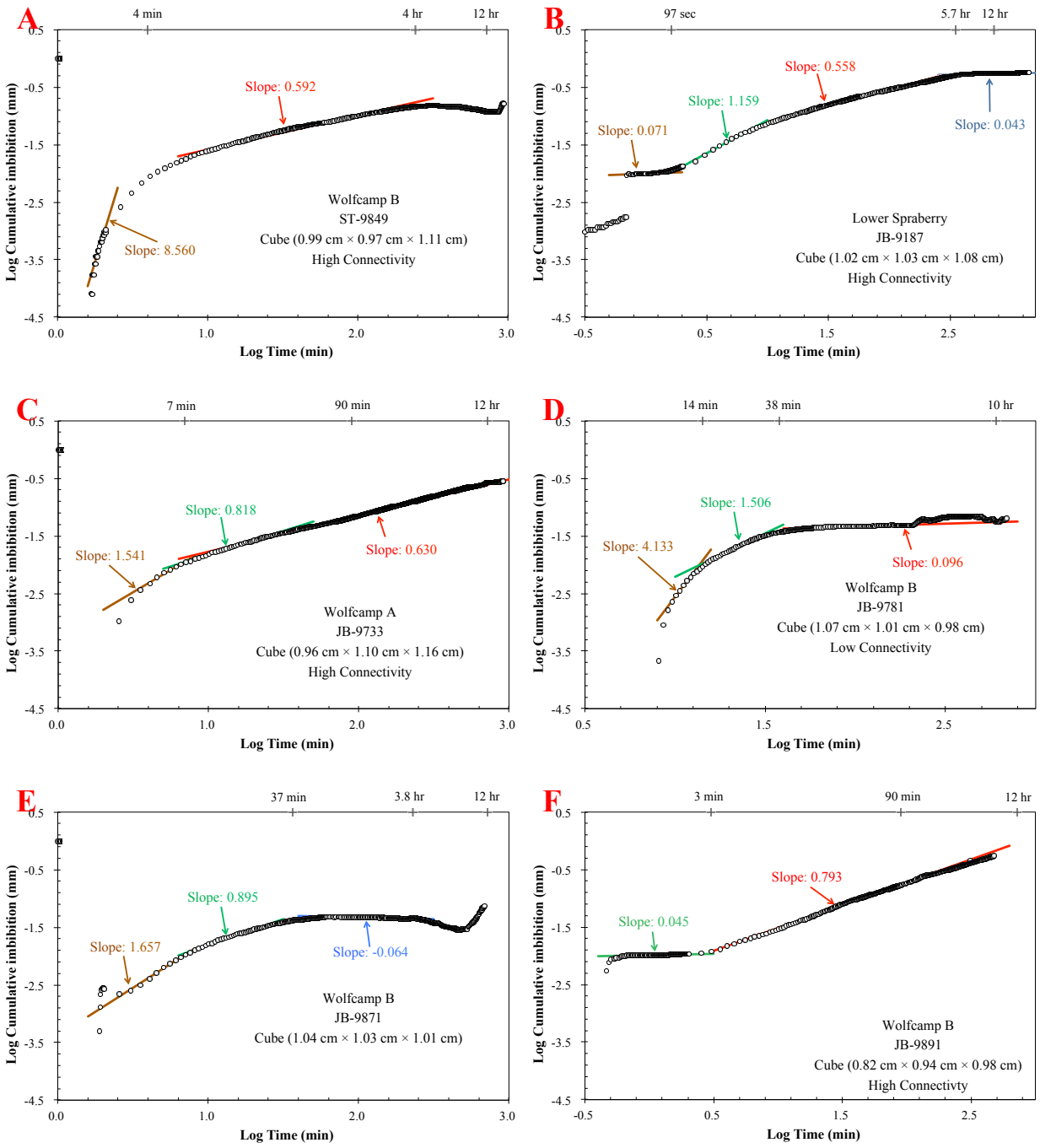

Figure 4-16: DT2 slopes for ST-9849 (A), JB-9187 (B), JB-9733 (C), JB-9781 (D), JB-9871 (E), and JB-9891 (F).

4-6 Mercury Intrusion Porosimetry (MIP)

Pore structure data measured directly, or calculated, from MIP test results on cube-sized samples are shown in Tables 4-6 and 4-7. Direct measurements from MIP tests are total pore

area, bulk density, apparent grain density, porosity, and pore throat diameter. Calculated values are determined by processing data using the Katz and Thompson (1986; 1987) equation for permeability and Hager (1998) approach for tortuosity. When processing data, inflection points or peaks are chosen on a plot of log differential intrusion vs. the intrusion pressure (Figures 4-18 to 22). Inflection points represent a pressure increase when mercury intruding pore throats exceeds capillary pressure of that specific pore network resulting in a peak in intrusion volume at specific pressure. For each connected pore network, there is a set of pore structure parameters such as porosity, pore-throat size, permeability and tortuosity. The main inflection point for each sample is used to determine permeability and tortuosity of the sample, where all inflection points for each sample are used in the modified Washburn equation to determine pore-throat size distribution. To better understand pore-throat size distribution for each sample, pore throats were divided into ranges based on correlated pressure ranges. These ranges represent predominant pore systems and are listed below (Hu et al., 2017).

- 1 - 1000 μm micro-fractures and lamination
- 0.05 - 1 μm intergranular pores
- 0.01 - 0.05 μm intragranular pores
- 0.005 - 0.01 μm organic matter-hosted pores
- 0.0028 - 0.005 μm inter-clay platelet pores

Pore-throat size distributions are listed in Table 4-7 and shown graphically in Figure 4-17.

Bulk density and grain density vary from sample to sample, but have similar values when porosity is lower, and larger values when porosity is higher. Porosity values differ throughout the samples tested, ST-9849 has the highest porosity at 10.2% and ME-8866 has the lowest porosity at 0.04%. For cube samples, porosity values established from MIP are almost all within 1.5%

porosity units of those determined from FIP. A few exceptions include ME-9052, ME-9197, and ST-9849, which have higher porosities reported from MIP testing. As expected, permeability is related to porosity, as illustrated by sample ST-9849 having the highest permeability at 3813.30 mD and ME-8633 having the lowest at 4.96E-7 mD. Tortuosity values vary across samples, where ME-8866 has the lowest at 0.04 and ME-9197 has the highest at 107.93.

Pore-throat size distribution is best shown graphically by Figure 4-17, where a darker shade of red represents larger pore throats. JB-9891 is a clear example of a sample dominated by macropores, which are pores greater than 100 nm in size and JB-9781 is a good representation of a sample dominated by micropores, which are pores less than 50 nm in size (Tonietto et al., 2014). Variations in pore-throat size are expected based on variety of sample compositions chosen for this study.

Samples ME-9052 and ST-9849 display abnormally large spikes in intrusion volume at lower pressures, which were interpreted as mercury invading fractures. These spikes indicating fractures were noted, but omitted when determining rock property values due to them skewing the data. Ideally, by eliminating fracture related spikes, data should more closely represent rock matrix pore space. The MIP data for a single sample with a fracture was processed including and excluding the fracture.

Table 4-6: MIP results summary.

Sample ID	**Total Intrusion Volume** at ~60,000 psi (mL/g)	**Total Pore Area** at ~60,000 psi (m^2/g)	**Bulk Density** at Filling Pressure (g/cm^3)	**Grain/Skeletal Density** at ~60,000 psi (g/cm^3)	**Porosity** (%)	**Permeability** (mD)	**Geometrical Tortuosity** (L_e/L)
ME-8027	0.000	0.001	2.669	2.672	0.113	0.07	0.09
ME-8621	0.003	0.940	2.576	2.594	0.700	0.71	0.23
ME-8633	0.002	0.776	2.522	2.533	0.440	4.96E-7	3.81
ME-8866	0.000	0.000	2.510	2.511	0.038	0.31	0.04
ME-9031	0.006	0.740	2.582	2.621	1.470	7.29E-5	2.21
ME-9052	0.035	0.361	2.448	2.676	8.530	1.18	3.46
ME-9197	0.026	3.253	2.268	2.409	5.846	6.68E-6	108
ST-8877	0.014	3.145	2.554	2.647	3.507	7.50E-5	24.3
ST-9612	0.002	0.785	2.617	2.633	0.629	1.02E-6	3.85
ST-9632	0.001	0.001	2.618	2.621	0.146	0.19	0.08
ST-9841	0.032	0.796	2.434	2.639	7.747	0.52	4.36
ST-9849	0.045	3.172	2.252	2.508	10.205	3813	0.21
JB-9187	0.020	5.638	2.462	2.592	5.022	6.19E-5	30.3
JB-9733	0.004	2.865	2.534	2.562	1.089	1.90E-6	5.64
JB-9781	0.008	4.757	2.380	2.427	1.946	1.83E-6	8.74
JB-9871	0.001	0.014	2.654	2.659	0.165	0.04	0.15
JB-9891	0.001	0.092	2.613	2.618	0.167	0.28	0.10

Table 4-7: Pore-throat size distribution results (%) from MIP analyses.

Sample ID	Pore Throat Size Ranges (μm)						
	> 10	10 - 1	1 - 0.1	0.1 - 0.05	0.05 - 0.01	0.01 - 0.005	0.005 - 0.0028
ME-8027	14.2	68.6	17.2	-	-	-	-
ME-8621	31.6	12.3	7.2	4.2	13.9	10.8	20.0
ME-8633	6.0	20.5	11.8	5.4	13.2	21.0	22.2
ME-8866	79.3	20.7	-	-	-	-	-
ME-9031	2.7	7.0	10.6	20.3	59.3	0.2	-
ME-9052	30.3	16.4	51.6	1.7	0.1	-	-
ME-9197	82.5	0.4	1.0	0.6	3.6	5.5	6.5
ST-8877	16.0	2.3	2.0	11.5	57.6	4.9	5.8
ST-9612	4.9	15.1	14.9	6.3	23.9	33.2	1.8
ST-9632	22.8	53.8	8.3	-	-	-	15.1
ST-9841	15.4	15.0	57.4	6.7	5.5	-	-
ST-9849	89.0	1.0	0.9	0.3	1.9	3.2	3.5
JB-9187	13.1	2.8	2.6	5.1	61.2	10.6	4.6
JB-9733	7.2	0.8	0.0	0.0	19.7	50.2	22.1
JB-9781	7.1	6.1	5.1	3.9	22.8	27.1	27.9
JB-9871	26.6	21.3	35.0	13.6	3.6	-	-
JB-9891	35.6	39.9	11.0	2.1	1.0	-	10.5

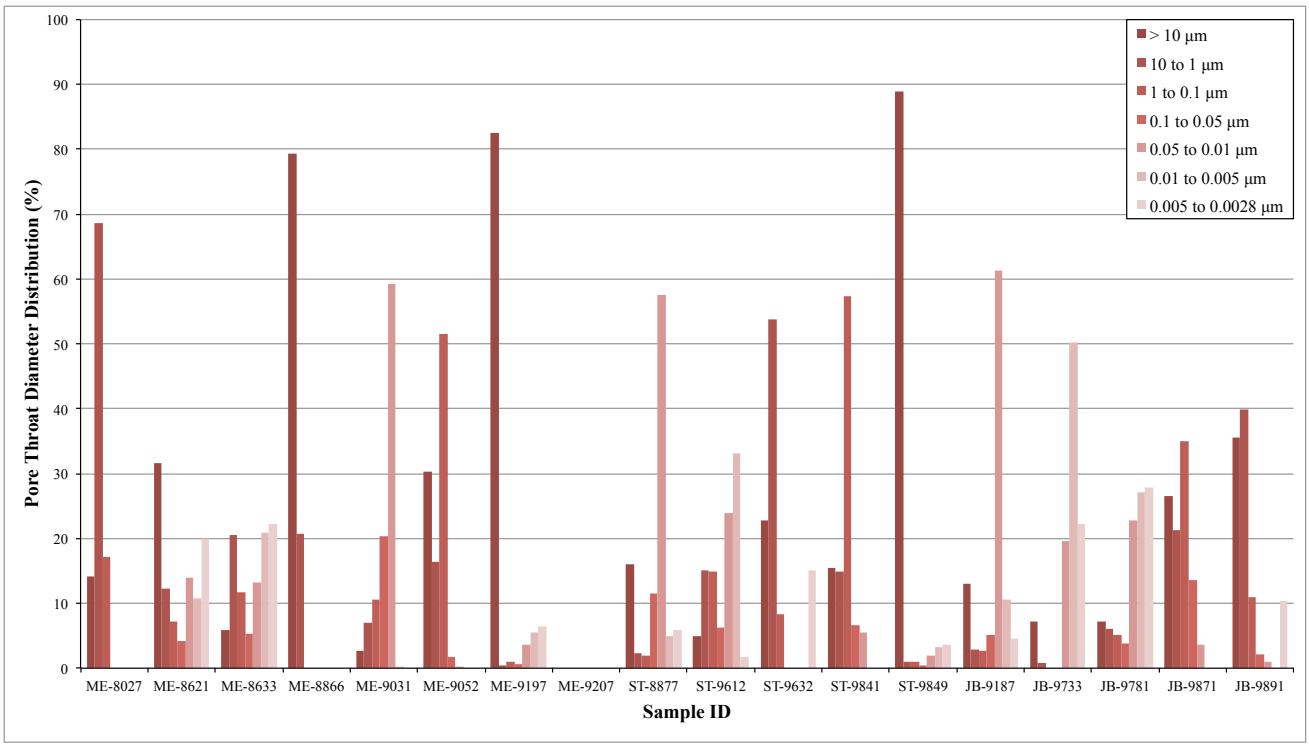

Figure 4-17: Graphical representation of pore-throat size distribution from MIP analyses.

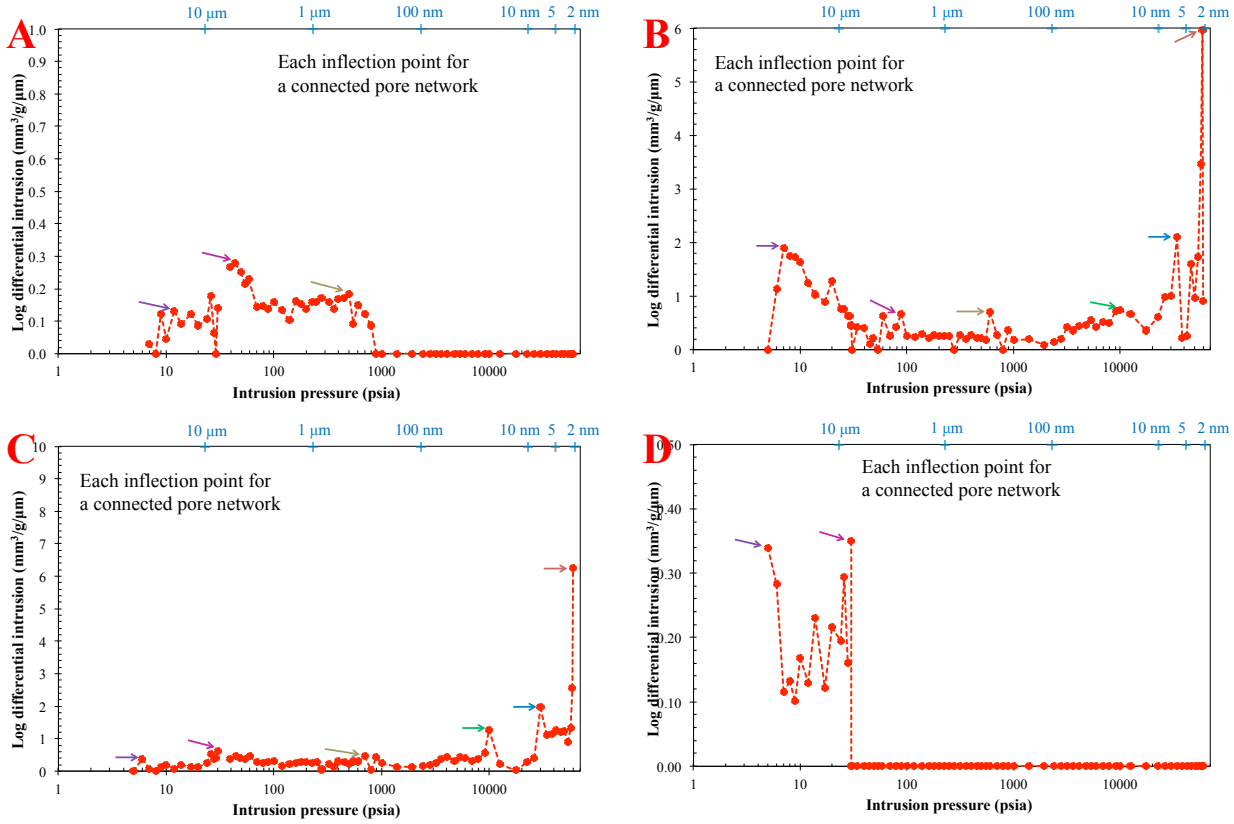

Figure 4-18: MIP intrusion results showing inflection points with colored arrows for each pore-size range for ME-8027 (A), ME-8621 (B), ME-8633 (C), and ME-8866 (D); the 2nd X-axis indicates the pore-throat size corresponding to the intrusion pressure of X-axis.

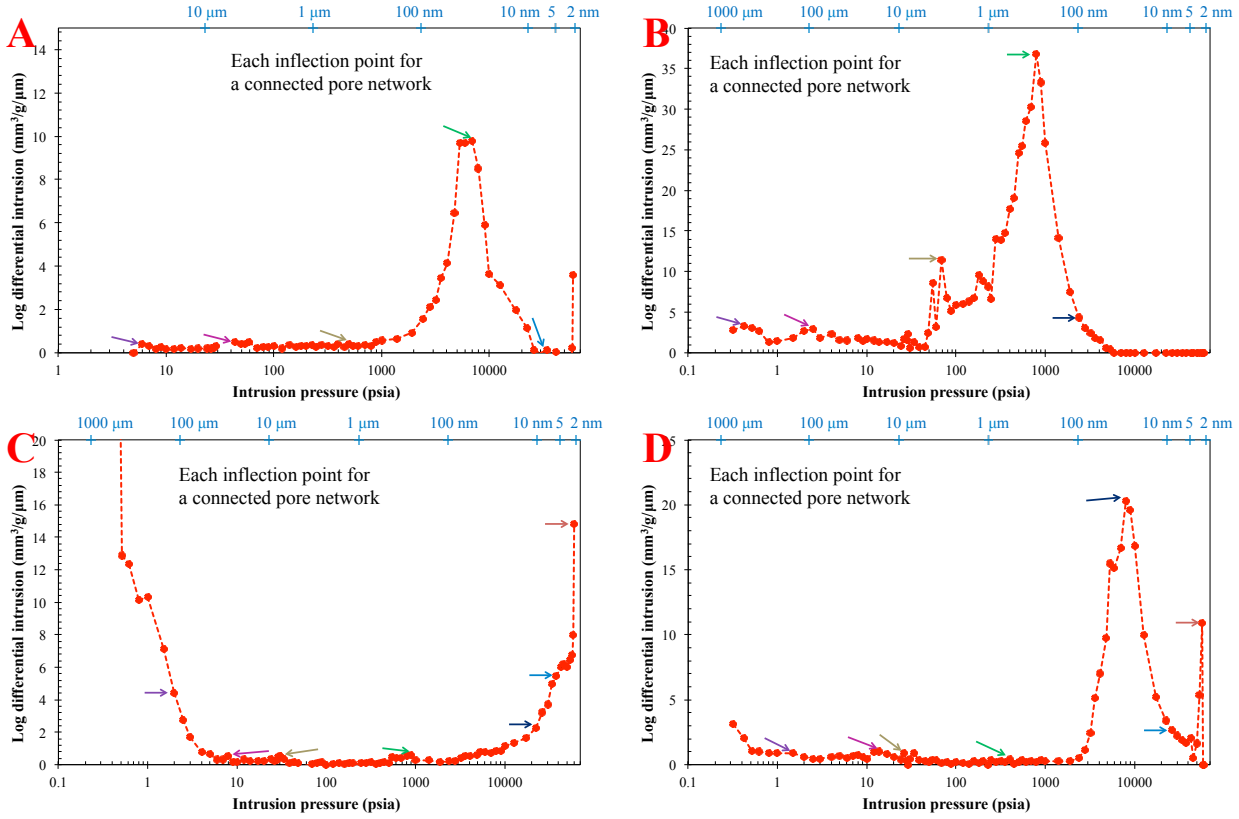

Figure 4-19: MIP intrusion results showing inflection points with colored arrows for each pore-size range for ME-9031 (A), ME-9052 (B), ME-9197 (C), and ST-8877 (D); the 2nd X-axis indicates the pore-throat size corresponding to the intrusion pressure of X-axis.

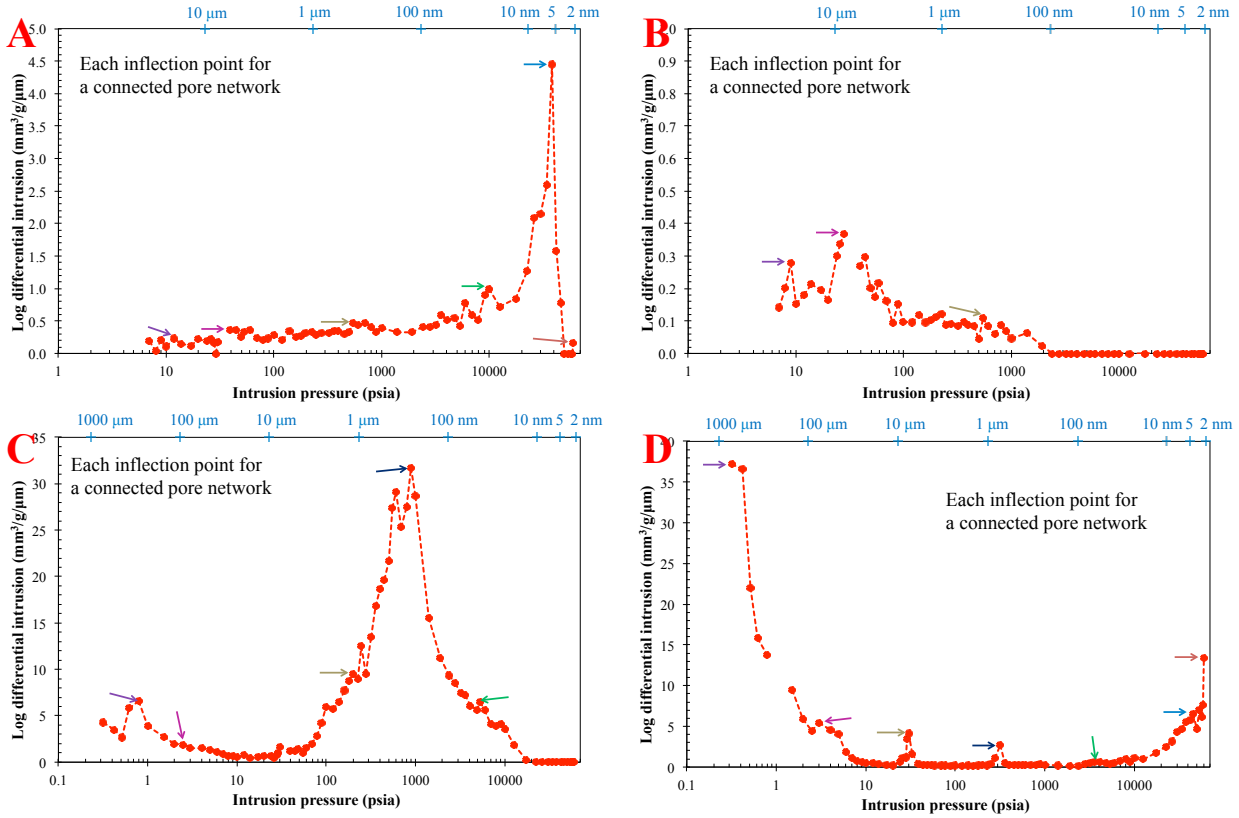

Figure 4-20: MIP intrusion results showing inflection points with colored arrows for each pore-size range for ST-9612 (A), ST-9632 (B), ST-9841 (C), and ST-9849 (D); the 2nd X-axis indicates the pore-throat size corresponding to the intrusion pressure of X-axis.

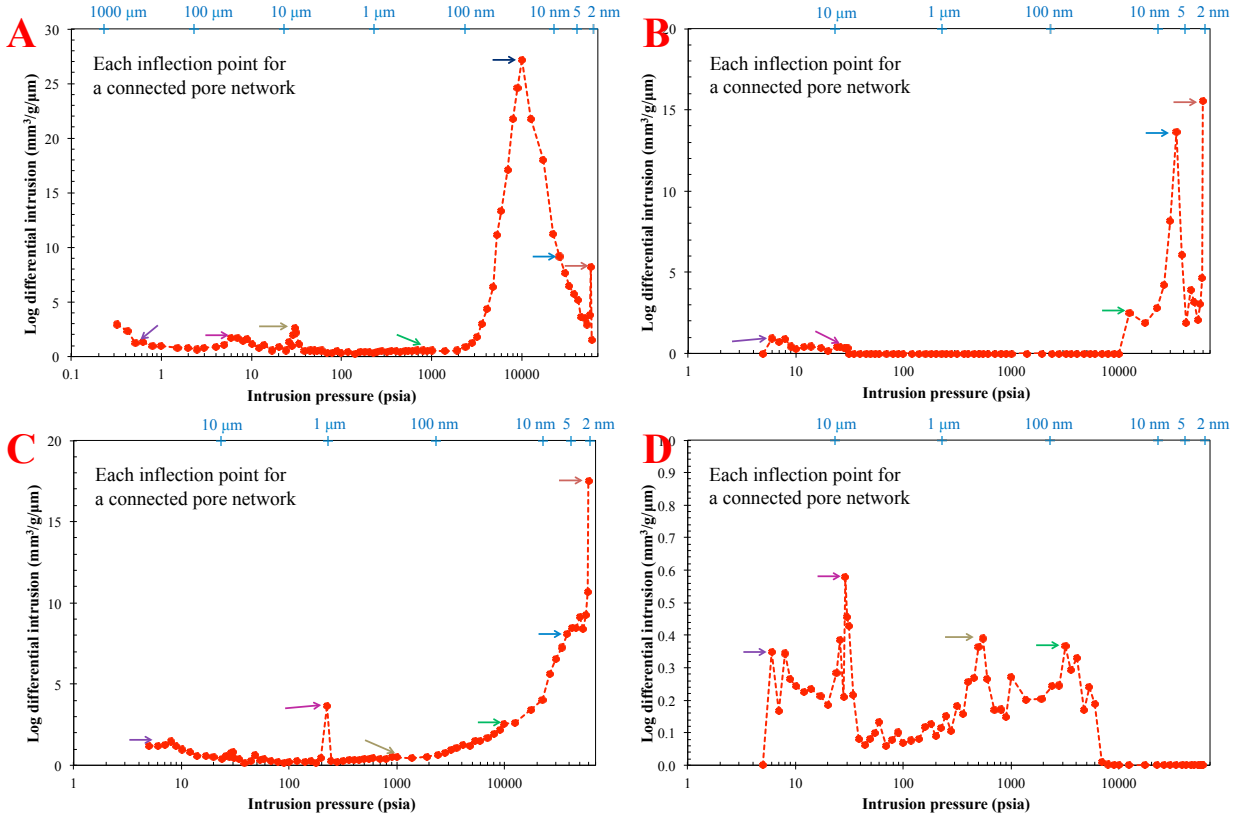

Figure 4-21: MIP intrusion results showing inflection points with colored arrows for each pore-size range for JB-9187 (A), JB-9733 (B), JB-9781 (C), and JB-9871 (D); the 2nd X-axis indicates the pore-throat size corresponding to the intrusion pressure of X-axis.

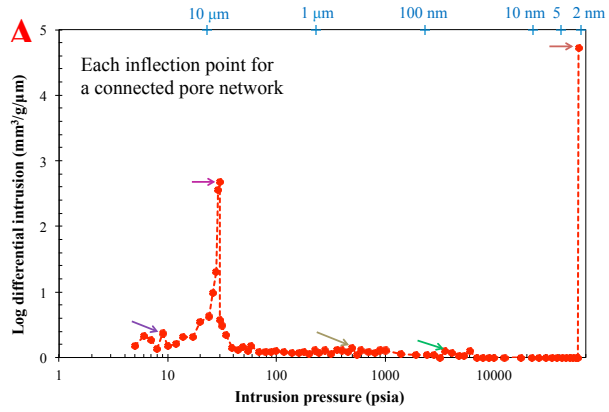

Figure 4-22: MIP intrusion results showing inflection points with colored arrows for each pore-size range for JB-9891 (A); the 2nd X-axis indicates the pore-throat size corresponding to the intrusion pressure of X-axis.

4-7 Contact Angle

Contact angle and wettability classification for samples tested is listed on Table 4-8.

Contact angles are reported as an average of left and right angles of droplets 30 seconds after the

droplet first makes contact with sample surface for each fluid except DT2. Due to a high rate of spreading of DT2 on our as-received samples, contact angles used are from less than one second after the droplet makes contact with sample surface. Images for ME-9197 at the 30 second point for DI water, API brine, 20% THF or 20% IPA, and the < 1 second point for DT2 are displayed in Figure 4-24. Angle measurements are recorded at incremental time intervals during testing duration, and data is displayed graphically for ME-9197 in Figure 4-23 (as an example) illustrating angle of each fluid droplet, against the sample surface, over time. The results in Table 4-8 indicate samples are largely intermediate to oil-wet, with the exception of ST-8877 being water-wet.

Table 4-8: Contact angle results (in degrees); 3 degrees for DT2 tests is the detection limit.

Sample ID	DI Water	API Brine	20% IPA	20% THF	DT2	Wettability Classification
ME-8027	48.7	66.2	43.6	48.1	13.4 to 3.0	Partial water-wet; Completely oil-wet
ME-8621	45.1	56.5	-	44.8	14.8 to 3.0	Partial oil-wet
ME-8633	67.6	67.6	-	52	14.8 to 3.0	Oil-wet
ME-8866	61	62.4	-	38.1	24.7 to 3.0	Oil-wet
ME-9031	35.2	-	-	-	11.0 to 3.0	Intermediate
ME-9052	68.4	87.2	53.9	50.5	-	Oil-wet
ME-9197	55.5	58.6	37.1	19.9	13.3 to 3.0	Oil-wet
ME-9207	60.2	69.5	-	39.1	18.6 to 3.0	Oil-wet
ST-8877	26	36.3	30.7	49.5	5.2 to 3.0	Water-wet
ST-9612	41.8	89.7	51.7	45.2	14.4 to 3.0	Oil-wet
ST-9632	68.7	43.3	61.8	49.8	15.3 to 3.0	Intermediate
ST-9841	72.5	81.6	47.9	50.1	17. to 3.0	Oil-wet
ST-9849	37.5	64.5	35.9	30	15.5 to 3.0	Oil-wet
JB-9733	53.4	-	-	-	-	Intermediate
JB-9781	42.3	49.7	-	43.6	13.4 to 3.0	Intermediate
JB-9871	53.2	72.4	-	57.6	15.0 to 3.0	Oil-wet
JB-9891	42.4	45.1	-	46.8	12.6 to 3.0	Intermediate

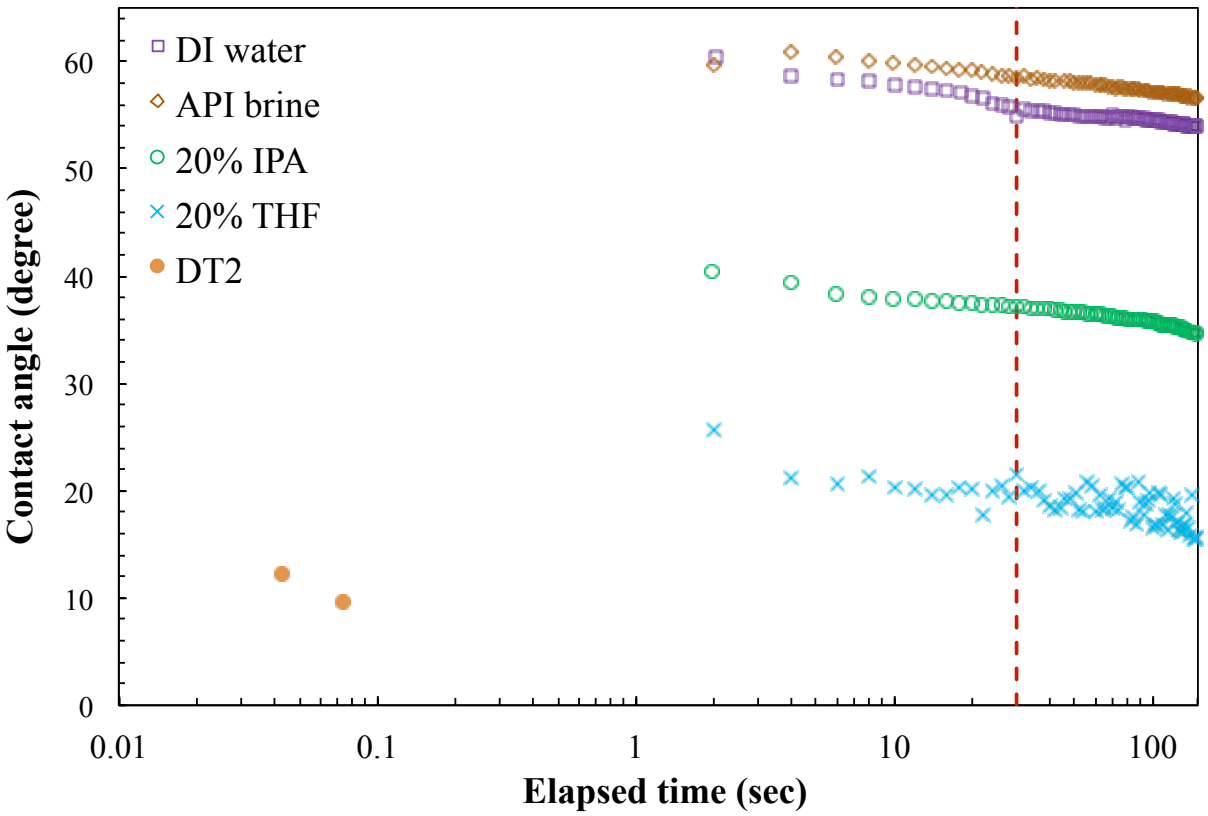

Figure 4-23: Contact angle results for ME-9197 in log time. Red dashed line marks the 30 second point where droplet angle results where recorded.

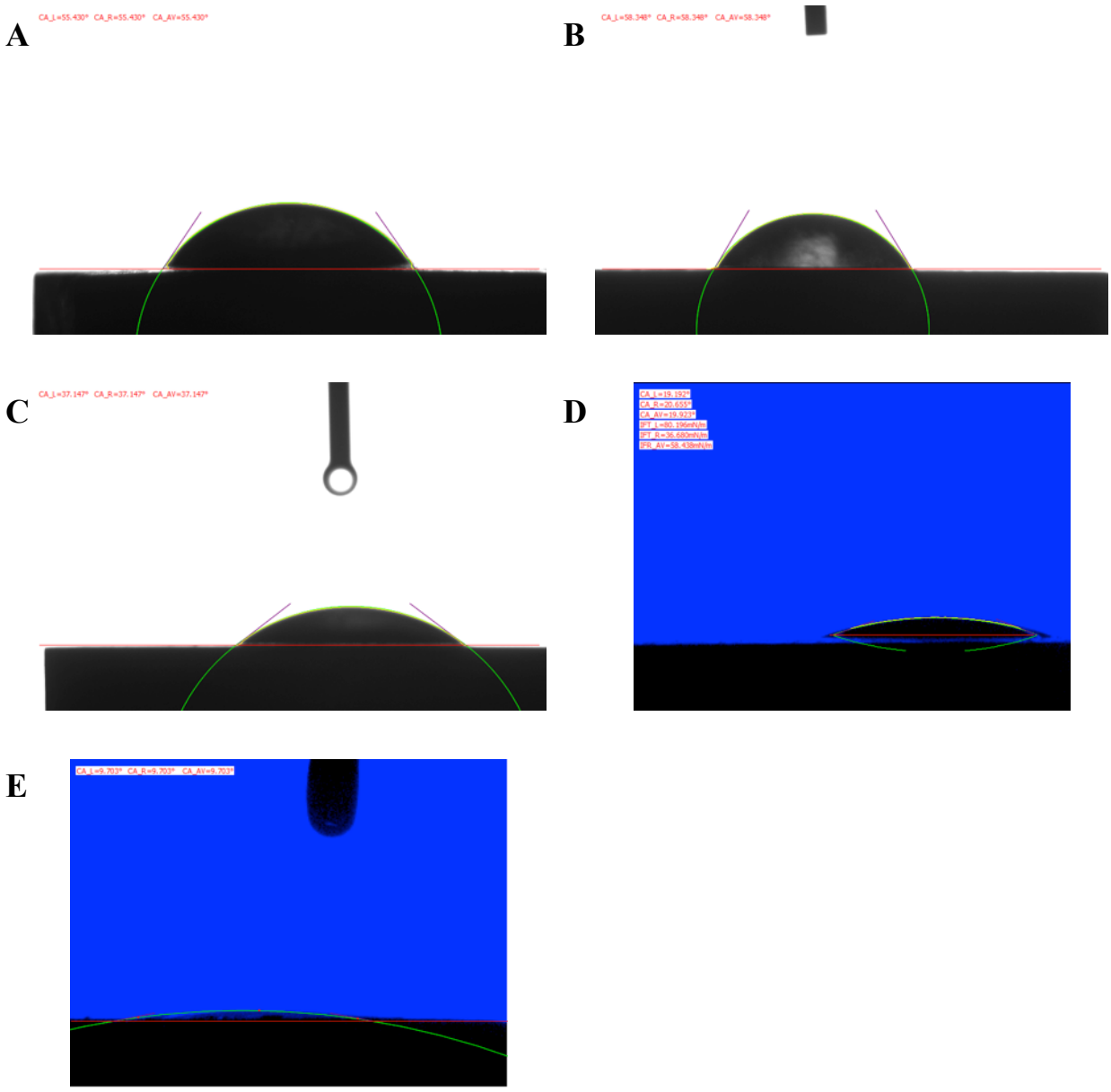

Figure 4-24: Images showing droplet and contact angle on ME-9197 sample surface after 30 seconds in fluid DI water (A), API Brine (B), 20% IPA (C), 20% THF (D), and DT2 (E).

4-8 Well Log Analysis

Formation tops, core data points, and well logs for the sampled wells are displayed in Figure 4-25 through Figure 4-27. Well log intervals shown encompass the core data points in order to make comparisons. Scales, symbology, and curve names are shown in log track headers. Well log curves presented to the left of the depth track are wireline measurements except total

porosity, and log curves presented to the right of the depth track are calculated except bulk density and core points. Formation top colors remain constant in all three wells and are labeled to the right of track 11.

Well log curves for each well are displayed in 11 tracks containing curves and core data points (Table 4-9). Core porosity and bulk density values are shown as single dots at their respective depths although multiple values may exist. MIP porosity and bulk density results were given display priority over other techniques, followed by vacuum-assisted FIP using DT2, followed by vacuum-assisted FIP using DI water; both MIP and FIP tests use 1-cm cubic samples. Total porosity in track three is an average of the neutron and density porosity, but total porosity in track nine takes into account the calculated kerogen and mineral volumes.

Table 4-9: Well log headers

Track 1	**Track 2**	**Track 3**	**Track 4**	**Track 5**	**Track 6**
Gamma Ray Caliper Photoelectric Factor	Deep Resistivity Shallow Resistivity	Sonic Porosity Density Porosity Neutron Porosity Total Porosity	Measured Depth	Core Porosity Corrected Porosity	Core Permeability Timur Permeability Estimation Water Saturation

Track 7	**Track 8**	**Track 9**	**Track 10**	**Track 11**
Core Bulk Density Bulk Density	Bulk Volume Water Clay Bound Water Bulk Volume Hydrocarbons	Core Carbonates Core Clays Core Quartz + Felds Volume Carbonate Volume Quartz Volume Clay Volume Kerogen Total Porosity Mineralogy	Core TOC Schmoker TOC Estimation	Shale Volume

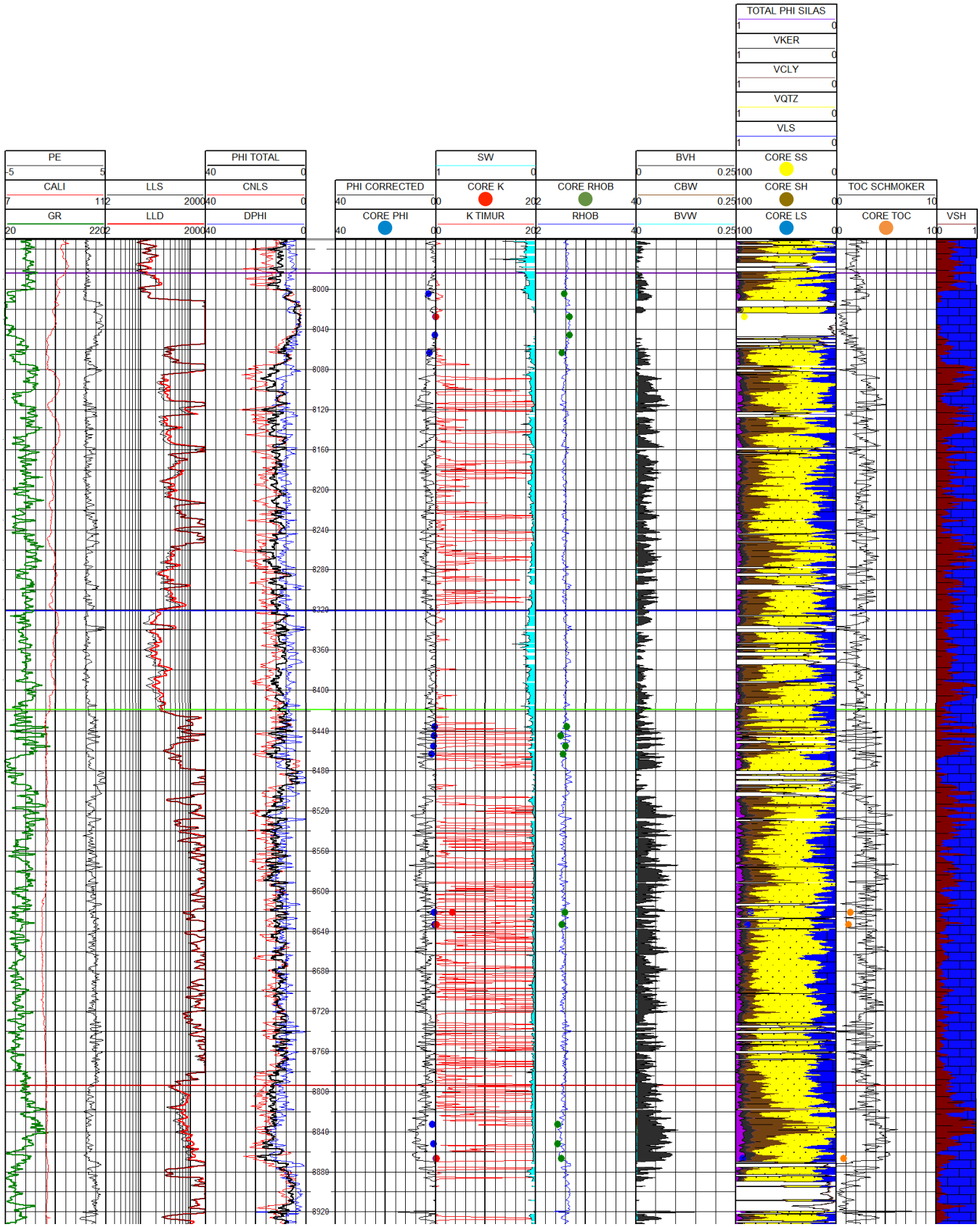
PE
-5
5
CALI
7
112
GR
20
220
LLS
200
LLD
200
PHI TOTAL
40
0
CNLS
40
0
DPHI
40
0
PHI CORRECTED
40
0
CORE PHI
40
0
SW
1
0
CORE K
0
202
K TIMUR
0
202
CORE RHOB
40
RHOB
40
BVH
0
0.25
CBW
40
0.25
BVW
40
0.25
TOTAL PHI SILAS
1
0
VKER
1
0
VCLY
1
0
VQTZ
1
0
VLS
1
0
CORE SS
100
0
CORE SH
100
0
CORE LS
100
0
TOC SCHMOKER
0
10
CORE TOC
0
100
VSH
1
8000
8040
8080
8120
8160
8200
8240
8280
8320
8360
8400
8440
8480
8520
8560
8600
8640
8680
8720
8760
8800
8840
8880
8920
Lower Spraberry
Dean
Wolfcamp A
Wolfcamp B

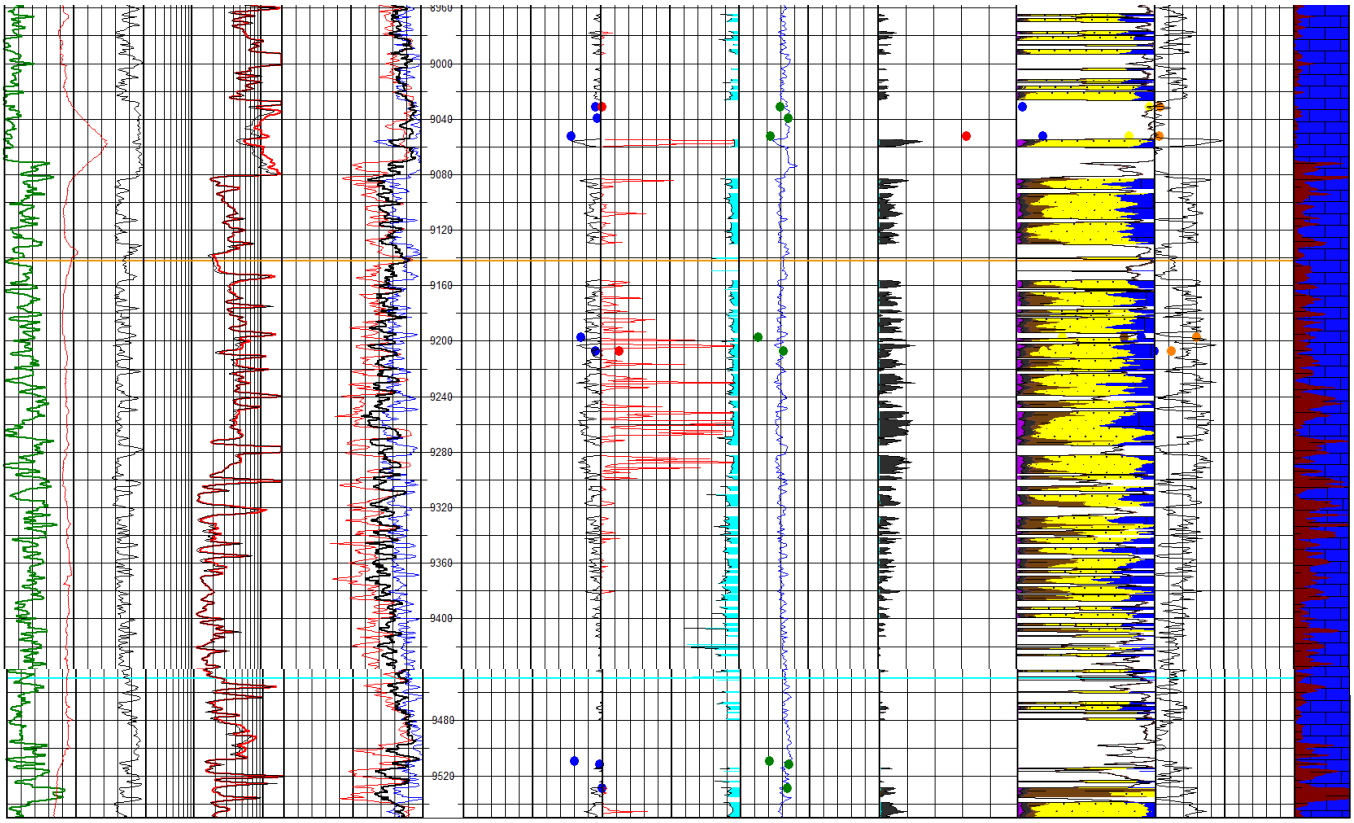

Figure 4-25: Mary Ellen #1 formation tops and well logs with core data points.

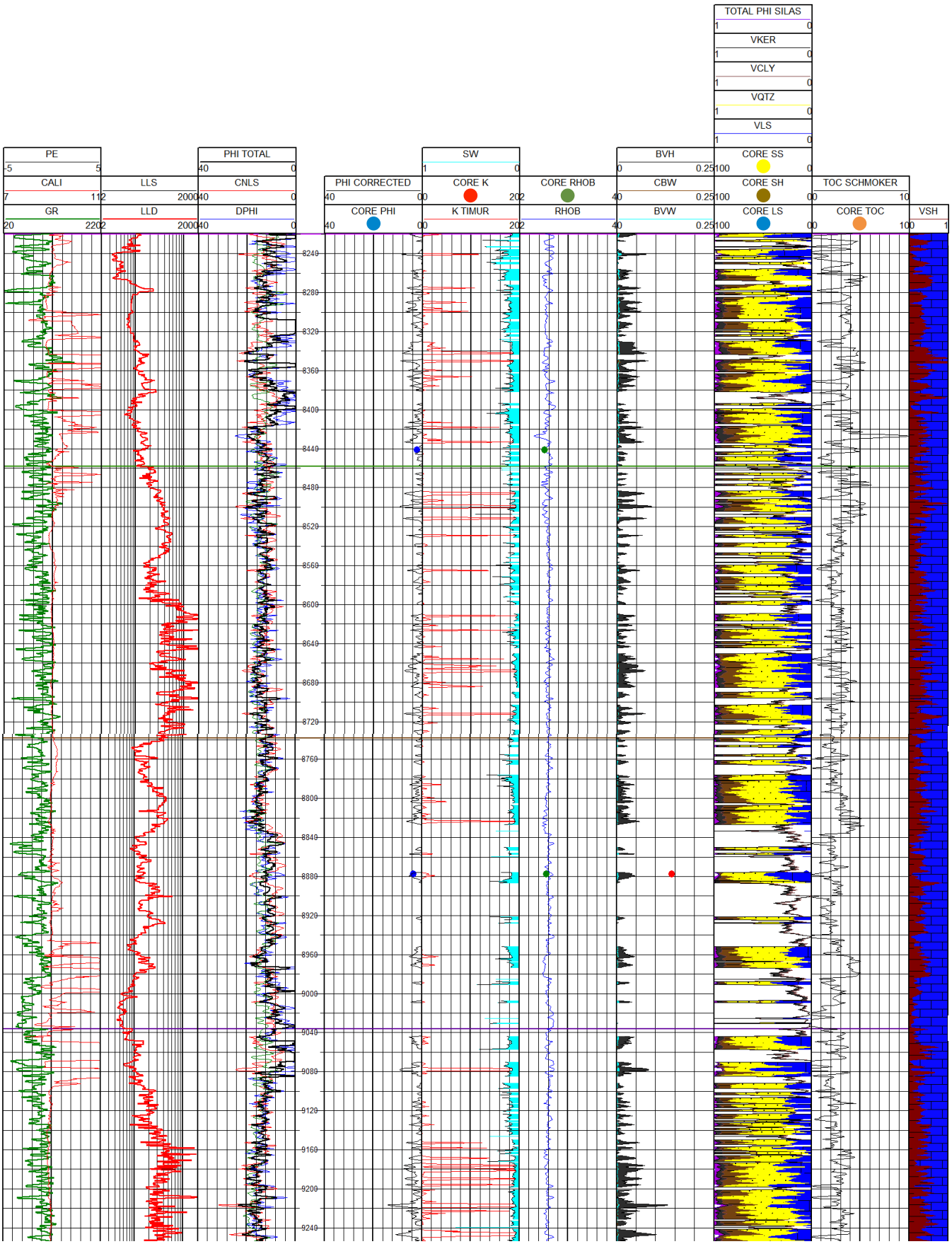
TOTAL PHI SILAS
VKER
VCLY
VQTZ
VLS
PE
PHI TOTAL
SW
BVH
CORE SS
CALI
LLS
CNLS
PHI CORRECTED
CORE K
CORE RHOB
CBW
CORE SH
TOC SCHMOKER
GR
LLD
DPHI
CORE PHI
K TIMUR
RHOB
BVW
CORE LS
CORE TOC
VSH
Spraberry
Middle Spraberry
Jo Mill
Lower Spraberry

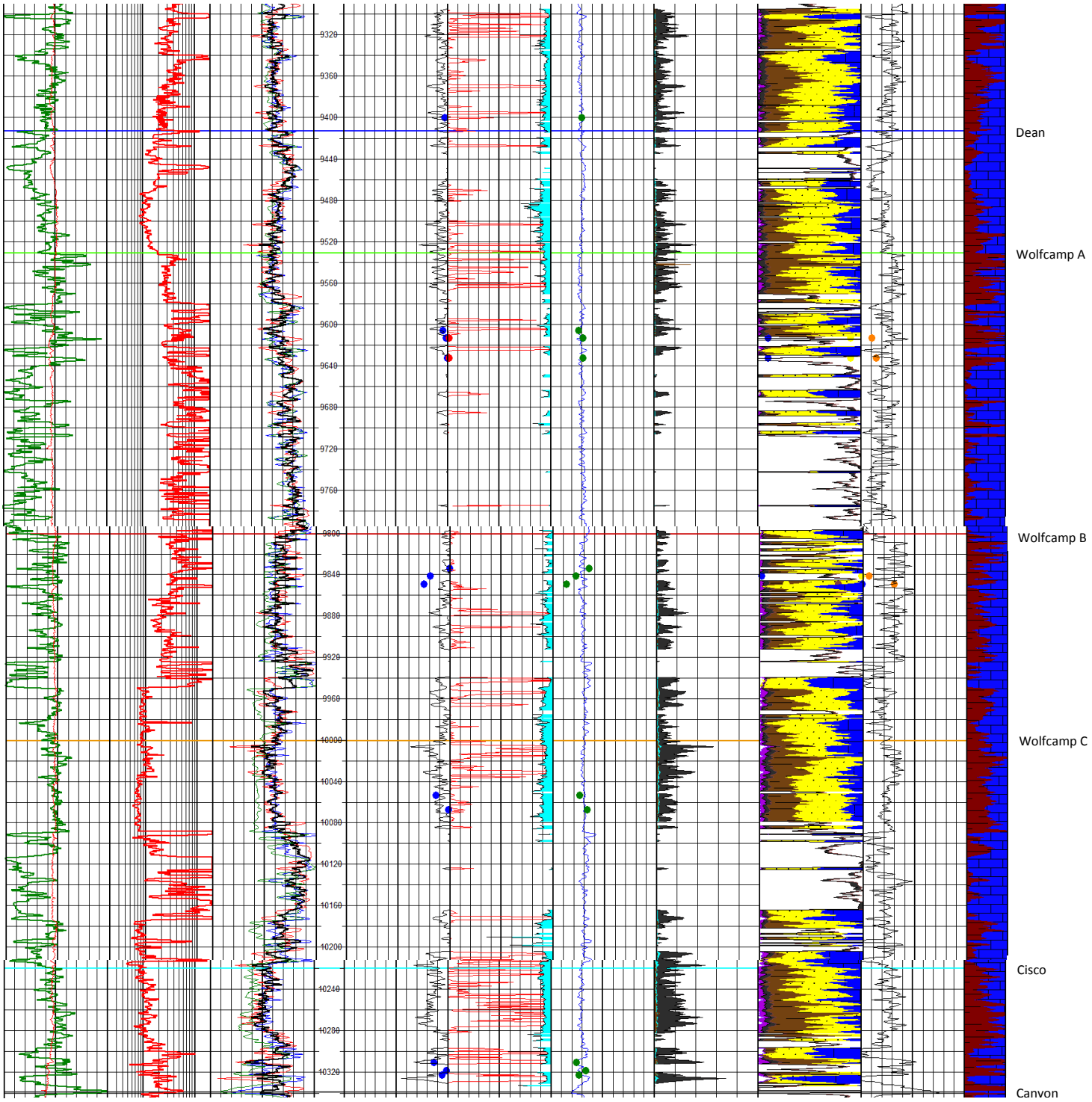

Figure 4-26: Spanish Trail #41-11 formation tops and well logs with core data points

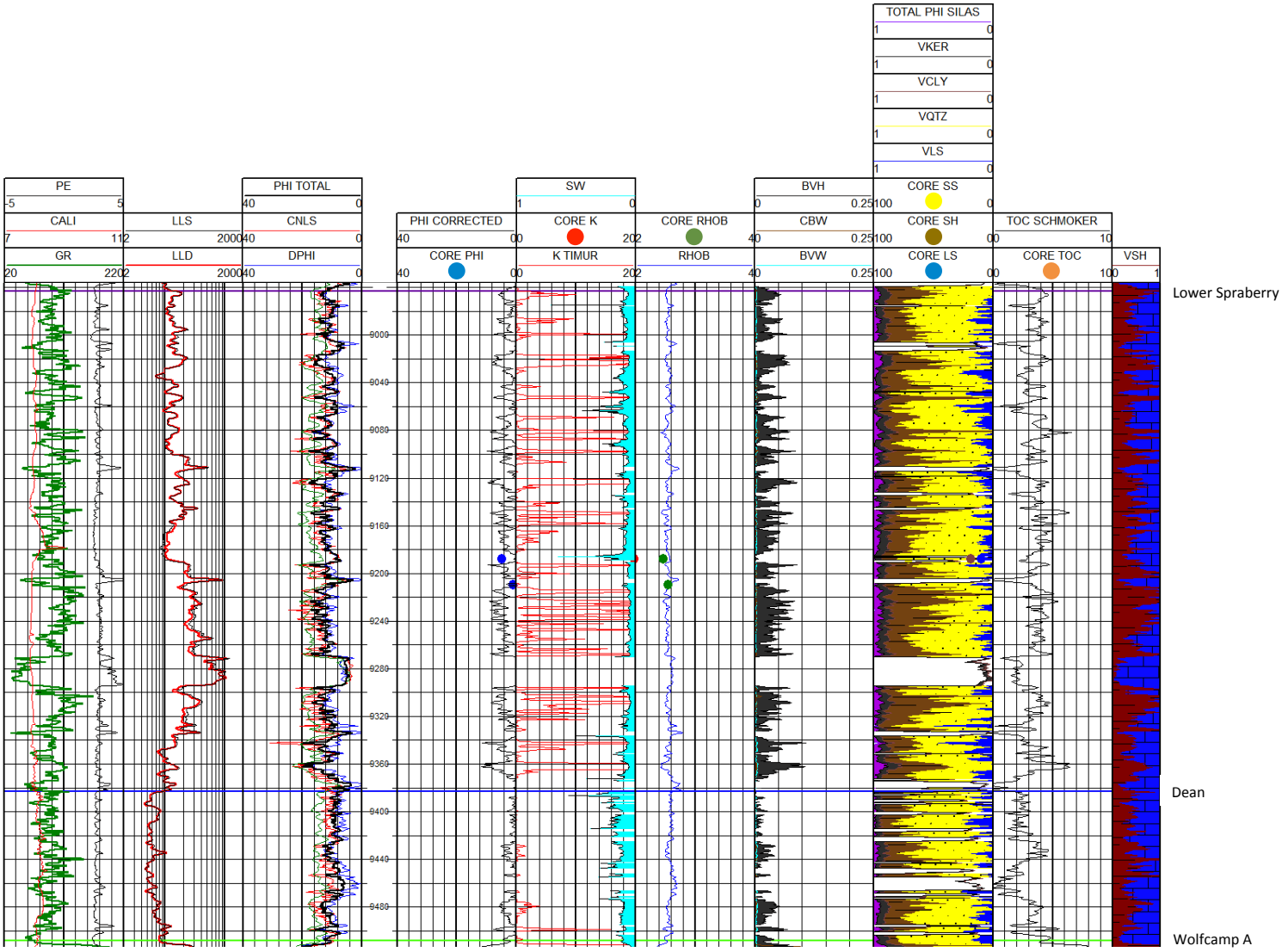
TOTAL PHI SILAS
VKER
VCLY
VQTZ
VLS
PE
PHI TOTAL
SW
BVH
CORE SS
CALI
LLS
CNLS
PHI CORRECTED
CORE K
CORE RHOB
CBW
CORE SH
TOC SCHMOKER
GR
LLD
DPHI
CORE PHI
K TIMUR
RHOB
BVW
CORE LS
CORE TOC
VSH
Lower Spraberry
Dean
Wolfcamp A

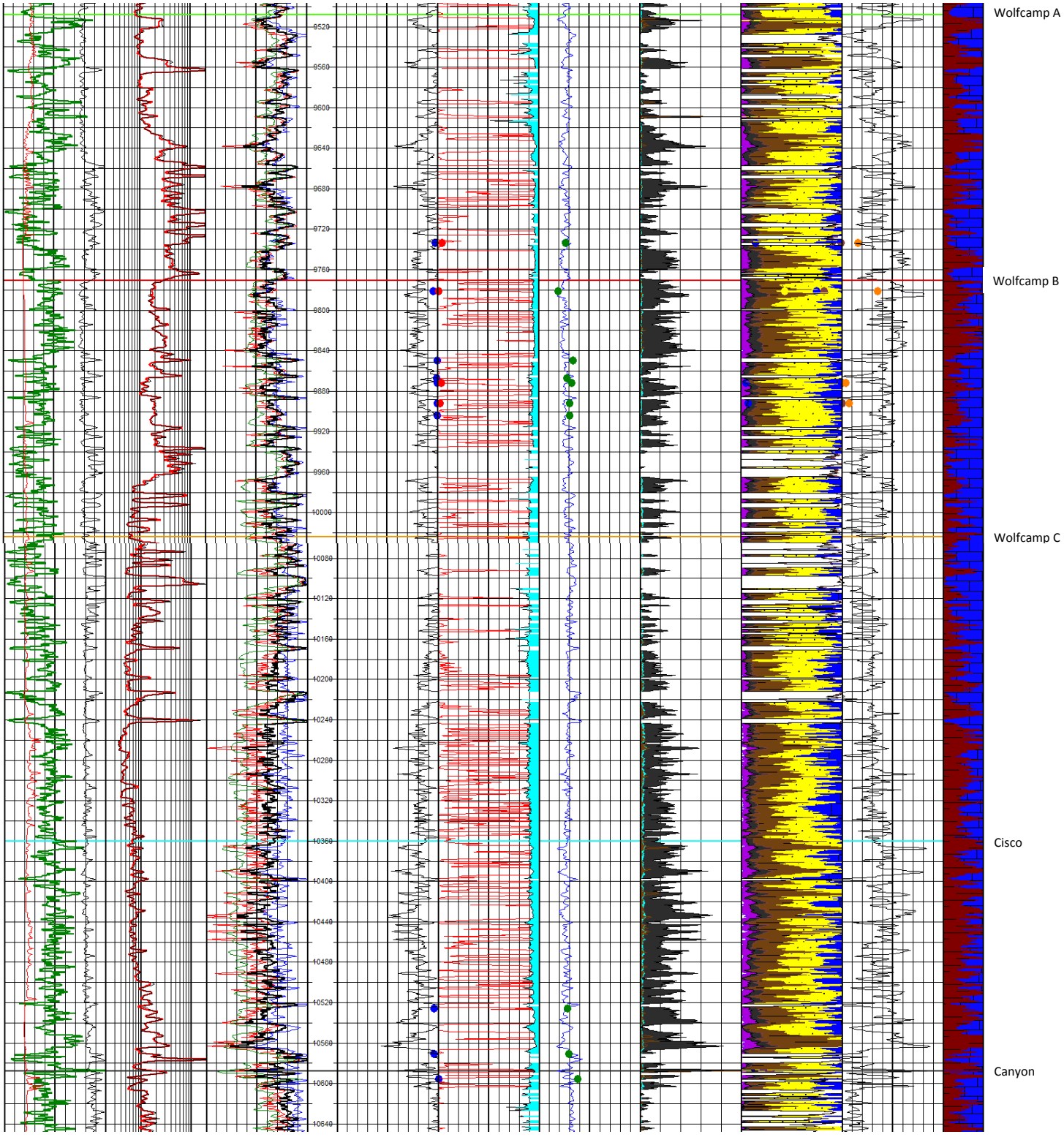

Figure 4-27: James Brown #18-2 formation tops and well logs with core data points.

4-9 Production Data

Completion and production data for wells in this study are listed in Table 4-10. All three wells were completed as verticals and stimulated using hydraulic fracturing. The wells solely target the Wolfcamp and Spraberry, except for the Spanish Trail #41-11, which also produces out of the Clearfork. The Mary Ellen #1 has been inactive since 2015 and is the only inactive well in the study, although it produced the most natural gas at 50,145 Mcf. The James Brown #18-2 was completed six years after the other two wells, yet it produced the most water at 38,136 bbls. The James Brown #18-2 also has a large perforation interval at 2,556 ft. The Spanish Trail #41-11 produced the most oil at 34,178 bbls, although it includes the Clearfork. The Mary Ellen #1 shows steady production decline until the end of 2013 when a sharp increase in water production began in early 2012, then several production fluctuations are encountered during its last two active years due to horizontal fracture hits (Figure 4-28). The Spanish Trail #41-11 shows a relatively steady production decline since coming online (Figure 4-29). The James Brown #18-2 production is variable, but generally shows decline in hydrocarbon production until mid 2017 when gas production increases and mid 2018 when oil production rose (Figure 4-30).

It should be noted that data, listed in Table 4-10 and shown in Figures 4-28 to 30, are as of October 2019.

Three stream production data for horizontal wells surrounding the three study well locations is presented in Table 4-11. Table 4-11 includes the cumulative production accompanied by lateral length, producing formation, and total months on production for each well.

Table 4-10: Completion and production data for three study wells (DrillingInfo, 2019).

Well Name	Mary Ellen #1	Spanish Trail #41-11	James Brown #18-2
County	Upton, TX	Midland, TX	Dawson, TX
Completion Year	2008	2008	2014
Type	Vertical	Vertical	Vertical
Well Status	Inactive	Active	Active
MD (ft)	9,950	10,613	11,110
TVD (ft)	9,950	10,613	11,110
Perferation Interval (ft)	7,340-9,842	7,767-	8,388-10,944
Field	Spraberry	Spraberry	Spraberry
Target Formation	Wolfberry	Clearfork & Wolfberry	Wolfberry
Cumulative Oil (bbl)	15,055	34,178	9,484
Cumulative Gas (Mcf)	50,145	21,455	16,267
Cumulative Water (bbl)	29,477	28,981	38,136

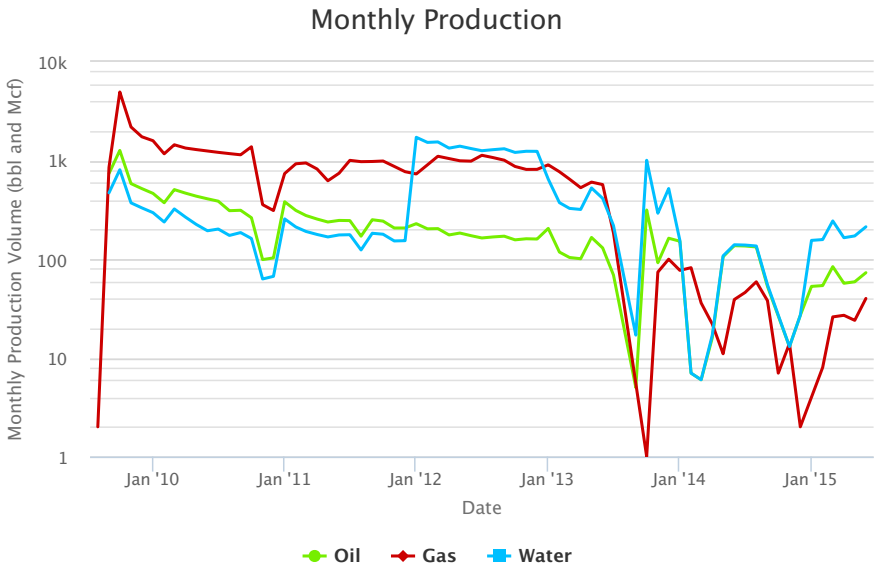

Figure 4-28: Monthly production for the Mary Ellen #1 (DrillingInfo, 2019).

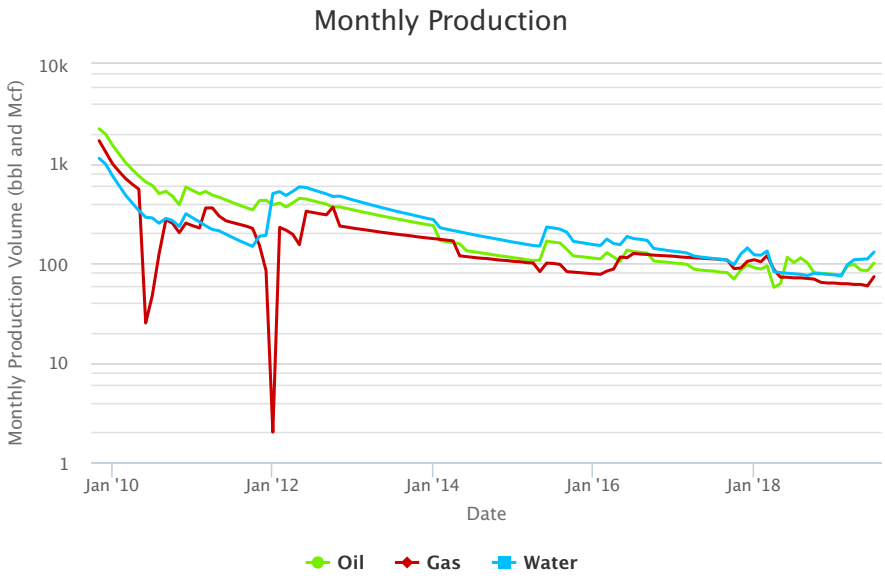

Figure 4-29: Monthly production for the Spanish Trail #41-11 (DrillingInfo, 2019).

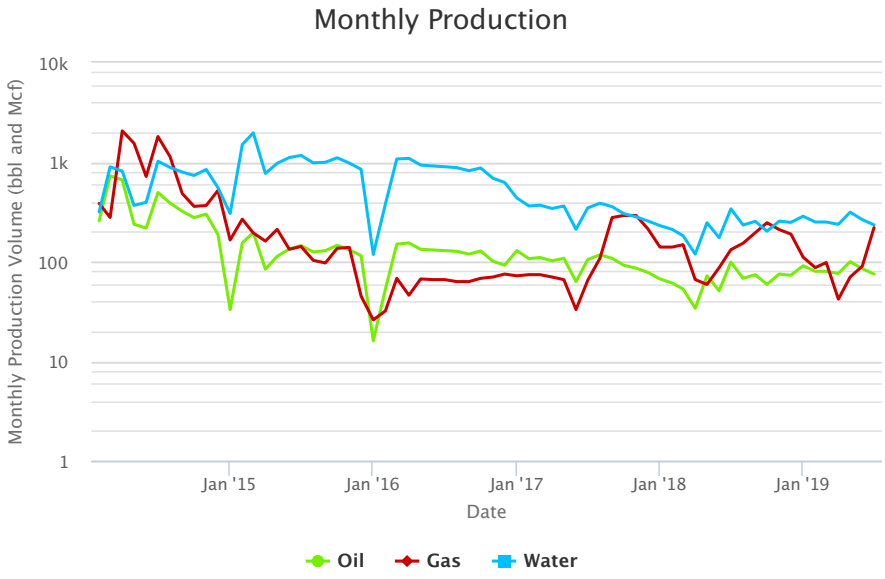

Figure 4-30: Monthly production for the James Brown #18-2 (DrillingInfo, 2019).

Table 4-11: Production data for horizontal wells surrounding the three study wells. All production reported from initial to 7/31/2019.

Production near Mary Ellen #1						
Well	**Lateral Length (ft)**	**Formation**	**Months on Production**	**Oil (bbl)**	**Gas (Mcf)**	**Water (bbl)**
Well 1	4957	Lower Spraberry	54	67,538	228,119	153,426
Well 2	4978		54	69,989	216,002	122,546
Well 3	7461	Wolfcamp B	75	131,369	1,228,686	176,457
Well 4	6965		70	124,877	623,741	136,251
Well 5	10180		58	233,496	1,566,200	287,638
Well 6	10353		72	150,630	1,045,975	184,788
Production near Spanish Traill #41-11						
Well 1	5215	Lower Spraberry	55	178,619	104,112	225,599
Well 2	5123		55	192,115	126,490	177,155
Well 3	5400		29	76,305	87,553	173,442
Well 4	5300		55	175,039	192,597	181,979
Well 5	10754	Wolfcamp A	38	240,986	192,265	152,757
Well 6	11116		38	236,353	169,365	155,958
Well 7	5041	Wolfcamp B	69	93,355	171,253	328,761
Well 8	5002		60	101,355	129,735	176,193
Well 9	5122		60	107,471	171,846	133,171
Well 10	4801		69	98,260	195,648	284,214
Production near James Brown #18-2						
Well 1	8601	Lower Spraberry	20	104,057	80,814	434,445
Well 2	8844		20	105,729	73,567	391,608
Well 3	6157	Wolfcamp B	29	73,785	25,909	137,183
Well 4	8543		63	105,129	72,911	355,017

Chapter 5: Discussion

5-1 Mineralogy

Mineralogy results from XRD analysis show that Wolfcamp samples are carbonate abundant with low to no clay content, which was expected from what is previously known about Wolfcamp formation lithology and deposition (Table 4-2). From visual inspection of carbonate-rich samples, many appear as carbonates likely formed by detrital carbonate deposition, where others are calcareous shales that are composed of clay-sized carbonate grains and skeletal

material deposited in deeper waters (Figure 3-1). There are samples in Spraberry and Wolfcamp intervals that have high quartz and feldspar content, which were specifically selected in order to test more siliceous-rich environments (Table 4-2). Coarse-grained samples with highest quartz contents are interpreted as submarine channel fan deposits. Finer grained samples with lower quartz and feldspar contents are likely to come from wind-blown sediments or distal portions of a fan complex. Low clay content throughout various facies is beneficial from a reservoir quality standpoint. Since clays are more ductile than other minerals, their absence can lead to a stiffer reservoir composed of siliciclastics and carbonates.

XRD tests were performed not only to interpret lithology of each sample, but also to check if facies determination from visual inspection of the slab matches the mineralogy detected by XRD analyses. Most XRD results corroborated the visual inspection, but some initially selected to represent more siliciclastic environments had XRD results showing high carbonate contents. High carbonate content detected in XRD analysis could be from calcite cement present in the sample (Wickard et al., 2016). However, calcite cement in siliceous rock typically does not exceed 30% (Dutton, 2008). After comparing XRD results with initial facies interpretations, three facies were determined to be compared; siliceous- clay-rich mudstone, packstone and grainstone, and carbonate mudstone.

XRD results were compared to mineralogy log curves in well logs with some minor matching success, but these density based logs typically show an underestimation of carbonate and/or an overestimation of silica and clay. Frequent, inaccurate matches of XRD results to mineralogy log curves render this particular density log derived mineralogy model inaccurate. This is not surprising due to many assumptions in densities and other values used in the total porosity for mineralogy and mineral volume curves, which could be incorrect for the entire

interval. To make the mineralogy log track more reliable throughout the Wolfberry, the photoelectric factor needs to be incorporated into the lithology determinations. The photoelectric factor can give a more defined view of lithologic differences thereby developing a more suitable mineralogy log track. In addition to the current mineralogy log curves, the shale volume curve (Vsh) also shows an overestimation of clays and underestimation of carbonates, however not as severe as the mineralogy logs. The percent carbonate results from geochemistry (acidification test) and XRD were also compared and generally match well, although there is a slight trend showing lower values of carbonate reported in the geochemistry results (Table 4-3).

Quartz and feldspars, carbonates, and clays from XRD were each compared to rock properties such as porosity, TOC, and density in Figures 5-1 through Figure 5-3. Porosity and TOC increase as quartz/feldspars and clay content increases, and decrease as carbonate content increases (Figures 5-1 and 5-2). Negative trends in porosity as carbonate content increases is possibly due to high carbonate samples being calcerous shales with finer grains and less pore space. Also, higher carbonate content samples composed of more calcite cement can fill much of the pore space. TOC trends follow porosity trends as expected since organic matter hosted pores are known to contribute heavily to the total porosity in organic rich shales (Loucks et al., 2009; Löhr et al., 2015). Density increases as carbonate content increases and decreases as clay and quartz/feldspar increases (Figure 5-3). These density trends are expected since density of quartz (2.65 g/cm^3) is less than the density of calcite (2.71 g/cm^3) and dolomite (2.87 g/cm^3). Carbonate trend in rock properties is always opposite to the quartz/feldspar and clay trends.

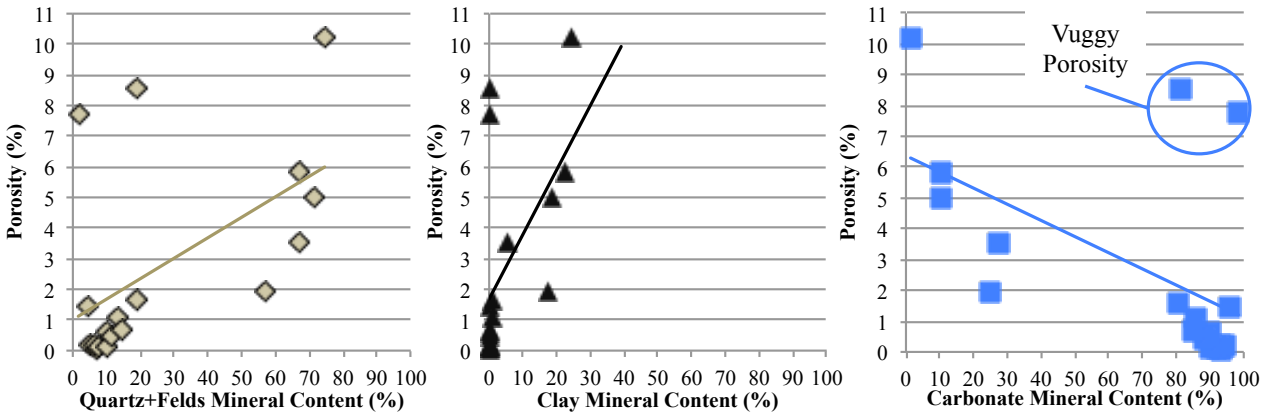

Figure 5-1: Porosity results vs. mineral content from XRD results with trend lines.

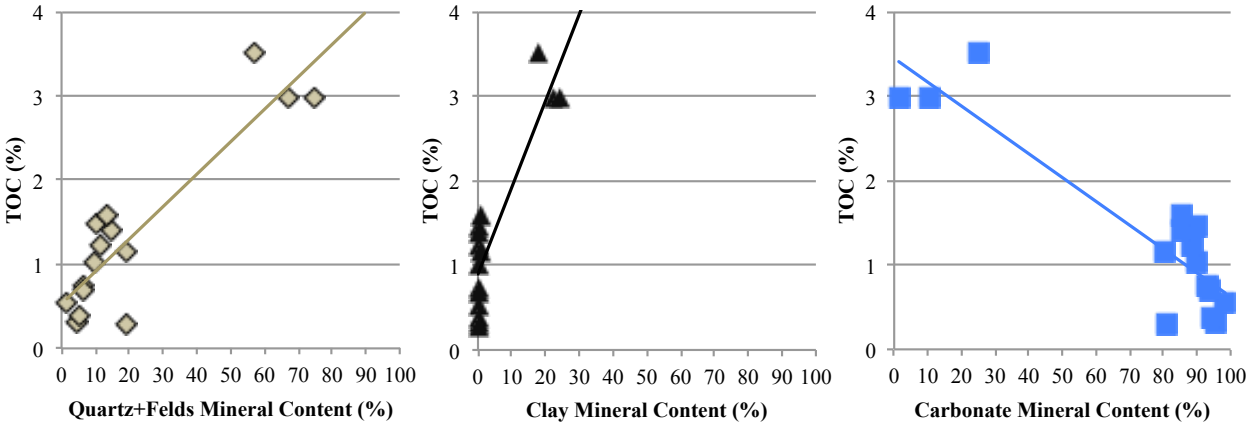

Figure 5-2: TOC results vs. mineral content from XRD results with trend lines.

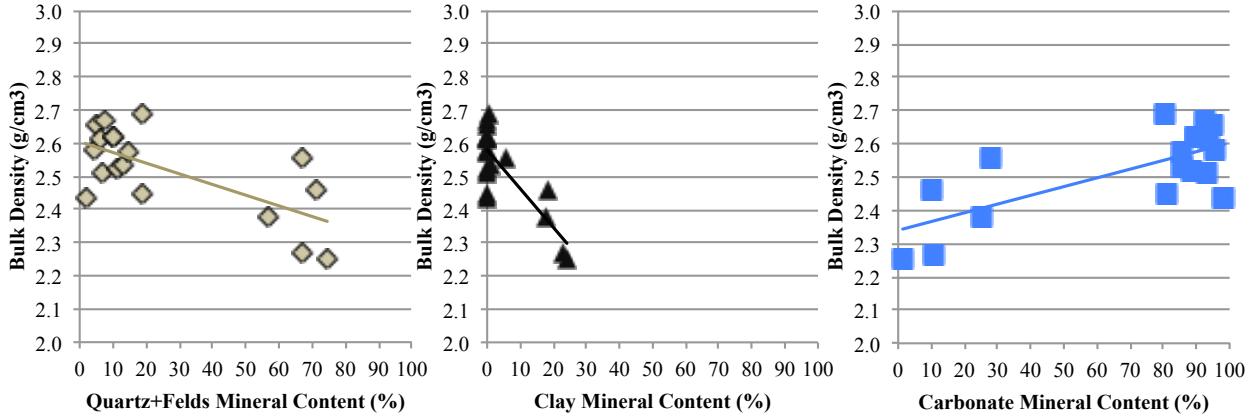

Figure 5-3: Bulk density results vs. mineral content from XRD results with trend lines.

5-2 Geochemistry

Geochemistry results from LECO TOC and HAWK pyrolysis show the Wolfcamp is organic-rich, thermally mature, and in the oil window. However, some portions are more geochemically ideal for hydrocarbon production than others, made clear by values shifting with facies composition. The three highest TOC values (3.0 - 3.5 wt%) match samples with highest clay contents from XRD (ME-9197, ST-9849, and JB-9781). Conversely, TOC values decrease as carbonate content increases (Tables 4-2 and 4-3) (Figure 5-2). These two trends are consistent with trends observed in Baumgardner and Hamlin (2014), where 3.0 wt% TOC in siliceous- and clay-rich Wolfcamp facies contrasted with 0.2 - 1.0 wt% TOC in carbonate-rich facies. Vitrinite reflectance of the Wolfcamp determined by Rodriguez (2017) illustrated %Ro of 0.85 to 0.90 that is only slightly higher than the vitrinite reflectance calculation range of %Ro from 0.53 to 0.81. Also, the vitrinite reflectance calculation indicates most of the formation is in the oil window regardless of composition, and no samples are over mature. This is expected since maturity is related to burial history after deposition. Kerogen type was not extremely clear, as several different relationships used to determine it were often not in agreement. Previous knowledge of depositional history in the Permian Basin makes sense that kerogen types would vary, but mostly be marine deposited type II kerogen (Kvale and Rahman, 2016; Gupta et al., 2017). The production index indicates that all samples are oil or gas generating and none are over mature. This confirms what was interpreted from the vitrinite reflectance calculation, but with addition of some samples in the gas generating window. How these geochemical values differ by facies composition is discussed more in the reservoir quality section.

The TOC results from core samples were compared to the Schmoker TOC relationship and illustrated low error percentage in all three wells. This TOC relationship can estimate TOC values for intervals in between sample points and in adjacent wells.

5-3 Porosity, Permeability, and Pore Structure

5-3-1 Porosity

Porosity results from MIP and vacuum-assisted FIP in DI water, DT2, and THF illustrate a range of porosity values that have agreement (Table 5-1). When comparing results of all five different methods, a difference of less than 1.5 % for porosity in all samples except for ME-9197 and ST-9849, which both had fracture indicators from MIP tests giving them much higher porosity values compared to FIP tests. THF tests serve as the low-bound due to rate of evaporation from the THF-saturated samples during sample weighing and processing. MIP and DT2 FIP results matched most closely, but since MIP is able to detect pore space to 2.8 nm in diameter and non-wetting mercury is pressurized up to 60,000 psi, these results demonstrated the most legitimate porosities. Still, use of DIW and DT2 gave an opportunity to measure fluid-accessible porosity, by considering wettability of these as-received samples. A difference of less than 1.5 % was observed except for samples ME-9052, ME-9197, ST-9841, ST-9449, JB-9187, and JB-9781. In most samples FIP tests underestimate porosity when compared to MIP tests (Table 5-1). This underestimation is expected due to lack of pressure in FIP testing not forcing fluid into the interior and smaller pore space. Also, as mentioned above, there is a connection between increasing TOC and increasing porosity, which is expected due to organic matter hosted pores contributing to total porosity in these organic rich shales (Loucks et al., 2009; Löhr et al., 2015) (Figure 5-4).

As to sample size effect, vacuum-assisted FIP porosity results on plug-sized samples in DI water were used for all samples that did not undergo MIP testing (Table 4-1). Although not ideal, these results were not unreasonable when comparing to MIP results in the 17 samples tested using both methods (Table 5-1). Sample size appears to not have much of an effect on porosity value, where half of FIP DIW tested plugs had higher porosity values than FIP DIW tested cubes and half had lower values (Table 5-1).

Porosity results from the Spraberry range from 0.1 to 5.0 % and are lower than the 8.6 to 9.6 % reported by Quintero (2016). The Wolfcamp porosity results illustrate a larger range (0.1 to 10.21 %) than the 0.9 to 2.7 % reported by Quintero (2016).

Porosity results from laboratory methods were compared to neutron, density, sonic, and total porosity log curves in well logs. A clear overestimation of porosity is displayed in all measured well log curves (Figures 4-25 to 27). The shifted and scaled corrected porosity curve in track four generally matches laboratory porosity data with only a few exceptions (Figures 4-25 to -27). This can be explained by larger sampling volumes (several feet) of the well logging approach. Corrected porosity curves can be used to estimate porosity values for intervals that lie in between sampled points. However, since the corrected porosity curve is a custom fit for data in its respective well, there is not a good way to compare against adjacent wells unless there is core porosity data for those wells.

Table 5-1: Porosity measurements from different methods (%). Siliceous- clay-rich facies in tan, packstone and grainstone facies in blue, and carbonate mudstone in gray.

Sample ID	Porosity (%)				
	MIP	Vacuum Assisted FIP			
		DI Water		DT2	THF
		Plug Size	Cube Size		
ME-9197	5.85	0.67	2.35	3.31	2.38
ST-8877	3.51	2.69	3.19	3.50	3.61
ST-9849	10.20	1.11	2.18	3.04	3.03
JB-9187	5.02	2.44	4.21	5.91	6.03
JB-9781	1.95	0.29	1.20	2.52	1.59
ME-8027	0.11	0.08	0.08	0.22	0.10
ME-8633	0.44	0.38	0.34	0.97	1.21
ME-9031	1.47	1.51	1.11	1.48	2.28
ME-9052	8.53	6.60	6.24	7.31	5.66
ME-9207	-	0.29	0.46	1.62	0.96
ST-9612	0.63	0.30	0.37	1.05	1.29
ST-9841	7.75	4.26	6.11	7.43	6.56
JB-9733	1.09	0.26	0.16	1.03	0.62
JB-9871	0.16	0.36	0.17	0.45	0.18
ME-8621	0.70	0.59	0.44	0.72	0.59
ME-8866	0.04	0.21	0.13	0.65	0.27
ST-9632	0.15	0.42	0.21	0.66	0.30
JB-9891	0.17	0.26	0.53	0.86	0.34

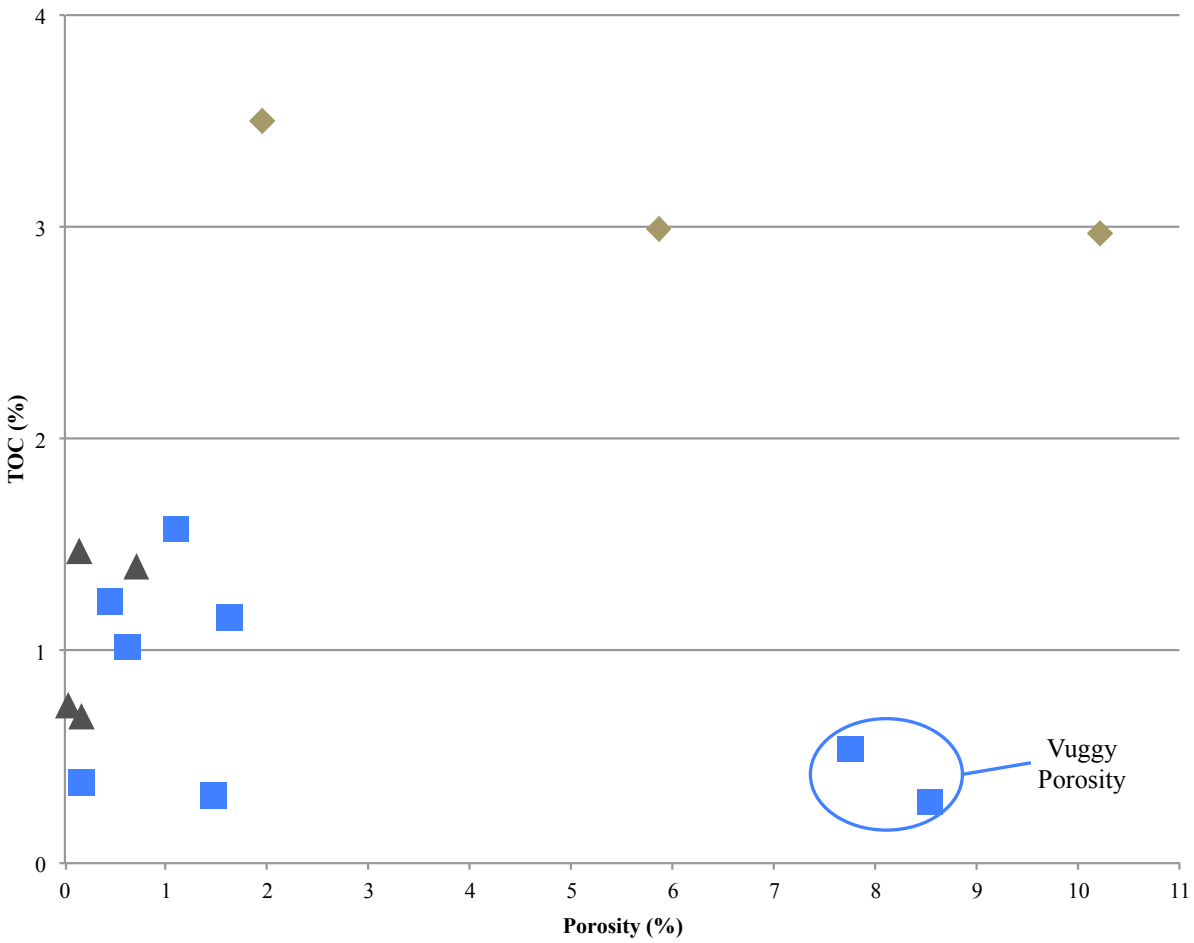

Figure 5-4: Porosity results vs. TOC results. Siliceous- clay-rich facies represented by tan diamonds, packstone and grainstone facies represented by blue squares, and carbonate mudstone represented by gray triangles.

5-3-2 Permeability

Permeability results from MIP tests show a wide range of permeability values indicating mixed ability for fluid flow through pore space. The highest permeability results are in samples ME-9052 and ST-9849, where ST-9849 has a fracture indicator from the MIP results. Intrusion volume associated with this fracture was excluded from the matrix permeability calculation for matrix permeability to be compared to other samples and other areas of the formation. However, often times there are fracture networks associated with large fractures and since fluid is able to travel through fractures easily, this is likely the reason the permeability is as high as it is in ST-

9849. For all samples, as expected, permeability generally increases as porosity increases (Figure 5-5).

Permeability results from the Spraberry range from 61.9 to 68178 nD, which is within the range of 5.0 to 321,065 nD permeabilities reported by Mzee (2019). The Wolfcamp permeability results illustrate a larger range than Spraberry results at 0.5 to 3,813,299,885 nD, this is similar to the 0.8 to 486,906 nD range reported by Mzee (2019) although with a much larger high bound.

MIP permeability results were compared to estimated Timur permeability log curves. The core permeability data does not match well with calculated log permeability. Attempts to calculate a curve that did match, failed (Figures 4-25 to 27). Since permeability in these heterogeneous shales is difficult to measure using MIP, it is not clear whether mismatching core data points and larger-scaled log curves is a function of the core data or the log equation.

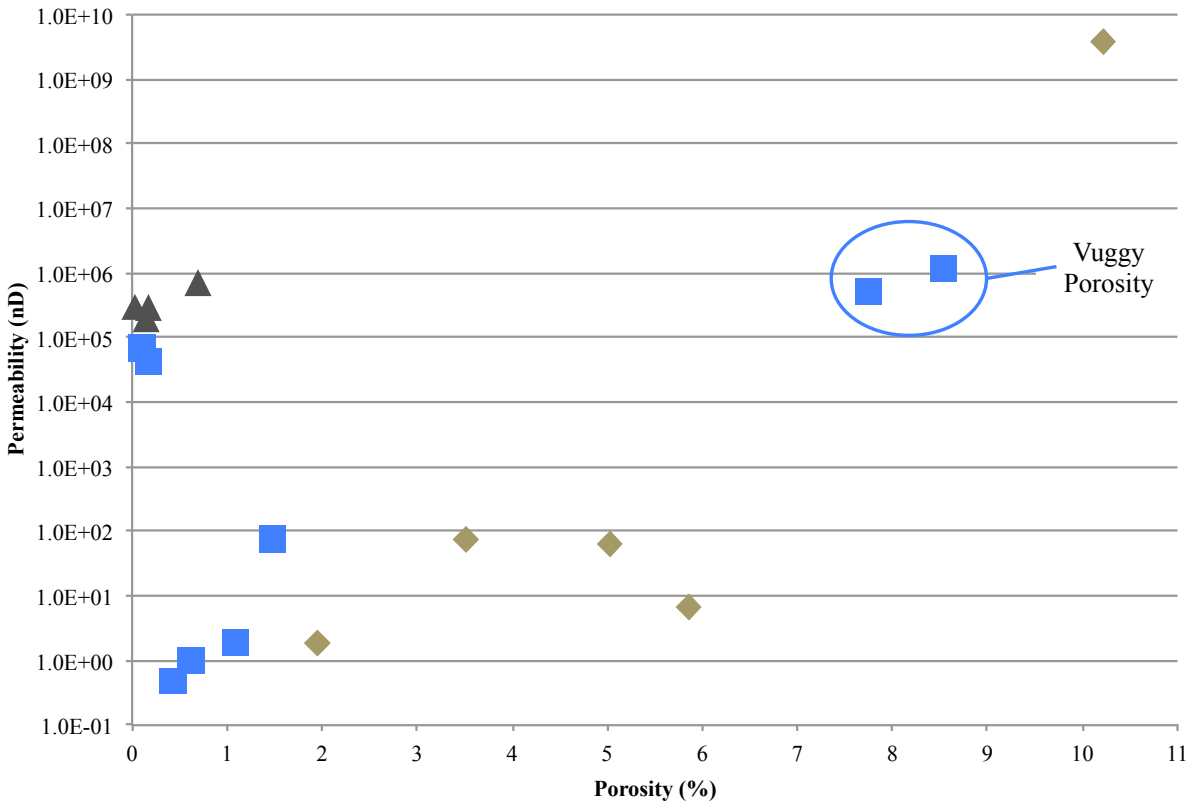

Figure 5-5: Porosity results vs. permeability results. Siliceous- clay-rich facies represented by tan diamonds, packstone and grainstone facies represented by blue squares, and carbonate mudstone represented by gray triangles.

5-3-3 Pore Structure and Wettability

The pore structure for samples in this study is defined by pore size distribution, tortuosity, connectivity, and wettability of the sample. A combination of MIP, imbibition, and contact angle tests were used to acquire these data. Pore structure results for the Spraberry and Wolfcamp samples are not consistent throughout, which is expected due to formation heterogeneity (Table 4-7). Samples dominated by macropore networks (>100 nm) consisting of micro-fractures, laminations, and/or intergranular pores have higher permeablities and lower tortuosities than samples dominated by micropore networks (2.8-50 nm) consisting of intragranular, organic matter hosted, and/or inter-clay platelet pores (Table 5-2) (Tonietto et al., 2014; Hu et al., 2017). This relationship is expected since fluid can flow more easily and more directly through fractures, along laminations, and in intergranular pores. Larger pore dominated samples do have more direct potential pathway to hydraulic fractures and the well bore. However, smaller sized pores can be accessed through hydraulic fracturing of the reservoir and play a part in the total volumes of fluid held in each reservoir.

Pore connectivity in shale, determined by fluid imbibition, is greatly related to wettability. Connectivity in most samples was much higher when using hydrophobic DT2 than when using hydrophilic DI water (Table 4-5). This would suggest that a hydrophobic fluid like oil would be more easily displaced than a hydrophilic fluid like water in Spraberry and Wolfcamp intervals. This was unexpected as contact angle results showing most samples are predominantly oil-wet, meaning that oil is more likely to surround the grains making other fluids like water easier to displace (Table 4-8). However, this can be explained by the fact that 100% DT2 was used in imbibition tests. DT2 is able to invade pore space at very high efficiencies and

wettability of the sample hardly affects its ability to invade. This is made clear in contact angle results where the DT2 droplet always invades and flattens to less than 3 degrees in less than one second (Table 4-8). DT2 is also 67% toluene, which often can clean a sample and change wettability. For a more accurate view of connectivity related to fluids similar to oil, an additional fluid like 20% THF could be used in future imbibition tests. Contact angle results indicating that Spraberry and Wolfcamp intervals are largely oil-wet, meaning that water is more easily displaced, is likely a contributing factor to why water production in these wells is often higher than oil production (Table 4-9).

Table 5-2: Sample grouped by predominate pore network, showing larger permeabilities and lower tortuosities in samples dominated by macropores.

Predominate Pore Network	Sample ID	Permeability (mD)	Geometrical Tortuosity (L_e/L)
Macropores (>100 nm)	ME-8027	0.07	0.09
	ME-8621	0.71	0.23
	ME-8866	0.31	0.04
	ME-9052	1.18	3.46
	ME-9197	6.68E-06	107.9
	ST-9632	0.19	0.08
	ST-9841	0.52	4.36
	ST-9849	3813	0.21
	JB-9871	0.04	0.15
	JB-9891	0.28	0.10
Micropores (2.8-50 nm)	ME-8633	4.96E-07	3.81
	ME-9031	7.29E-05	2.21
	ST-8877	7.50E-05	24.29
	ST-9612	1.02E-06	3.85
	JB-9187	6.19E-05	30.19
	JB-9733	1.90E-06	5.64
	JB-9781	1.83E-06	8.74

5-4 Bulk and Grain Densities

Bulk and grain density results, from MIP and vacuum-assisted FIP in DI water, DT2, and THF, show similar values (Tables 5-3 and 5-4). When comparing results from five methods used for bulk density determination, absolute error is less than 0.15 g/cm^3, except for in ME-8633, ME-8866, ME-9197, and ST-9849. Tight results assist in substantiating the rest of FIP density results for samples that were not tested using MIP. However, MIP density results are almost all lower than FIP results, and furthermore DT2 FIP results are consistently highest in both bulk and particle density results followed by THF FIP.

Apparent bulk density results from pycnometry show a decrease as sample size decreases. This is expected since porosity and density have an inverse relationship and edge accessible porosity invaded during pycnometry comprises more total porosity as sample size decreases. Pycnometry results also illustrate higher reported densities when testing in DT2 than when testing in DIW. This is unexpected since DT2 is able to invade the pore space better than DIW, which should result in higher porosity values and lower bulk density values. A potential cause for this is difficulty of this method using small volumes causing inconsistent density results. Pycnometry weights could be impacted by many variables, including DT2 evaporation, excess fluid on the pycnometer surface, and air trapped in the pycnometer.

Bulk density results from laboratory methods were compared to bulk density log curves in track seven of the log montage (Figures 4-25 to 27). Laboratory collected bulk densities match measured log curve bulk densities with a very low error percentage. This level of matching from laboratory-scale bulk densities to the logging-scale bulk densities helps validate several calculated log curves that use bulk density curves. Also, core data matching density log curves

can be used to estimate a density value for intervals that lie in between sampled points in the three sampled wells and adjacent wells.

Table 5-3: Bulk density measurements from different methods (g/cm^3). Siliceous- clay-rich facies in tan, packstone and grainstone facies in blue, and carbonate mudstone in gray.

Sample ID	Bulk Density (g/cm3)				
	MIP	Vacuum Assisted FIP			
		DI Water		DT2	THF
		Plug Size	Cube Size		
ME-9197	2.268	2.497	2.479	2.511	2.495
ST-8877	2.554	2.601	2.611	2.665	2.651
ST-9849	2.252	2.480	2.485	2.553	2.499
JB-9187	2.462	2.522	2.534	2.595	2.571
JB-9781	2.380	2.472	2.520	2.519	2.496
ME-8027	2.669	2.682	2.687	2.757	2.749
ME-8633	2.522	2.613	2.651	2.710	2.673
ME-9031	2.582	2.649	2.653	2.729	2.683
ME-9052	2.448	2.497	2.524	2.558	2.582
ME-9207	-	2.628	2.646	2.691	2.689
ST-9612	2.617	2.640	2.632	2.693	2.673
ST-9841	2.434	2.504	2.513	2.553	2.555
JB-9733	2.534	2.601	2.602	2.670	2.659
JB-9871	2.654	2.691	2.704	2.736	2.741
ME-8621	2.576	2.613	2.633	2.710	2.672
ME-8866	2.510	2.644	2.647	2.705	2.679
ST-9632	2.618	2.610	2.663	2.701	2.690
JB-9891	2.613	2.706	2.695	2.752	2.747

Table 5-4: Grain density measurements from different methods (g/cm^3). Siliceous- clay-rich facies in tan, packstone and grainstone facies in blue, and carbonate mudstone in gray.

Sample ID	Grain Density (g/cm3)				
	MIP	Vacuum Assisted FIP			
		DI Water		DT2	THF
		Plug Size	Cube Size		
ME-9197	2.409	2.514	2.539	2.597	2.556
ST-8877	2.647	2.673	2.697	2.762	2.751
ST-9849	2.508	2.500	2.540	2.633	2.577
JB-9187	2.592	2.585	2.646	2.758	2.736
JB-9781	2.427	2.479	2.550	2.584	2.537
ME-8027	2.672	2.684	2.689	2.763	2.752
ME-8633	2.533	2.623	2.660	2.737	2.705
ME-9031	2.621	2.689	2.682	2.770	2.745
ME-9052	2.676	2.673	2.692	2.759	2.737
ME-9207	-	2.635	2.658	2.736	2.715
ST-9612	2.633	2.648	2.641	2.721	2.707
ST-9841	2.639	2.616	2.677	2.758	2.734
JB-9733	2.562	2.607	2.606	2.698	2.675
JB-9871	2.659	2.701	2.709	2.749	2.746
ME-8621	2.594	2.628	2.645	2.729	2.688
ME-8866	2.511	2.650	2.644	2.723	2.687
ST-9632	2.621	2.630	2.669	2.719	2.698
JB-9891	2.618	2.713	2.710	2.776	2.756

5-5 Well Logging and Upscaling Lab Results

All calculated log curves, have been discussed aside from kerogen and fluid volumes (Figures 4-25 to 27). In addition to TOC and density log curves being fairly validated by core data, the kerogen volume curve can be viewed with some assurance since it was calculated from TOC and density logs. For water, clay bound water, and hydrocarbon volumes a combination of the Vsh (shale volume), corrected porosity, and S_w (water saturation) curves were used. The Vsh curve is a clay indicator more than a shale indicator due to the Wolfcamp containing shale that is mostly composed of clay-sized carbonate and silica grains. Corrected porosity was checked against core data and matches to some extent. S_w is determined from Archie's equation and is

unable to be verified based on data provided, but since the Archie equation is often insufficient for hybrid tight reservoirs like the Wolfcamp, the S_w is likely unsuitable (Equation 3-19). A more suitable shale corrected water saturation determination using the Simandoux or Dual Water model could be incorporated and compared. Based on accuracy of these curves, fluid volumes are likely unreliable. Although potentially unreliable, observations from fluid volume contents suggest hydrocarbon volume is significantly higher than volumes of water and clay-bound water (Figures 4-25 to 27). This is expected since intervals are thought to be oil-wet and although an oil-wet reservoir indicates that relative permeability is higher for water than oil, it also signifies that there should be higher volumes of hydrocarbon present in the reservoir.

In-depth interpretation of well log facies for pay intervals and log response rational behind those interpretations is beyond the scope of this study. This study is focused more on comparing core results to log curves and determining how core-based facies affect reservoir quality. However, some rudimentary observations of the well logs can be made as follows.

There are several zones of washout displayed by caliper curves rising above gauge hole. These zones from 9020-9080 ft in the Mary Ellen #1, 8300-8500 ft and 8940-9100 ft in the Spanish Trail #41-11, and 9160-9180 in the James Brown #18-2 are possible lithological indicators of thin friable clay-rich shale intervals (Figures 4-25 to 27). Deep and shallow resistivity curves indicate a dense tight carbonate lithology when the two curves are reading very high resistivity values like from 8010-8050 ft in the Mary Ellen #1 (Figure 4-25).

Deep and shallow resistivity curves can indicate fluid content and potential hydrocarbon bearing zones like in the Mary Ellen #1 from 8800-8880 ft. Deep resistivity is high with slight offset to shallow resistivity (Figure 4-25). Hydrocarbon potential identified with resistivity logs,

is corroborated by the corrected porosity curve. Although it is potentially clay rich, XRD core data at 8866 ft is 93% carbonate (Table 4-2).

High porosity zones are areas of interest within the well due to their ability to store large volumes of fluids. The high porosity zone from 10200-10560 ft in the James Brown #18-2 indicated by the corrected porosity curve being high for Wolfcamp shale intervals. Resistivity curves are reading low values indicating a clay heavy shale, which is corroborated by gamma ray and Vsh curves (Figure 4-27). This clay heavy zone could make this area more ductile and more difficult to fracture as a result. However, the high TOC and connected high porosity indicate a great potential hydrocarbon source interval.

In general, well logs corroborate heterogeneity of Wolfcamp intervals. Due to heterogeneity and low porosity there are not any continuous pay intervals, but numerous smaller isolated pay intervals with low porosity exist and were accessed and stimulated via hydraulic fracturing.

5-6 Production by Location

Production data was scaled to 10,000 ft laterals in order to normalize the data for comparisons (Table 5-5). The scaled data was then normalized further to production per 18 months and averaged by formation and location (Table 5-5). Although production is not constant through time, based on the data that is presentable, scaling in this time manner is the only option.

The northern and central areas surrounding the Spanish Trail #41-11 and James Brown #18-2 have considerably higher oil production than the southern area surrounding Mary Ellen #1. However, the area surrounding Mary Ellen #1 has significantly higher gas production than the other two areas. This noticeable difference in production volumes may be due to different deposited organic materials and hydrocarbon maturities in these areas. The burial history and

deposited organics in the southern area surrounding the Mary Ellen #1 is leading to more mature gas prone reservoirs. The hydrocarbon maturity controls API gravity and this difference in maturity would lead to less viscous oil that able to flow through connected pore space more quickly significantly impacting the oil production. Further analyzing the burial history, organic deposition, maturity indicators, and oil API gravities for different areas around the basin would lead to more conclusive evidence regarding this difference in production.

Table 5-5: Normalized production data for horizontal wells surrounding study wells.

Formation	Cumulative Production per 10000 ft Laterals			Cumulative Production per 10,000 ft Lateral per 18 Months			Cumulative Production Formation Average		
	Oil (bbl)	Gas (Mcf)	Water (bbl)	Oil (bbl)	Gas (Mcf)	Water (bbl)	Oil (bbl)	Gas (Mcf)	Water (bbl)
Production Near Mary Ellen #1									
Lower Spraberry	136,248	460,196	309,514	45,416	153,399	103,171	46,141	149,018	92,615
	140,597	433,913	246,175	46,866	144,638	82,058			
Wolfcamp B	176,074	1,646,811	236,506	42,258	395,235	56,761	48,980	338,890	59,844
	179,292	895,536	195,622	46,104	230,281	50,303			
	229,367	1,538,507	282,552	71,183	477,468	87,689			
	145,494	1,010,311	178,487	36,374	252,578	44,622			
Production Near Spanish Trails #41-11									
Lower Spraberry	342,510	199,640	432,596	112,094	65,337	141,577	107,654	91,426	141,620
	375,005	246,906	345,803	122,729	80,806	113,172			
	141,306	162,135	321,189	87,707	100,636	199,359			
	330,262	363,391	343,357	108,086	118,928	112,371			
Wolfcamp A	224,090	178,785	142,047	106,148	84,687	67,285	103,432	78,429	66,872
	212,624	152,361	140,300	100,717	72,171	66,458			
Wolfcamp B	185,191	339,720	652,174	48,311	88,623	170,132	56,359	93,348	127,059
	202,629	259,366	352,245	60,789	77,810	105,674			
	209,822	335,506	259,998	62,947	100,652	77,999			
	204,666	407,515	591,989	53,391	106,308	154,432			
Production Near James Brown #18-2									
Lower Spraberry	120,982	93,959	505,110	108,884	84,563	454,599	108,239	79,714	426,557
	119,549	83,183	442,795	107,594	74,865	398,516			
Wolfcamp B	119,839	42,081	222,808	74,383	26,119	138,295	54,771	25,252	128,514
	123,059	85,346	415,565	35,160	24,385	118,733			

5-7 Reservoir and Source Quality Evaluation

For reservoir and source quality evaluation the various sample compositions were combined into three facies; siliceous and/or clay rich lithotype, carbonate packstone and grainstone, and carbonate mudstone and wackestone. These facies are similar to facies used by Baumgardner and Hamlin (2014). The rock properties used to classify reservoir and source quality for each facies group in the Lower Spraberry and four Wolfcamp intervals for the three sampled wells are displayed in Table 5-6 with a sample ID depth legend displayed in Table 5-7.

Table 5-6: Comparison of three generalized facies reservoir and source rock properties for each stratigraphic unit in each well.

Stratigraphic Unit	Property		Mary Ellen #1			Spanish Trail #41-11			James Brown #18-2		
			Siliceous/ Clay Rich	Packstone Grainstone	Mudstone/ Wackestone	Siliceous/ Clay Rich	Packstone Grainstone	Mudstone/ Wackestone	Siliceous/ Clay Rich	Packstone Grainstone	Mudstone/ Wackestone
Spraberry	Pore Structure	Porosity (%)	3.03	0.11	2.44 (Fractured)	3.51	-	1.00	5.02	-	1.18
		Permeability (mD)	-	0.07	-	7.50E-5	-	-	6.19E-5	-	-
		Tortuosity	-	0.09	-	24.29	-	-	30.19	-	-
		Wettability	-	Partial Oil-Wet	-	Water-Wet	-	-	-	-	-
		Bulk Density (g/cm^3)	-	2.69	-	2.55	-	-	2.46	-	-
		Grain Density (g/cm^3)	-	2.67	-	2.65	-	-	2.59	-	-
	Geochemistry	TOC (wt%)	-	-	-	-	-	-	-	-	-
		Vitrinite Reflectance (%Ro)	-	-	-	-	-	-	-	-	-
		Free Oil + Gen. Pot. (S1+S2)	-	-	-	-	-	-	-	-	-
	Mineralogy	Quartz + F (%)	-	8	-	67	-	-	71	-	-
		Carbonate (%)	-	92	-	28	-	-	10	-	-
		Clay (%)	-	0	-	5	-	-	19	-	-
		XRD lithofacies	-	Carbonate Dominated	-	Carb-rich Siliceous	-	-	Mixed Siliceous	-	-
Wolfcamp A	Pore Structure	Porosity (%)	-	0.44	0.70	-	0.63	0.15	-	1.09	
		Permeability (mD)	-	4.96E-7	0.71	-	1.02E-6	0.19	-	1.90E-6	-
		Tortuosity	-	3.81	0.23	-	3.85	0.08	-	5.64	-
		Wettability	-	Oil-Wet	Partial Oil-Wet	-	Oil-Wet	Intermediate	-	Intermediate	-
		Bulk Density (g/cm^3)	-	2.52	2.58	-	2.62	2.62	-	2.53	-
		Grain Density (g/cm^3)	-	2.53	2.60	-	2.63	2.62	-	2.56	-
	Geochemistry	TOC (wt%)	-	1.23	1.40	-	1.02	1.47	-	1.58	-
		Vitrinite Reflectance (%Ro)	-	0.75	0.75	-	0.62	0.80	-	0.68	-
		Free Oil + Gen. Pot. (S1+S2)	-	2.87	3.07	-	2.76	4.09	-	6.42	-
	Mineralogy	Quartz + F (%)	-	12	15	-	10	10	-	13	-
		Carbonate (%)	-	88	85	-	90	90	-	86	-
		Clay (%)	-	0	0	-	0	0	-	1	-
		XRD lithofacies	-	Carbonate Dominated	Carbonate Dominated	-	Carbonate Dominated	Carbonate Dominated	-	Carbonate Dominated	-
Wolfcamp B	Pore Structure	Porosity (%)	-	8.53	1.47	0.04	10.21	7.75	0.13	1.95	0.17	0.17
		Permeability (mD)	-	1.18	7.3e-5	0.31	3813.3	0.52	-	1.83E-6	0.04	0.28
		Tortuosity	-	3.46	2.21	0.04	0.21	4.36	-	8.74	0.15	0.10
		Wettability	-	Oil	Inter.	Oil-Wet	Oil-Wet	Oil-Wet	-	Intermediate	Oil-Wet	Intermediate
		Bulk Density (g/cm^3)	-	2.45	2.58	2.51	2.25	2.43	-	2.53	2.65	2.61
		Grain Density (g/cm^3)	-	2.68	2.62	2.51	2.51	2.64	-	2.56	2.66	2.62
	Geochemistry	TOC (wt%)	-	0.29	0.32	0.74	2.97	0.54	-	3.50	0.38	0.69
		Vitrinite Reflectance (%Ro)	-	0.68	0.72	0.71	0.70	0.54	-	0.68	0.57	0.67
		Free Oil + Gen. Pot. (S1+S2)	-	0.88	0.54	1.40	8.05	2.54	-	15.10	1.15	1.48

	Mineralogy	Quartz + F (%)	-	19	4	7	75	2	-	57	5	7
		Carbonate (%)	-	81	96	93	1	98	-	25	95	93
		Clay (%)	-	0	0	0	24	0	-	18	0	0
		XRD lithofacies	-	Carbonate Dominated		Carbonate Dominated	Clay-rich Siliceous	Carbonate Dominated	-	Mixed Siliceous	Carbonate Dominated	Carbonate Dominated
Wolfcamp C	Pore Structure	Porosity (%)	5.85	1.62		-	-	-	3.00 (Fctd)	-	-	-
		Permeability (mD)	6.68E-6	-		-	-	-	-	-	-	-
		Tortuosity	107.93	-		-	-	-	-	-	-	-
		Wettability	Oil-Wet	Oil-Wet		-	-	-	-	-	-	-
		Bulk Density (g/cm^3)	2.27	2.69		-	-	-	-	-	-	-
		Grain Density (g/cm^3)	2.41	2.74		-	-	-	-	-	-	-
	Geochemistry	TOC (wt%)	2.99	1.16		-	-	-	-	-	-	-
		Vitrinite Reflectance (%Ro)	0.71	0.70		-	-	-	-	-	-	-
		Free Oil + Gen. Pot. (S1+S2)	5.90	2.35		-	-	-	-	-	-	-
	Mineralogy	Quartz + F (%)	67	19		-	-	-	-	-	-	-
		Carbonate (%)	11	80		-	-	-	-	-	-	-
		Clay (%)	23	1		-	-	-	-	-	-	-
		XRD lithofacies	Mixed Siliceous	Carbonate Dominated		-	-	-	-	-	-	-
Wolfcamp D	Pore Structure	Porosity (%)	-	0.46 (Avg.)		8.13 (Fractured)	-	-	2.84 (Fractured)	-	-	1.27 (Avg.)

Table 5-7: Sample ID depth reference for the data presented in Table 5-6.

Stratigraphic Unit	**Mary Ellen #1**			**Spanish Trail #41-11**			**James Brown #18-2**		
	Siliceous/ Clay Rich	Packstone Grainstone	Mudstone/ Wackestone	Siliceous/ Clay Rich	Packstone Grainstone	Mudstone/ Wackestone	Siliceous/ Clay Rich	Packstone Grainstone	Mudstone/ Wackestone
Spraberry	8004	8027	8063	8877		9400	9187		9209
Wolfcamp A		8633	8621		9612	9632		9733	
Wolfcamp B		9052 & 9031	8866	9849	9841	9833	9781	9871	9891
Wolfcamp C	9197	9207				10053 & 10067			
Wolfcamp D		9511 & 9528	9509			10310, 10318 & 10322			10525, 10570 & 10595

5-7-1 Facies Effect on Reservoir and Source Quality by Basin Location

In this study one well was sampled in the northern, central and southern portions of the Midland Basin. One well is not enough to classify an entire portion of the basin, especially for heterogeneous intervals of the Wolfcamp Shale. However, comparisons of northern, central, and southern Midland Basin reservoir and source quality are made for the Lower Spraberry, Wolfcamp A, B, C, and D.

In the Lower Spraberry stratigraphic interval siliceous- clay-rich facies has a moderate reservoir quality, which is much higher than both carbonate facies, where packstone and grainstone facies displays the poorest reservoir quality. Siliceous- clay-rich facies in the northern James Brown well has higher reservoir quality than the siliceous- clay-rich facies in the central Spanish Trail well. Carbonate mudstone exhibits moderate reservoir in the southern Mary Ellen well due to fractures creating secondary porosity.

The Wolfcamp A packstone and grainstone group has poor, but increasing, reservoir quality from north to south in the basin and the carbonate mudstone facies forms poor reservoirs in both central and southern portions, The northern well was not adequately sampled for this interpretation. Source potential is fair and stays similar in all three areas and in both carbonate facies.

The Wolfcamp B siliceous- clay-rich facies has the highest reservoir and source quality out of any facies and formation. The siliceous- clay-rich reservoir is best in the central Spanish Trail well followed by the northern James Brown well, but source quality is highest in the northern James Brown well. The packstone and grainstone facies displays high reservoir quality in vuggy carbonates to the south and central wells, but still has a low source potential aside from notable storage. This is expected since vuggy porosity is secondary porosity and TOC

relationships with porosity is related to primary porosity. Reservoir and source quality of the carbonate mudstone facies is poor throughout all three locations.

In the Wolfcamp C siliceous- clay-rich facies have acceptable reservoir and great source followed by fair reservoir and source in the packstone and grainstone facies. Moderate reservoirs in the carbonate mudstones are due to fractures creating secondary porosity.

Wolfcamp D fractured carbonate mudstones have high reservoir quality, which is most ideal in the southern Mary Ellen well due to secondary porosity and fluid pathways created by fractures. The packstone and grainstone facies forms a poor reservoir in this interval.

5-7-2 Facies Effect on Reservoir and Source Quality by Formation

Siliceous- clay-rich facies reservoir and source quality are both high and are highest of all three facies groups. The Wolfcamp B appears to form ideal reservoir and source followed by the Wolfcamp C then the Spraberry. However, Wolfcamp A and D siliceous- clay-rich facies were not tested.

The packstone and grainstone facies typically has poor reservoir potential. However, in the Wolfcamp B, vuggy secondary porosity associated with this group gives it high reservoir quality. The packstone and grainstone facies has fair source quality in both the Wolfcamp C and A and poor source quality in the Wolfcamp B. Spraberry and Wolfcamp D were not tested for source potential.

The carbonate mudstone facies has poor reservoir and source quality due to extremely low porosity, which is associated with heavy calcite cement. However, fractures are present in this facies and show large increases in reservoir quality like the Wolfcamp D, C, and Spraberry intervals. Source quality for this facies was only tested in the Wolfcamp A and B, where the Wolfcamp A has fair source potential and the Wolfcamp B has a poor source potential.

5-7-3 Overall Reservoir and Source Quality Trends by Facies

Neither the formation interval nor basin location has much effect on how facies influence reservoir and source quality. The most ideal reservoir and source is the siliceous- clay-rich facies that has a low carbonate content. In this facies reservoir and source quality decrease as carbonate content increases. Although not typical for carbonate facies to be associated with poor reservoirs, carbonate-rich Wolfcamp intervals exhibit poor reservoir quality and can be explained by extensive, heavy carbonate cement destroying original porosity in these facies. Facies that have primary compositions of quartz, feldspars, and clays lack carbonate cement and thus are able to preserve original porosity. In siliceous- clay-rich facies, organic matter hosted pores are also preserved by lack of carbonate cement, consequently allowing for high source potential. Although siliceous- clay-rich facies have high reservoir and source quality, it should be noted that if clay content is too high (>35%) ductility concerns could make these facies difficult to stimulate via hydraulic fracturing. This is not evident as samples tested had clay contents of 24%.

Aside from the most ideal facies, the packstone and grainstone facies in the Wolfcamp B stratigraphic unit can develop high secondary porosity associated with dissolution vugs. Also, carbonate mudstone facies often have heavy fracturing due to their stiffness associated with lack of clay content. These fractures create large amounts of secondary porosity and highly preferential hydrocarbon migration pathways. When hydrocarbons are able to migrate into these zones of vuggy porosity and fracture porosity, these carbonates could make for fair to high quality hydrocarbon reservoirs.

In addition to the facies effect on reservoir quality, there is an oil-wet or intermediate-wet tendency throughout the Spraberry and Wolfcamp intervals that affects reservoir quality as well.

Although a single wettability does not necessarily encompass an entire facies wettability, intermediate-wet zones tend to have higher reservoir quality than oil-wet zones due to abilities of both hydrophobic oil fluids and hydrophilic water fluids to flow at a similar rate. In more oil-wet zones oil typically surrounds the grains and displaces the hydrophilic water thereby having higher relative permeability and flowing more easily.

5-8 Sources of Error

Lack of Solvent Cleaning

Samples did not undergo any form of solvent cleaning to remove residual fluids before testing porosity and permeability other than heating to 60°C. Lack of cleaning could result in underestimated values of total porosity and permeability. Over estimations of tortuosity in samples due to residual fluid still being present can take up existing pore space. However, current tests on as-received samples do reflect reservoir conditions, apart from some evaporation of light hydrocarbons and wettability modification due to being stored in laboratory conditions. In addition, solvent used for sample cleaning is toluene and DT2 used in experiments for this study is 67% toluene. So, it is possible that porosity measurement from vacuum-assisted FIP in DT2 may have partially cleaned the sample resulting in a more accurate edge-accessible porosity measurement, although no heating element was involved. Also, solvent cleaning can change the wettability of samples, so it is beneficial to the wettability and connectivity tests that no solvent cleaning was performed. Nevertheless, some tests (such as porosity and permeability) on samples after solvent cleaning will be carried out in subsequent work.

Testing at Non-reservoir Pressure and Temperature Conditions

Samples were not tested at reservoir pressure or reservoir temperature. Since pressure and temperature at reservoir depth is much higher than testing conditions, rock property values may

not exactly represent reservoir properties. However, since only a few core studies do perform tests at reservoir conditions, if these results are skewed they should skew in a rather uniform manner and results should still be comparable to the majority of core studies. Finally, reservoir condition scaling factors can be used for more accurate reservoir properties and better property estimation in different pressures and temperatures.

Pyrolysis

During pyrolysis testing, clay minerals can convert bitumen to carbonaceous residue, which could cause an underestimation of hydrocarbon generation potential since under reservoir conditions, bitumen is expelled more easily (Waples, 1985).

MIP

Dictated by measurement principles, MIP tests will overestimate volume of smaller pores and underestimate volume of larger pores due to the ink-bottle effect. The ink-bottle effect occurs when larger pores are connected via small pore throats at the sample surface (Kaufman, 2010; Hu and Ewing, 2014). Larger pores can only be accessed when pressure is high enough to pass mercury through the initial small pore throat, thus giving much larger pore volumes at specific pressures. The MIP approach measures pore-throat size distribution, pore throats control hydrocarbon movement in the subsurface. Also, since minimum detection limits for MIP testing was 2.8 nm, a possible underestimation of porosity could occur in pores smaller than 2.8 nm. However, considering molecular sizes of petroleum products at 0.5-10 nm, smaller than 2.8 nm pore-throat sizes do not play an important role in oil movement.

Shale Representation

There is poor representation of clay-rich laminated shales for the Wolfcamp intervals in this study due to many tests involving reduction of plug sized samples to 1 cm^3 cubes. Often

times, when this facies is cut, the sample broke apart and cubes were not salvageable. This suggests that many of "shales" that underwent the full suite of tests were composed of clay-sized carbonate grains and skeletal material forming wackestones, mudstones, and micrite. Although more extensive testing should be conducted on clay-rich laminated shale facies, before sample cutting, all samples, including clay-rich laminated shale facies, were tested using vacuum-assisted FIP in DI water for porosity and density values.

Sample Mixing

Although cleaning of equipment used in grinding and sieving process was carefully carried out between samples, it is still possible that some slight sample mixing occurred skewing results in tests on sample sizes from GRI+ to powder.

Human Error and Misidentification

Although significant attention to detail took place during experimentation, possible human error took place when testing and recording data, which can result in skewed data points. To remedy this possibility, multiple test runs were often conducted.

Chapter 6: Conclusions and Recommendations

6-1 Conclusions

Samples were chosen that encompass various facies within the Lower Spraberry and Wolfcamp intervals in the Midland Basin to study petrophysical and geochemical properties to better understand how facies affect reservoir quality and source potential. In addition to this main goal, results from different testing methods were compared. Findings from the study are summarized below:

- Various sample compositions and facies were lumped into three groups.
  - Siliceous- clay-rich

        - Quartz as well as clay forming feldspars were deposited during lowstands by channel fan complexes or windblown sediment in distal portions of the basin.
    - Packstone and grainstone
        - Formed during highstand reef and carbonate development periods, then redeposited in lowstands by gravity flows/grain flows and turbidity currents.
    - Carbonate mudstone and wackestone
        - Deposited by distal portions of turbidity currents and hemipelagic material.
- Neither formation interval nor basin location have much effect on which facies has high reservoir and source quality.
- Ideal reservoir and source in the Lower Spraberry and Wolfcamp intervals is the siliceous-clay-rich mudstone.
- Reservoir and source quality decrease as carbonate content increases, maybe due to extensive, heavy carbonate cement destroying original porosity.
- Although quality decreases with increasing carbonate content, the packstone and grainstone facies in the Wolfcamp B stratigraphic unit can occasionally develop a high secondary porosity associated with dissolution vugs.
- Carbonate wackestone/mudstone facies can have high secondary porosity from fracturing.
- Lower Spraberry and Wolfcamp intervals are oil-wet to intermediate-wet.
- TOC and porosity decrease as carbonate content increases, and increase as quartz+feldspar and clay content increase.
- XRD-derived percent carbonate matches well with TOC-derived percent carbonate.
- XRD results do not match well with well log mineral volume curves.

- TOC and pyrolysis show the Wolfcamp Shale is a thermally mature formation that is oil-prone.
- TOC results match Schmoker equation log curve.
- Organic matter hosted pores contributing to total porosity, exhibited by porosity increasing as TOC increases.
- MIP and vacuum-assisted FIP porosity and density results match well, while MIP and DT2 FIP match the best.
- Measured well log porosity curves overestimate porosity, but corrected porosity curves moderately match laboratory porosity results.
- Matrix permeability increases as porosity increases.
- MIP permeability results did not match Timur equation estimations for permeability.
- Laboratory density results match the bulk density log curve well.
- Well logs corroborate heterogeneity in the Wolfcamp intervals. Due to heterogeneity and low porosity, there are no continuous pay intervals, but there are numerous, smaller isolated pay intervals with relatively low porosity potentially accessed via hydraulic fracturing.

Based on these findings, the most optimal drilling targets for the Lower Spraberry and Wolfcamp intervals would be those with low carbonate content.

6-2 Recommendations for Future Work

To further and better evaluate Spraberry and Wolfcamp Shale intervals, a larger sample range is necessary. Also, implementing solvent cleaning and conducting more testing using helium gas expansion and NMR. SEM and petrographic thin section studies would also increase the data quality by allowing for a better determination of pore type. Three wells are not enough to classify the entire Midland Basin, especially for heterogeneous intervals of the Wolfcamp

Shale. Adding more wells and more core data laterally, as well as adding more sample points within each facies vertically, would vastly improve reliability of results. In addition to more samples, future plug sized samples should be evaluated by using helium gas expansion to evaluate porosity and permeability results and compare against MIP. Furthermore, plugs should be cleaned of residual fluids before testing. Cubes used in vacuum-assisted FIP and MIP should also be cleaned using a solvent cleaning technique prior to testing. However, cubes used in contact angle and imbibition experiments should not be cleaned in order to preserve wettability characteristics. In order to evaluate fracture-prone shale samples, sieve size fractions should be tested for a variety of properties. NMR testing would add a valuable data set to existing data to compare results and achieve reliable data. Evaluating petrographic thin sections could help determine cementation properties in carbonate rich samples. Also, as Stolz (2014) suggested for the Avalon Shale, looking into diagenetic history of carbonate deposits could be beneficial for formation evaluation. Understanding the diagenetic history can help determine where the most prone locations for vuggy porosity are and where there is a lack of carbonate cement. Lastly, an in-depth lithofacies determination based on well logs and compared to core-identified facies would help with lateral facies correlations and mapping, eventually determining the extent of various facies and thus reservoir sweet spots.

Appendix A

Laboratory Methods and Procedures for X-Ray Diffraction Analysis at Shimadzu Center for Environmental, Forensics, and Material Science

Standard Operating Procedure

MaximaX XRD-7000: Shimadzu X-ray Diffractometer

Sample Preparation:

- Prepare your sample by compacting the sample into the sample holder using a glass slide
- Avoid vertical loading by removing excess sample with the edge of the glass slide
- Attempt to make your sample as flat and homogenous as possible; once this is completed your sample is ready to be analyzed.

Power Operations: *IF THE CHILLER AND XRD ARE ALREADY ON CONTINUE TO STEP 3*

- Turn the chiller on by pressing the power button (on the face of the chiller), a green light will illuminate.
    - Allow the chiller to sit for ~20 minutes to adjust to the proper temperature.
- Turn the XRD on by pressing the power button on the left hand side. The green power button will illuminate on the front panel of the XRD.

XRD Calibration:

- Locate and open the [PCXRD] program on the desktop. The main "XRD-6100/7000" panel will display.
- Click the [Display and Setup] icon, a "door alarm check" window will pop up. Follow the prompt to open and close the XRD door, once complete click "Close". An "IOcon" window will pop up with the message "Now Calibration! If ready OK", Click "OK".
- The XRD is officially calibrated and ready to process your sample.

Setting Analysis Conditions:

To set the processing conditions go to the "XRD 6100/7000" panel.

- Click on the [Right Gonio Condition] icon to open the [Analysis Condition Edit Program] window
- Click the blue bar under [Measurement Mode: Standard] to open the [Standard Condition Edit] window.
- Most of the settings in the [Standard Condition Edit] window will be preset. Only a few conditions will need to be changed.
- The following general condition settings will work for a wide array of materials.

**It's very important to follow these next steps, double check any settings you change ensuring to follow these guidelines precisely. This will minimize minor mistakes when processing materials and will prevent damage to the detector*.*

- Scanning condition: Scan Range (deg) = 2°-70°
- Optional Condition: Check the box [Option Enable]
- Beta Attachment: Control Mode: *Rotation*
  Rotation Speed (rpm): 6
- Slit Condition: Slit Conditions are preset, and must be verified on the XRD to ensure the proper slit sizes match the settings listed under the Slit Conditions.
    - Checking the Slits:
        - Open the XRD door, on the left side of the XRD is the X-ray tube, the Divergence Slit is attached to the left side of the divergence soller slits.

        - On the right hand side will be the detector arm which contains a set of Scattering soller slits, the Scattering Slit faces the sample (Left) and the Receiving Slit faces the detector (Right).
        - If they are not the same sizes as what is preset in the [Slit Condition] box change the slit's so they do match.
    - *Standard Slit Settings:*
        - Divergence Slit: 1.0°
        - Scattering Slit: 1.0°
        - Receiving Slit: 0.3 mm
- Double check your settings and make sure they are correct, if they are click [OK].
- A [File & Sample Condition Edit] window will display; change the [Group name] to match your destination folder name and change [File name] and [Sample Name] to match your sample name, click [New].
    - Later samples can be created by simply changing the file and sample names and clicking [Modify].
- Click [Close] on the [Standard Condition Edit] window.

Starting the XRD Processing:

- Locate and click the [Right Giono Analysis] icon on the [XRD-6100/7000] panel.
- Your current sample name should appear highlighted blue in the upper portion of the [Right Gonio System: AnalysisCondition Edit Program] window. Highlight your sample and click [Append], this adds your sample to the list in the bottom portion of the window labeled [Entry for Analysis], click [Start].
- Your sample should appear in the bottom of the [Right Giono Analysis & Spooler Program] window, click [Start] in this window. This officially starts the analysis process.
    - Indicators for Analysis: A clicking sound will come from the XRD when the locking mechanism on sliding door locks. On the face of the XRD a yellow light should illuminate under [X-RAYS ON].
- Leave all software windows open and allow the XRD to process your sample, this should take ~30 minutes.

Completed XRD Processing:

- A complete peak spectrum should appear in the [Right Giono Analysis & Spooler Program] window upon completion.
- The green [Analyzing!] Box should disappear and the yellow [X-RAYS ON] light should turn off.
- If you have more samples to analyze, continue to run your samples in the same manner listed above.

Opening Peak Profile Spectrum:

- Locate and open the icon for the [MDI jade 9] software on the Desktop.
- Under [file], click [Read], locate the folder [xddat] under [favorites]. Locate the folder where your samples are saved.
- In your folder, each sample should have a [.RAW] file, use this file to open your selected spectrum in the [Jade 9] software.

Identifying Minerals in Peak Spectrum:
It's important to have an educated background on the sample you're analyzing. Knowledge regarding the bulk composition and what you're searching for will greatly reduce the amount of time spent IDing the various peaks in the spectrum.

- Locate the [Find Peaks] icon on the main tool bar next to the [Floppy Disk/Save] icon, this will identify and mark any statistically significant peaks within the spectrum
- Choose a mineral database: At the top of the panel to the right of the spectrum window, there will be a drop down menu choose the [RDB-Minerals] as the database. The RDB-Mineral database should be predominately used to identify most minerals in your spectra.
    - *If you cannot find a mineral in the RDB-Minerals database change to the [PDF+4 Minerals] database library, but be sure to change back to the RDB database once the mineral is located.*
- Begin searching for minerals based on your pre-existing knowledge regarding the sample. When you identify minerals that fit your peak spectrum hit [Enter] on the keyboard, this process will add the minerals to a compiled list of those minerals which you identified in the spectrum.
- Once you have exhausted your initial hypothetical list of minerals, a helpful tool to use is the [Line Based Search/Match]. Go to the main tool bar and locate [Identify] and select the [Line Based Search] option.
    - *This tool will compile a list of minerals by searching a selected PDF database for entries with peaks which are statistical matches for the peaks identified within your spectrum.*
    - Settings:
        - [Two-Theta Error Window] max setting should be no more than 0.24%
        - [Top Hits to List] max setting 80
    - Set the parameters and click the blue [Play] icon next to the [X] to run the search and generate a list of possible phases that might fit your spectra. **Note: the line based search should not be used as a primary way to identify the bulk mineral mode of the sample as the software is not consistent when generating phases and will possibly leave out important phases for the spectrum**.*

Model Analysis:

- Once all minerals have been ID'd, check that they have been added to the mineral list by pushing [Enter] on the keyboard.
- Click the [%] icon next to the drop-down mineral list located on the toolbar in the middle of the window to begin modal analysis.
    - An overlay will appear with different chart configurations of the modal results, to change the configurations of the chart use the drop down menu in the chart window.
- To view the modal analysis in text format: locate and click the […] icon near the [%] icon. This will list the minerals by name, chemical formula, and the normalized weight percent for each mineral. It will also state if the mineral is a [major], [minor], [trace], or [absent] component in the sample.
- If you would like to remove a mineral from your mineral list at any time, highlight the mineral and press [Delete] on the keyboard. [Absent] phases should be removed from the list by this method.

Analysis Check with Pattern Deconvolution:

- A key indication that the peak spectrum has been fully fitted and identified is by using the [Pattern Deconvolution] tool which automatically runs with the modal analysis.
    - The pattern deconvolution tool will generate a red overlay spectrum on top of the original white spectrum.
    - This process is generating a [Best Fit Profile] composed of the selected mineral standards from the [Mineral PDF database library] with your sample spectrum.
    - If all minerals have been properly identified, then the red deconvolution overlay will match the peak spectra for each peak. If there are peaks that don't have the red deconvolution overlay then those peaks have not been identified.
- Continue processing your spectrum until your original spectra and the deconvolution spectra match.

Saving Data:

To save your data,

- Go to [file] and [Save], save your data under [Current work as *.SAV]. This will save all analysis as a separate file.

Appendix B

Laboratory Methods and Procedures for Total Organic Carbon Analysis at GeoMark Research

Standard Operating Procedure

LECO C230: GeoMark Total Organic Carbon Instrument

Sample Requirements for a Typical Geochemical Program:

- For geochemical analysis a teaspoon (ca., 10 g) of sample material is needed when TOC, Rock-Eval, vitrinite reflectance and residual hydrocarbon fluid fingerprinting is to be completed. If possible, a tablespoon is preferred. However, it is possible to complete a detailed program with even less sample, although there is dependent on the sample characteristics (e.g., organic richness, abundance of vitrinite, amount of staining). Sample prep includes grinding the sample with mortar and pestle until it passes through a 60-mesh sieve.

Total Organic Carbon (TOC) – LECO C230 instrument:

- Leco TOC analysis requires decarbonation of the rock sample by a treatment with hydrochloric acid (HCl). This is done by treating the samples with concentrated HCl for at least two hours. The samples are then rinsed with water and flushed through a filtration apparatus to remove the acid. The filter is then removed, placed into a LECO crucible and dried in a low temperature oven (110^{o}C) for a minimum of 4 hours. Samples may also be weighed after this process in order to obtain a % carbonate value based on weight loss.
- The LECO C230 instrument is calibrated with standards having known carbon contents. This is completed by combusting these standards by heating to 1200^{o}C in the presence of oxygen. Both carbon monoxide and carbon dioxide are generated, and the carbon monoxide is converted to carbon dioxide by a catalyst. The carbon dioxide is measured by an IR (infra-red) cell. Combustion of unknowns is then completed and the response of unknowns per mass unit is compared to that of the calibration standard, thereby the TOC is determined.
- Standards are analyzed as unknowns every 10 samples to check the variation and calibration of the analysis. Random and selected reruns are done to verify the data. The acceptable standard deviation for TOC is 3% variation from established value.

Turnaround Time:

- The standard turnaround time for sample orders over the past 12 months is approximately 2 to 3 weeks, depending on number of samples in the order.

Appendix C

Laboratory Methods and Procedures for Pyrolysis Analysis at GeoMark Research

Standard Operating Procedure

Rock Eval or HAWK: GeoMark Pyrolysis Instrument

Sample Requirements for a Typical Geochemical Program:

- For geochemical analysis a teaspoon (ca., 10 g) of sample material is needed when TOC, Rock-Eval, vitrinite reflectance and residual hydrocarbon fluid fingerprinting is to be completed. If possible, a tablespoon is preferred. However, it is possible to complete a detailed program with even less sample, although there is dependent on the sample characteristics (e.g., organic richness, abundance of vitrinite, amount of staining). Sample prep includes grinding the sample with mortar and pestle until it passes through a 60-mesh sieve.

Rock Eval / HAWK Pyrolysis:

- Approximately 100 milligrams of washed, ground (60 mesh) whole rock sample is analyzed in the Rock-Eval or HAWK instrument. Organic-rich samples are analyzed at reduced weights whenever the S2 value exceeds 40 mg/g or TOC exceeds 7-8%. Samples must be re-analyzed at lower weights when these values are obtained at 100 mg.

RE-II Operating Conditions:

- S1: 300^{o}C for 3 minutes
- S2: 300^{o}C to 550^{o}C at 25^{o}C/min;
  hold at 550^{o}C for 1 minute
- S3: trapped between 300 to 390^{o}C

RE-VI Operating Conditions:

- S1: 300^{o}C for 3 minutes
- S2: 300^{o}C to 650^{o}C at 25^{o}C/min;
  hold at 650^{o}C for 0 minute
- S3: measured between 300 to 400^{o}C

HAWK Operating Conditions:

- S1: 300^{o}C for 3 minutes
- S2: 300^{o}C to 650^{o}C at 25^{o}C/min;
  hold at 650^{o}C for 0 minute
- S3: measured between 300 to 400^{o}C

Measurements from Rock-Eval are:

- S1: free oil content (mg HC/g rock)
- S2: remaining generation potential (mg HC/g rock)
- T_{max}: temperature at maximum evolution of S2 hydrocarbons (^{o}C)
- S3: organic carbon dioxide yield (mg CO_2/ g rock)

Several useful ratios are also utilized from Rock-Eval and TOC data. These are:

- Hydrogen Index (HI): S2/TOC × 100 (in mg HC/g TOC)
- Oxygen Index (OI): S3/TOC × 100 (in mg CO_2/g TOC)
- Normalized Oil Content: S1/TOC × 100 (in mg HC/g TOC)
- S2/S3:
- Production Index (PI): S1/ (S1+S2)

Instrument calibration

- Achieved using a rock standard. Its values were determined from a calibration curve to pure hydrocarbons of varying concentrations. This standard is analyzed every 10 samples as an

unknown to check the instrument calibration. If the analysis of the standard ran as an unknown does not meet specifications, those preceding data are rejected, the instrument recalibrated, and the samples analyzed again. However, normal variations in the standard are used to adjust any variation in the calibration response. The standard deviation is considered acceptable under the following guidelines:

  - T_{max}: $\pm 2^{o}C$
  - S1: 10% variation from established value
  - S2: 10% variation from established value
  - S3: 20% variation from established value

- Analytical data are checked selectively and randomly. Selected and random checks are completed on approximately 10% of the samples. A standard is analyzed as unknown every 10 samples.

Turnaround Time:

- The standard turnaround time for sample orders over the past 12 months is approximately 2 to 3 weeks, depending on number of samples in the order.

Appendix D

Core Slab and Core Plug Photos

Sample photos showing core slab intervals on left with blue pen for scale as well as pointing to the approximate plug point (unless corrected by red arrow), and core plug photos upon arrival to UTA lab on right with a ruler for scale.

1) ME-8004

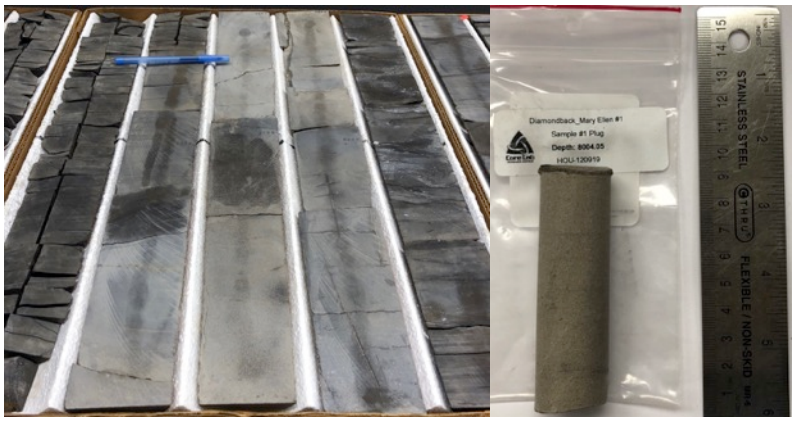

2) ME-8027

3) ME-8045

4) ME-8063

5) ME-8435

6) ME-8444

7) ME-8455

8) ME-8463

9) ME-8621

10) ME-8633

11) ME-8832

12) ME-8852

13) ME-8866

14) ME-9031

15) ME-9039

16) ME-9044

17) ME-9052

18) ME-9207

19) ME-9197

20) ME-9509

21) ME-9511

22) ME-9528

23) ST-8441

24) ST-8877

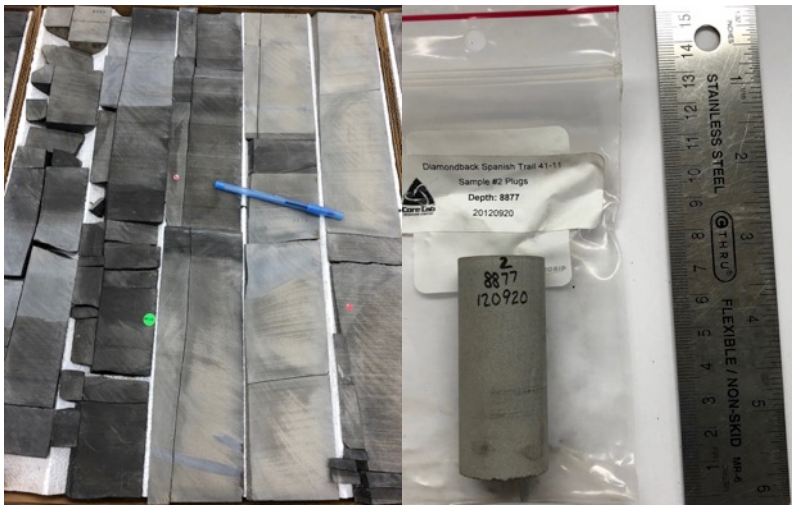

25) ST-9400

26) ST-9605

27) ST-9612

28) ST-9632

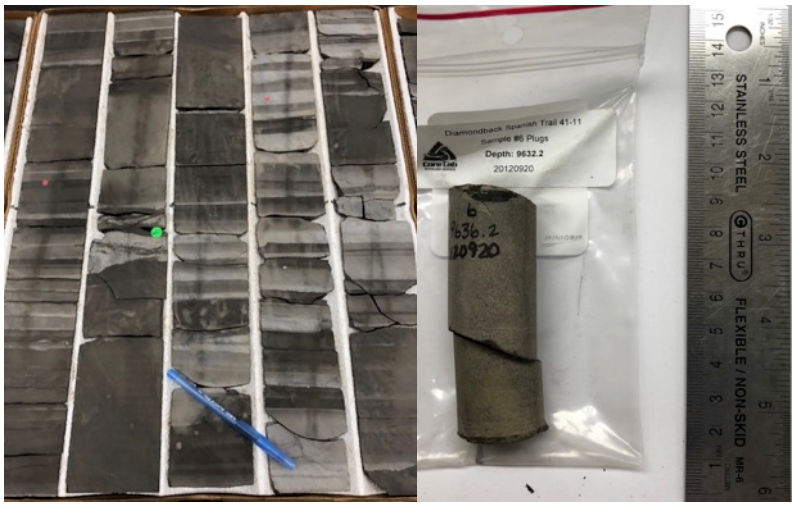

29) ST-9833

30) ST-9841

31) ST-9849

32) ST-10053

33) ST-10067

34) ST-10310

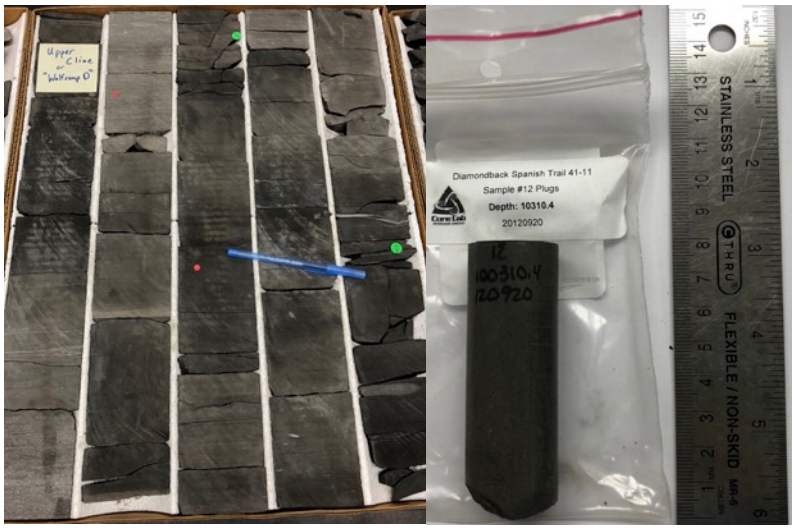

35) ST-10318

36) ST-10322

37) JB-9187

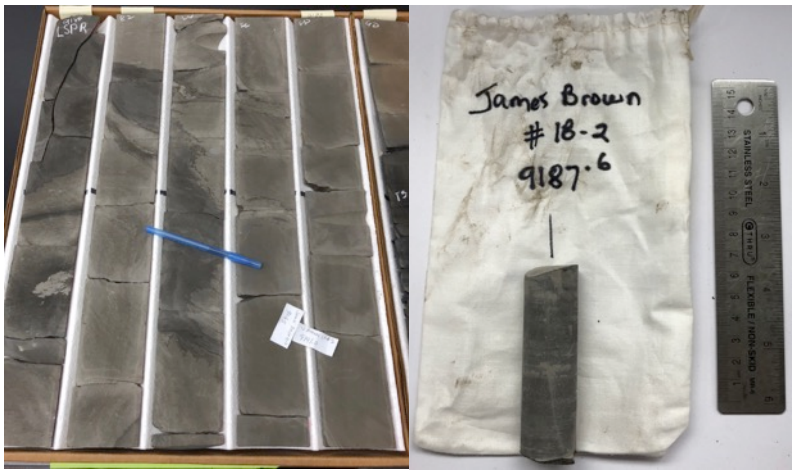

38) JB-9209

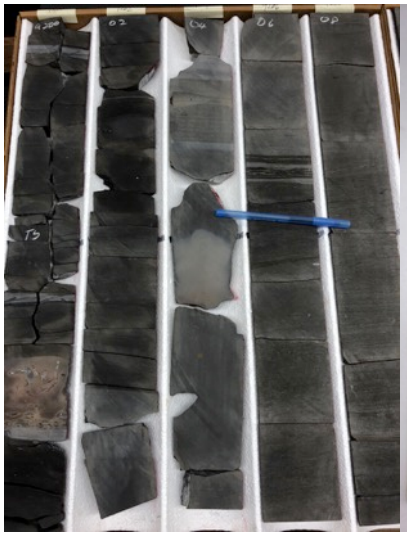

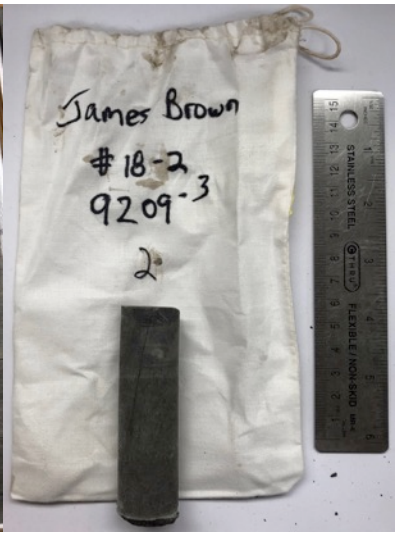

39) JB-9733

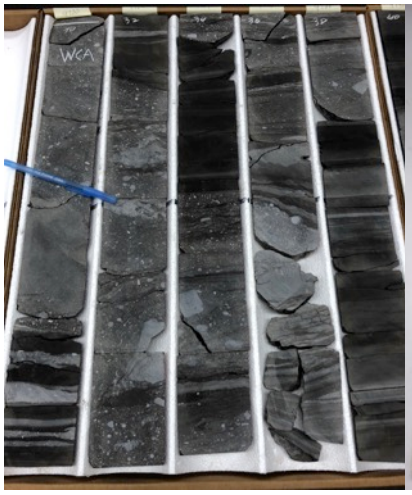

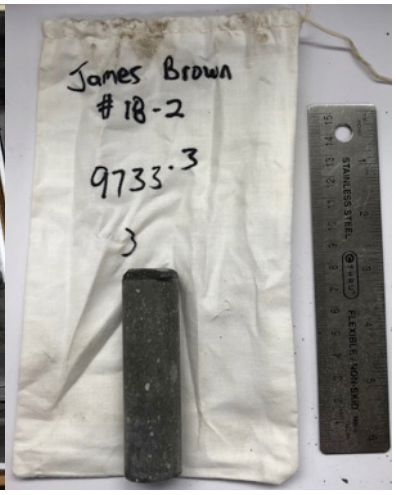

40) JB-9781

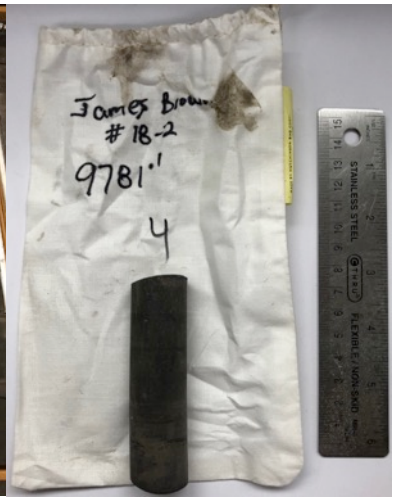

41) JB-9849

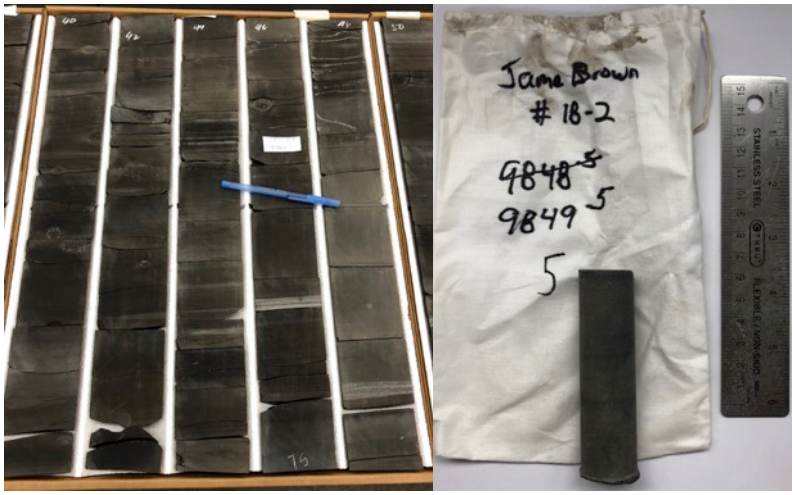

42) JB-9867

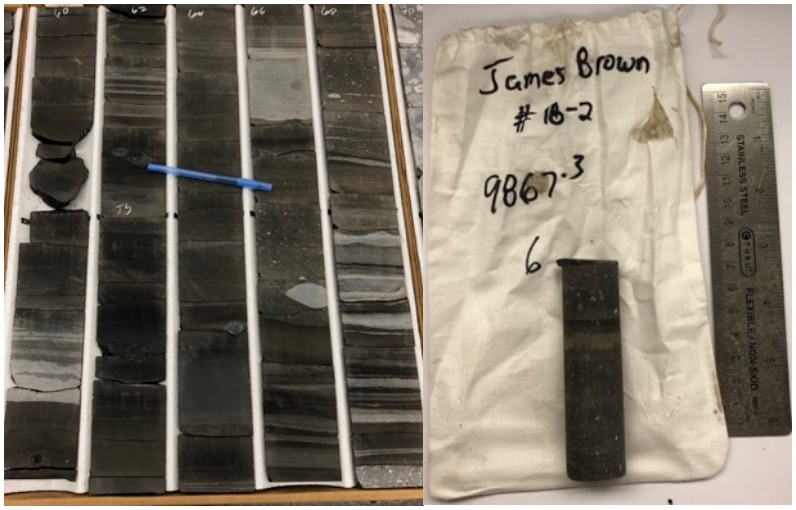

43) JB-9871

44) JB-9891

45) JB-9904

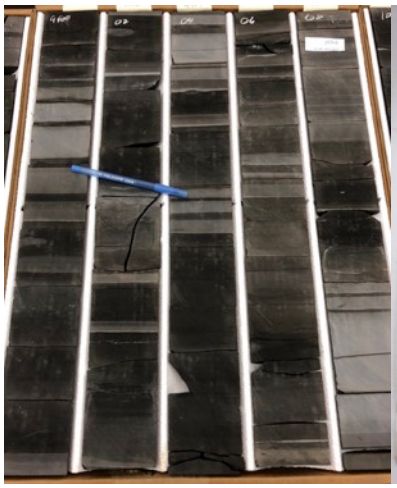

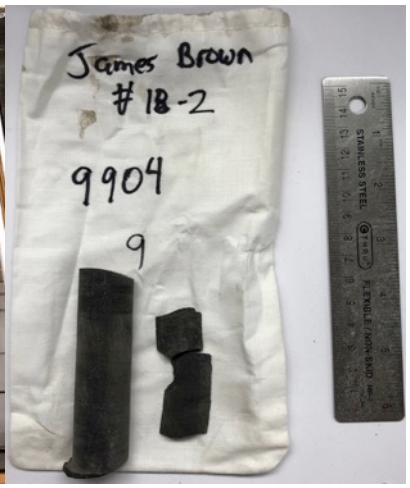

46) JB-10525

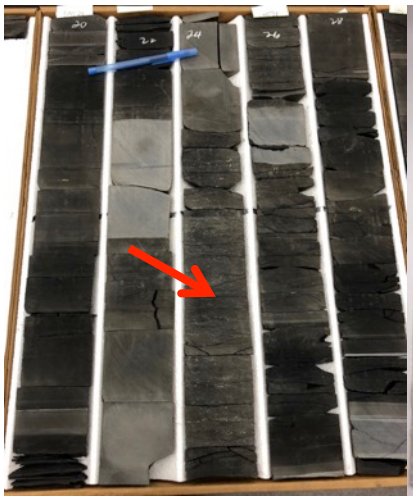

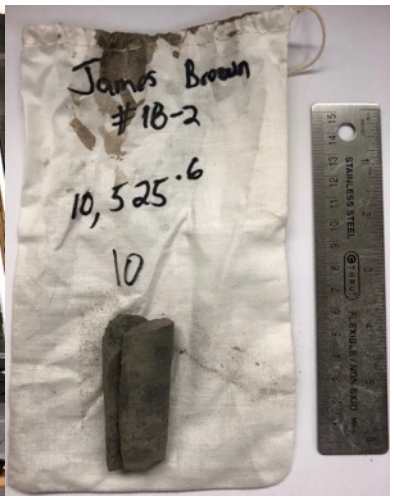

47) JB-10570

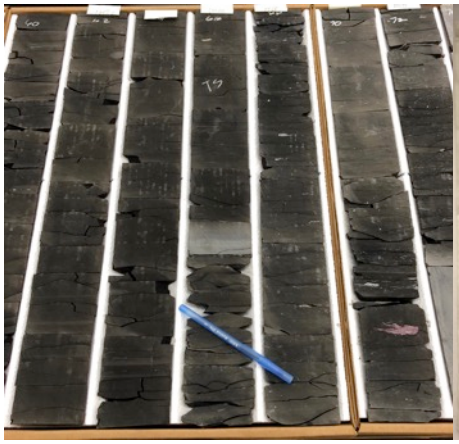

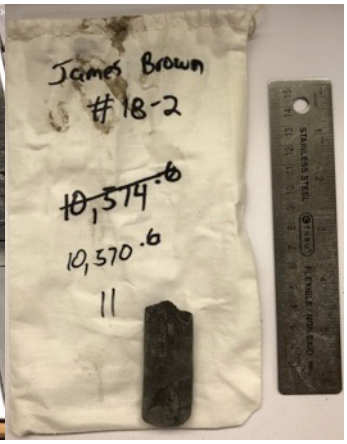

48) JB-10595

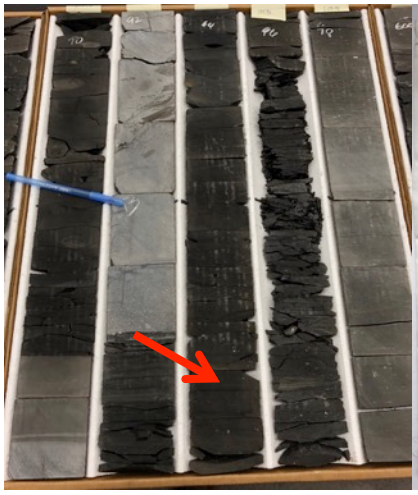

References

Abramov, A., Mlada, S. 2017. Midland Basin: Wolfcamp Target Benches. Shale Newsletter. https://www.rystadenergy.com/newsevents/news/newsletters/UsArchive/shale-newsletter-july-2017/. Accessed on September 20, 2019.

Agbalaka C., Dandekar, A.Y., Patil, S.L., Khataniar, S., Hemsath, J.R. 2008. The effect of wettability on oil recovery: A review, Paper presented at the SPE Asia Pacific Oil and Gas Conference and Exhibition 2008 – "Gas Now: Delivering on Expectations;" Perth, Western Australia, Australia. 1. pp. 73-85.

Alnaji, N.S. 2002. Two carbonate shelf margins with hydrocarbon potential compared: Upper Jurassic Formations of Arabian Basin and Guadalupian Formations of Permian Basin of Texas and New Mexico. University of South Carolina, SEPM Strata. http://www.sepmstrata.org/page.aspx?&pageid=137&4. Accessed on September 24, 2019

American Petroleum Institute. 1998. RP-40 Recommended practices for core analysis section. In API Recommended Practice (2rd ed.). Washington, D.C: API Publishing Services.

Archie, G.E. 1942. The electrical resistivity log as an aid in determining some reservoir characteristics. Journal of Petroleum Technology. 5: 54-62.

Asquith, G. 2010. Petrophysics of gas-bearing shales. Texas Tech. University-Advanced Petrophysics Course Manual.

Baumgardner, R.W., Hamlin, H.S., Rowe, H.D. 2014. High-Resolution Core Studies of Wolfcamp/Leonard Basinal Facies, Southern Midland Basin, Texas. AAPG Search and Discovery Article #10607. http://www.searchanddiscovery.com/documents/2014/10607baumgardner/ndx_baumgardner.pdf.

Beaumont, C. 1981. Foreland basins, Geophysical Journal of the Royal Astronomical Society. v. 65, p. 291 -329.

BEG. Bureau of Economic Geology, The University of Texas at Austin. 2019. Wolfberry and Spraberry Play of the Midland Basin, Project STARR. http://www.beg.utexas.edu/research/programs/starr/unconventional-resources/wolfberry-spraberry. Accessed on September 24, 2019.

Bhuyan, K., Passey, Q.R. 1994. Clay Estimation from Gamma Ray and Neutron- Density Porosity Logs.

Blakey, R. 2011. Paleogeography of Southwestern North America. http://deeptimemaps.com/southwest-north-america-map-list/. Accessed on September 13, 2019.

Blomquist, P. K. 2016. Wolfcamp Horizontal Play Midland Basin, West Texas. IHS Geoscience Webinar Series.

Cai, J., Hu, X., Standnes, D. C., and You, L. 2012. An analytical model for spontaneous imbibition in fractal porous media including gravity. Colloids and Surfaces A: Physicochemical and Engineering Aspects. 414: 228-233. doi:10.1016/j.colsurfa.2012.08.047.

Chukwuma, F. 2015. Nanopetrophysics of the Utica Shale, Appalachian Basin, Ohio, USA. M.S. Thesis, Department of Science, University of Texas at Arlington, USA.

Crain, E.R. 1978. The Rock-Fluid Model for Petrophysical Analysis in Crain's Petrophysical Handbook. https://www.spec2000.net/01-rockfluidmodel.htm.

Crowe, C.W. 1969. Method of lessening the inhibitory effects to fluid flow due to the presence of solid organic substances in a subterranean formation.

Cui, X., Bustin, A. M. M., & Bustin, R. M. 2009. Measurements of gas permeability and diffusivity of tight reservoir rocks: Different approaches and their applications. Geofluids. 9(3), 208–223.

Dane, J., C.G. Topp, A.L. Flint, L.E. Flint. 2002. 2.2 Particle Density. DOI: 10.2136/sssabookser5.4.c10.

DrillingInfo. 2019. Found at https://www.enverus.com. Accessed on September 18, 2019.

Dutton, S. P. 2008. Calcite cement in Permian deep-water sandstones, Delaware Basin, west Texas: Origin, distribution, and effect on reservoir properties. AAPG Bulletin. v. 92, p. 765–787. doi:10.1306/01280807107.

EIA. 2018. Permian Basin, Wolfcamp Shale Play Geology review, U.S. Energy Information Publication report. https://www.eia.gov/maps/pdf/PermianBasin_Wolfcamp_EIAReport_Oct2018.pdf, Accessed on September 18, 2019.

EIA. 2019. Permian Basin, Wolfcamp and Bone Spring Shale Plays Geology review, U.S. Energy Information Publication report. https://www.eia.gov/maps/pdf/Wolfcamp_BoneSpring_EIA_Report_July2019.pdf, Accessed on September 24, 2019.

Ewing, T. E. 1991, The tectonic framework of Texas: Text to accompany "The Tectonic Map of Texas". Austin, Bureau of Economic Geology, The University of Texas at Austin. 36 pp.

Fellah, Z.E.A., Berger, S., Lauriks, W., Depollier, C., Aristégui, C., Chapelon, J.-Y. 2003. Measuring the porosity and the tortuosity of porous materials via reflected waves at oblique incidence. J. Acoust. Soc. Am. 113, 2424–2433. doi:10.1121/1.1567275.

Fielding, C.R., Frank, T.D. & Isbell, J.L. 2008. The late Paleozoic ice age—A review of current understanding and synthesis of global climate patterns, in Fielding, C.R., Frank, T.D. & Isbell, J.L., eds., Resolving the Late Paleozoic Ice Age in time and space: Geological Society of America Special Paper no. 441,343-354.

Galley, John E. 1958. Oil and Geology in the Permian basin of Texas and New Mexico: North America: Habitat of Oil. AAPG Special Volume, 395-446.

Galloway, W.E., T.E. Ewing, C.M. Garrett, N. Tyler, and D.G. Bebout. 1983. Atlas of major Texas oil reservoirs. The University of Texas at Austin, Bureau of Economic Geology Special Publication. 139 pp.

Gao, Z.Y., and Hu, Q.H. 2013. Estimating permeability using median pore-throat radius obtained from mercury intrusion porosimetry. Journal of Geophysics and Engineering, 10, 025014. DOI:10.1088/1742-2132/10/2/025014.

Gao, Z.Y., & Hu, Q.H. 2016. Initial water saturation and imbibition fluid affect spontaneous imbibition into Barnett shale samples. Journal of Natural Gas Science and Engineering, 34: 541–551.

Gao, Z.Y., & Hu, Q.H. 2016. Wettability of Mississippian Barnett Shale samples at different depths: Investigations from directional spontaneous imbibition. AAPG Bulletin, 100(1): 101–114.

Gardner, S.P., McDonough, K.-J., Lieber, R., Vogler, R., Cook, S., Pollachek, M. 2017. Uniting Petrophysics and Stratigraphy to Decipher Classified Facies from a Pre-Stack 3D Inversion: Wolfcamp and Spraberry, Howard County, Midland Basin. Search and Discovery Article #10946.

Gardiner, W.B. 1990. Fault fabric and structural subprovinces of the Central basin Platform: A model for strike - slip movement, in Flis, J. E., and Price. R. C., eds., Permian basin Oil and Gas Fields: Innovative Ideas in Exploration and Development: Midland. West Texas Geological Society. 90-87, p. 15-27.

Gaswirth, S.B., Marra, K.R., Lillis, P.G., Mercier, T.J., Leathers-Miller, H.M., Schenk, C.J., Klett, T.R., Le, P.A., Tennyson, M.E., Hawkins, S.J., Brownfield, M.E., Pitman, J.K., and Finn, T.M. 2016. Assessment of undiscovered continuous oil resources in the Wolfcamp shale of the Midland Basin, Permian Basin Province, Texas, 2016: U.S. Geological Survey Fact Sheet 2016–3092, 4 p. https://doi.org/10.3133/fs20163092.

Ghanbarian, B., Hunt, A.G., Ewing, R.P., and Sahimi, M. 2013. Tortuosity in porous media: A critical review. Soil Sci. Soc. Am. J. 77. 1461– 1477.

Hager, J. 1998. Steam drying of porous media. Ph.D. Thesis, Department of Chemical Engineering, Lund University, Sweden.

Hamlin, H.S. & Baumgardner, R.W. 2012. Wolfberry (Wolfcampian-Leonardian) deep-water depositional systems in the Midland Basin: Stratigraphy, lithofacies, reservoirs, and source rocks: Report of Investigations 277. Bureau of Economic Geology, The University of Texas at Austin. 61 pp.

Hamlin, H.S., Baumgardner, R.W. 2012. Wolfberry Play, Midland Basin, West Texas. Search and Discovery.

Hanford, C.R. 1981. Coastal sabkha and salt pan deposition of the lower Clear Fork Formation (Permian), Texas. Journal of Sedimentary Petrology. v. 51, p. 761-778.

Heckel, P.H. 1986. Sea-level curve for Pennsylvanian eustatic marine transgressive-regressive depositional cycles along midcontinent outcrop belt, North America. Geology, 14: 330-334.

Hills, J. M. 1985. Structural evolution of the Permian basin of west Texas and New Mexico, in Dickerson, P. W., and Muehlberger, W. R., eds., Structure and Tectonics of Trans-Pecos Texas: Midland, West Texas Geological Society. 85-81. pp. 89-99.

Holmes, M., Holmes, A. M., & Holmes, D. I. 2017. Mixed Reservoir Wetting in Unconventional Reservoirs and Interpretation of Porosity/Resistivity Cross Plots, Derived From Triple-Combo Log Data. Unconventional Resources Technology Conference. doi:10.15530/URTEC-2017-2668804.

Horak, R. L. 1985. Trans-Pecos Tectonism and its effect on the Permian Basin, In Dickerson, P.W. and Muehlberger, W.R., eds. Structure and Tectonics of Trans-Pecos Texas: West Texas Geological Society. Publication 81, 81-87.

Hu, Q.H., and Ewing, R.P. 2014. Integrated experimental and modeling approaches to studying the fracture-matrix interaction in gas recovery from Barnett Shale. Final Report, Research Partnership to Secure Energy for America (RPSEA), National Energy Technology Laboratory, Department of Energy. 91p.

Hu, Q.H., Ewing, R.P., and Dultz, S. 2012. Pore connectivity in natural rock. Journal of Contaminant Hydrology. 133: 76–83.

Hu, Q.H., Ewing, R.P., and Rowe, H.D. 2015. Low nanopore connectivity limits gas production in the Barnett Formation. Journal of Geophysical Research: Solid Earth. 120(12): 8073-8087.

Hu, Q.H., Persoff, P., and Wang, J.S.Y. 2001. Laboratory measurement of water imbibition into low-permeability welded tuff. Journal of Hydrology. 242(1-2): 64–78.

Hu, Q. H., Zhang, Y. X., Meng, X. H., Li, Z., Xie, Z. H., Li, M. W. 2017. Characterization of multiple micro-nano pore networks in shale oil reservoirs of Paleogene Shahejie

Formationin Dongying Sag of Bohai Bay Basin, East China. Petroleum Exploration and Development. 44(5): 720–730.

Jarvie, D.M. 2018. Petroleum Systems in the Permian Basin: Targeting Optimum Oil Production. Jarvie HGS Downtown Permian Basin Presentation. Houston, TX.

Jordan, T. E. 1981. Thrust loads and foreland basin development, Cretaceous western United States. AAPG Bulletin. 11, 65, p. 2506-2520.

Kantzas, A., Bryan, J., Taheri, S. n.d. Fundamentals of Fluid Flow in Porous Media.

Kao, C. S., and Hunt, J.R. 1996. Prediction of wetting front movement during one-dimensional infiltration into soils. Water Resources Research. 32: 55-64

Katz, A.J., and Thompson, A.H. 1986. A quantitative prediction of permeability in porous rock. Physical Review B. 34: 8179–81.

Katz, A.J., and Thompson, A.H. 1987. Prediction of rock electrical conductivity from mercury injection measurements. Journal of Geophysical Research. 92(B1): 599–607.

Kaufmann, J. 2010. Pore space analysis of cement-based materials by combined nitrogen sorption – Wood's metal impregnation and multi-cycle mercury intrusion. Cement and Concrete Composites. 32(7): 514–522.

Kibria, M.G., Q.H. Hu, H. Liu, Y. Zhang, J. Kang. 2018. Pore structure, wettability, and spontaneous imbibition of Woodford Shale, Permian Basin, West Texas. Marine and Petroleum Geology. 91: 735–748.

Kupchenko, C.L., Gault, B.W., and Mattar, L. 2008. Tight gas production performance using decline curves. CIPC/SPE Gas Technology Symposium 2008 Joint Conference, Presentation at the Society of Petroleum Engineers, Calgary, Alberta, Canada. 16 June, 2008. 978-1-55563-179-6.

Li, J., Lu, S., Chen, G., Wang, M., Tian, S., & Guo, Z. 2019. A new method for measuring shale porosity with low-field nuclear magnetic resonance considering non fluid signals. Marine and Petroleum Geology. 102: 535–543.

Löhr, S.C., Baruch, E.T., Hall, P.A. and Kennedy, M.J. 2015. Is organic pore development in gas shales influenced by the primary porosity and structure of thermally immature organic matter?. Organic Geochemistry. 87, pp.119-132.

Lopez, R., and A. 2007. Soria. Kinematical description of the spontaneous imbibition processes. WSEAS International Conference on Fluid Mechanics and Aerodynamics.

Loucks, R.G., R.M. Reed, S.C. Ruppel and D.M. Jarvie. 2009. Morphology, genesis, and

distribution of nanometer-scale pores in siliceous mudstones of the Mississippian Barnett Shale. Journal of Sedimentary Research. 79(11-12): 848-861.

Lu, S., Xue, H., Wang, M., Huang, W., Li, J., Xie, L., Liu, X. 2016. Several key issues and research trends in evaluation of shale oil. Acta Petrolei Sinica. 37(10), 1309–1322.

Ma, S., N.R. Morrow, X. Zhou, and Zhang. 1994. Characterization of Wettability from Spontaneous Imbibition Measurements. Western Research Institute - University of Wyoming.

Majeed, M.H. 2014. Static Contact Angle and Large Water Droplet Thickness Measurements with the Change of Water Temperature.

Mann, G. 2017. Petrophysical Properties of the Yeso, Abo and Cisco Formations in the Permian Basin in New Mexico, U.S.A. M.S. Thesis, the University of Texas at Arlington, USA.

Mazzullo, S.J. & Reid, A.M. 1989. Lower Permian platform and basin depositional systems, northern Midland basin, Texas, in Crevello, P.D., Wilson, J.L., Sarg, J.F. & Read, J.F., eds., Controls on carbonate platform and basin development: SEPM Special Publication 44, p. 305-320.

Micromeritics. 2001. Porosimetry brochure.

Morris, R.L. and Biggs, W.P. 1967. Using log-derived values of water saturation and porosity: Society of Professional Well Log Analysts, 8th Annual Logging Symposium, Transactions, Paper O.

Mzee, N. 2019. Nano-Petrophysical Study of the Wolfcamp, Dean, and Spraberry Formations of the Midland Basin. M.S. Thesis, the University of Texas at Arlington, USA.

Nelson, S. A. 2018. X-Ray Crystallography. https://www.tulane.edu/~sanelson/eens211/x-ray.htm. Accessed on October 5, 2019.

Oriel, S. S., Myers, A.D., Crosby, E. 1967. West Texas Permian basin region, in McKeeand, E. and Oriel, S., eds., Paleotectonic investigations of the Permian system in United States, U.S. Geological Survey Professional Paper 515-A, p. 21-64.

Page, L.R., Adams, E.J. 1940. Stratigraphy, Eastern Midland Basin, Texas. AAPG Bulletin, 24: 52–64.

Philip, J.R. 1957. The theory of infiltration: 4. Sorptivity and algebraic infiltration equations. Soil Science. 84: 257–265.

Pioneer Natural Resources. 2012. Permian Investor Presentation. http://media.corporate-ir.net/media_files/IROL/90/90959/MarchPermianInvestorPresentation.pdf. Accessed on Sep. 23 2019.

Pioneer Natural Resources. 2014. The Wolfcamp Shale Technical Learnings to Date and Challenges Going Forward. https://www.ryderscott.com/wp-content/uploads/RSC-2014-Reserves-Conference_01Flumerfelt.pdf. Accessed on Sep. 23 2019.

Quintero, R.P. 2016. Coupled Geochemical and Nano-Petrophysical Study of The Spraberry-Wolfcamp Trend West Texas, U.S.A. The University of Texas at Arlington.

Robinson, K. 1988. Petroleum geology and hydrocarbon plays of the Permian basin Petroleum province West Texas and southeast New Mexico, U.S. Geological Survey Open-File Report 88-450-Z, 53 p. https://doi.org/10.3133/ofr88450Z.

Rodriguez, C. 2017. Identifying new drilling areas in Midland Basin intergrating latest GIS buffering technology and geological mapping. IHS Energy.

Rodriguez, R., Crandall, D., Song, X., Verba, C., & Soeder, D. 2014. Imaging Techniques for Analyzing Shale Pores and Minerals. Morgantown, WV.

Roth, M., and Roth, M. 2018. Permian Stacked-Pay Potential Assessment Using Multi-Disciplinary Analytics. Search Discov. Artic. 11150. doi:10.1306/11150Roth2018.

Schlumberger. 2014. sCore Lithofacies Classification Reveals Barnett Shale Reservoir Quality.

Schlumberger Oilfield Glossary. 2018. Geopressure gradient - Schlumberger Oilfield Glossary. Retrieved from https://www.glossary.oilfield.slb.com/en/Terms/g/geopressure_gradient.aspx.

Schmoker J.W., Hester T.C. 1983. Organic Carbon on Bakken Formation, United States Portion of Williston Basin. AAPG Bulletin. 67(12): 2165- 2174.

Scholle, P. 2002. An Introduction and Virtual Geologic Field Trip to the Permian Reef Complex, Guadalupe and Delaware Mountains, New Mexico-West Texas, The New Mexico Bureau of Geology & Mineral Resources.

Sondergeld, C., Newsham, K., Comisky, J., Rice, M., & Rai, C. 2010. Petrophysical considerations in evaluating and producing shale gas resources. SPE Unconventional Gas Conference Held in Pittsburgh.

Soreghan, G.S., Keller, G.R., Gilbert, C.M., Chase, C.G., Sweet, D.E. 2012. Load- induced subsidence of the Ancestral Rocky Mountains recorded by preservation of Permian landscapes. Geosphere. published online http://dx.doi.org/ 10.1130/GES00681.1.

Steiber, S.J. 1970. Pulsed neutron capture log evaluation in the Louisiana Gulf Coast: Society of Petroleum Engineers, 45th Annual Meeting, paper SPE-2961.

Stolz, D. 2014. Reservoir character of the Avalon Shale (Bone Spring Formation) of the Delaware Basin, West Texas and Southeast New Mexico: Effect of carbonate-rich sediment gravity flows. Masters Thesis. University of Kansas.

Sutton, L. 2014. The Midland Basin vs. the Delaware Basin- Understanding the Permian. Drillinginfo. https://info.drillinginfo.com/midland-basin-vs-delaware-basin/.

Timur, A. 1968. An investigation of permeability, porosity, and residual water saturation relationships for sandstone reservoirs. The Log Analyst, v. 9, p. 8-17.

Tokonaga, T.K., and Wan, J. 2001. Surface zone flow along unsaturated rock fractures. Water Resources Research, 84: 257-264.

Tonietto, S.N., M.Z. Smoot, and M. Pope. 2014. Pore Type Characterization and Classification in Carbonate Reservoirs. Geology and Geophysics, Texas A&M University.

Veevers, J.J. & Powell, M. 1987. Late Paleozoic glacial episodes in Gondwanaland reflected in transgressive-regressive depositional sequences in Euramerica: Geological Society of America Bulletin, 98: 475-487.

Waite, L., Lindner, P., Sinclair, S., Damman, A. 2019. Lithostratigraphic Framework of the Wolfcamp and Spraberry of the Midland Basin. AAPG Southwest Sect. Annu. Conv. Dallas, Texas.

Walker, D.A., Golonka, J., Reid, A.M. & Reid, S.A.T. 1991. The effects of late Paleozoic paleolatitude and paleogeography in the Midland basin, Texas, in Candelaria, M.P., ed., Permian basin plays – tomorrow's technology today: West Texas Geological Society Publication no. 91-89, p. 141-162.

Wang, Q., 2019. Nano-petrophysics study of Haynesville Shale, East Texas, USA. The University of Texas at Arlington, MS Thesis.

Wang, S., Javadpour, F., and Feng, Q. 2016. Confinement correction to mercury intrusion capillary pressure of shale nanopores, Scientific Reports, v. 6, p. 20160.

Waples, D.W. 1985. Geochemistry in Petroleum Exploration, Chapter 2: Organic Facies, Source Rock Evaluation, International Human Resources Development Corporation. Denver, Colorado. 96 pp.

Ward, R. F., Kendall, C., Harris, P. M. 1986. Upper Permian (Guadalupian) facies and their association with hydrocarbons - Permian basin, west Texas and New Mexico. AAPG Bulletin, 70 (3), 239-262.

Ward, Z.D. 2017. Depositional Processes and Environments in Wolfcamp-Leonardian Strata, Southern Midland Basin, Texas. Oklahoma State University, MS thesis.

Washburn, E.W. 1921. Note on a method of determining the distribution of pore sizes in a porous material. Proceedings of the National Academy of Sciences, 7: 115–116.

Webb, A. 2001. An introduction to the physical characterization of materials by mercury intrusion porosimetry with emphasis on reduction and presentation of experimental data. Micromeritics Instrument Corporation.

Wickard, A.K., Elmore, R.D., and Heij, G. 2016. A Diagenetic Study of the Wolfcamp Shale, Midland Basin, West Texas. In Unconventional Resources Technology Conference, San Antonio, Texas, 1-3 August 2016 pp. 2421-2435.

Wilson, J.L. 1975. Carbonate Facies in Geological History: New York, Springer-Verlag, 471 pp.

Worley, D. 2017. Coupled Geochemical and Nano-Petrophysical Study of the Utica Play, Appalachian Basin, Ohio, U.S.A. The University of Texas at Arlington.

Yang, K.-M., and Dorobek, S. 1995. The Permian Basin of West Texas and New Mexico: Tectonic history of a "composite" foreland basin and its effects of stratigraphic development. p. 149-174, 10.2110/pec.95.52.0149.

Yang, R., Guo, X., Yi, J., Fang, Z., Hu, Q., & He, S. 2017. Spontaneous Imbibition of Three Leading Shale Formations in the Middle Yangtze Platform, South China. Energy and Fuels, 31(7), 6903–6916.

Zhang, X., Morrow, N., and Ma, S. 1996. Experimental verification of a modified scaling group for spontaneous Imbibition. SPE Reservoir Engineering, 11.04: 280-85.

Zoeten, de E., Goldstein, R.H. 2017. Diagenetic History of the Wolfcamp A in the Eastern Midland Basin, Texas. Search and Discovery Article #51395.